## Title
Biophysical Characterization of Cancer-Derived Cells and Extracellular Vesicles

**Author**
LeClaire, Michael Joseph

**Publication Date**
2021

UNIVERSITY OF CALIFORNIA

Los Angeles

# Biophysical Characterization of Cancer-Derived Cells and Extracellular Vesicles

A dissertation submitted in partial satisfaction of the requirements for the degree Doctor of Philosophy in Chemistry

by

Michael Joseph LeClaire

2021

## ABSTRACT OF THE DISSERTATION

# Biophysical Characterization of Cancer-Derived Cells and Extracellular Vesicles

by

Michael Joseph LeClaire

Doctor of Philosophy in Chemistry

University of California, Los Angeles, 2021

Professor James K. Gimzewski, Chair

Extracellular vesicles (EVs) are a class of lipid bilayer enclosed particles secreted by most mammalian cells, and are found ubiquitously in body fluids such as plasma and cerebrospinal fluid. EVs contain molecular signatures of their secreting host cells, and are involved in long-range intercellular communication and transfer of biomolecular cargo. There is significant potential for EVs to be used as biomarkers for specific cancers, and their involvement in long-range intercellular communication holds promise for their use as targeted drug delivery vehicles. However, EVs' nanoscale size and heterogeneity (30-1000 nm) and the choice of isolation methods confound the structural, biophysical, and surface biochemical analysis of single vesicles. Here, we focus on the characterization of single small extracellular vesicle (sEV) (40-160 nm) structural-mechanical properties by atomic force microscopy (AFM) and other methods. We examined the impact of isolation methods on the biophysical heterogeneity of single sEVs, including their nanoscale morphology and the presence of co-isolates. We also investigated the structural-mechanical properties of breast cancer cell line-derived sEVs and their secreting cells, finding that breast-cancer derived sEVs reflect the biomechanical signature of the cancer cells

that secrete them, and identify similar trends in patient plasma derived EV like particles. Finally, we demonstrated the applicability of AFM-based single sEV analysis as an efficient tool to quantify the abundance, structure, and biomechanical properties of sEVs from limited volume patient cerebrospinal fluid. Overall, this work advances the understanding of single sEV structural-mechanical properties, provides a framework to assess sEV quality and purity, and further develops cellular and nanoscale mechanotyping methodologies.

The dissertation of Michael Joseph LeClaire is approved.

Joseph Loo

Jian Yu Rao

Emil Reisler

James K. Gimzewski, Committee Chair

University of California, Los Angeles

2021

This dissertation is dedicated to my friends, family, and colleagues who supported me on my journey.

# Table of Contents

## List of Figures

## List of Tables

# Acknowledgements

First, I have to thank my family who have stood by me and supported me in every step of my journey, even when I decided to move cross-country to pursue my PhD at UCLA. Specifically, I'd like to thank my parents for teaching me how to be independent, and helping me nurture my love for science. I've come a long way from reading Magic School Bus books and doing science fair projects to attempt to make sandstone, and it is thanks to them always pushing me to educate myself and pursue my love for science that I made it this far. I also need to thank my sister, Marie, for all her love and support over the years, and for never complaining about the number of dog pictures I send her on Instagram.

Of course, none of this would have been possible without the guidance of my advisor, Jim Gimzewski, whose creative thinking and brilliant mind are a constant inspiration and helped me develop as a scientist. I'd also like to thank Shivani Sharma—especially over the course of the COVID-19 pandemic, her mentorship and the many hours we spent on Zoom pouring over data and talking through papers helped me thrive and succeed when everything else in the world seemed grim and bleak. I'd also like to thank the rest of my committee— Dr. Loo, Dr. Reisler, and Dr. Rao—whose teaching and mentorship helped get me going in the direction I needed to go.

I would never have made it to UCLA if it weren't for those at the University of Pittsburgh who helped me thrive and pushed me towards a graduate career. I'd like to thank Dr. Kaz Koide who accepted me as a first-year undergraduate student into his lab, and helped me develop my research skills and work ethic early on, and who shaped me into the scientist I am today. I'd also like to thank Dr. Matt Tracey (Grandpappy) who mentored me in Dr. Koide's lab, whose guidance and positive attitude have been invaluable. And I'd also like to thank Dr. Michelle Ward whose devotion to teaching and her drive to help her students thrive is something I admire and hope to carry with me for the rest of my life, and whose support helped cement my career path.

This would not have been possible without the support system I developed at UCLA. I'd like to thank my labmates Christopher Dunham, Sam Lilak, Kelsey Scharnhorst, and Renato Aguilera for all the good times we had throughout graduate school and for their support. I also have to give thanks to the undergraduate researchers I've mentored—Shayan Dadgar and Jasmine Tzeng—for working with me and helping me develop as a leader by teaching them. I'd also like to thank Dr. Weibo Yu for all of our collaboration over the years, and Dr. Adam Stieg and Dr. Mike Lake for their guidance and problem-solving for on AFM. I'd also like to thank the members of the Organization for Cultural Diversity in Science, not only for pushing to improve diversity, equity, and inclusion for underrepresented students at UCLA, but also for introducing me to so many fantastic people across the chemistry department and the division of physical sciences. I have to give a special shout-out to Hayden Montgomery, my OCDS co-president, for the tight bond we developed and for all the projects and meetings she helped me through. I'd also like to thank the UCLA Pokemon Go community for keeping me entertained over the years, but specifically my Pokemafia friends—Damani White-Lewis, Leila Fletcher, Ted Schmid, Kevin Wojta, Nathan Pham, and Benson Xu—for really making UCLA feel like home.

Finally, I have to thank all the friends who helped me and supported me over the years. I have to thank Damani (again) and Justin Gutzwa for all of our Hot Hilda Summer video chats talking about everything and nothing, and for expanding my horizons through their own research and passions. I'd like to thank Suzy Hinkle who has been nothing but a positive force in my life since we met moving in to Pitt, Jon Berman for his never-ending dad jokes and jovial attitude, Chris Persaud who has stuck by me since we sat next to each other in high school graphic design class, Ben

Alexander for always being a voice of reason and honesty, and Jeff King and Carrie Smolen for all of our RuPaul’s Drag Race and Survivor nights that were always the high point of my weeks.

**Chapter 2** is a version of Sharma, S., **LeClaire, M.** & Gimzewski, J. K. Ascent of atomic force microscopy as a nanoanalytical tool for exosomes and other extracellular vesicles. *Nanotechnology* 29, 132001 (2018). © IOP Publishing. Reproduced with permission. All rights reserved. The published manuscript carries the following acknowledgement: The authors would like to thank the International Center for Materials Nanoarchitectonics Satellite (MANA), National Institute for Materials Science (NIMS), Japan and the California NanoSystems Institute (CNSI) for their support.

**Chapter 3** is a version of Sharma, S., **LeClaire, M.**, Wohlschlegel, J. & Gimzewski, J. Impact of isolation methods on the biophysical heterogeneity of single extracellular vesicles. *Scientific Reports* 10, 13327 (2020). The published manuscript carries the following acknowledgement: We acknowledge the use of equipment at the EICN, ALMS and NPC laboratories at the CNSI, UCLA. We thank Kaituo Wang for help in acquiring cryo-EM images; Evan Darling, Leica Microsystems for help with dSTORM data analysis, and Paul Chang for help with MALS measurements of EVs. The authors also acknowledge help from Franklin Monzon (Spectradyne LLC) for micro-fluidics data analysis. This work was financially supported by NIH/NCI Grant (R21CA218386 to S.S.) and the UCLA SPORE in Brain Cancer (P50 CA211015) Career Enhancement Award (to S.S.).

**Chapter 4** is a version of **LeClaire, M.**, Gimzewski, J. & Sharma, S. A review of the biomechanical properties of single extracellular vesicles. *Nano Select* 2, 1–15 (2021). The published manuscript carries the following acknowledgement: This work was financially supported by NIH/NCI grant (R21CA218386) and the UCLA Career Enhancement Award (P50 CA211015).

**Chapter 5** is a manuscript in press and carries the following acknowledgement: This work was financially supported by NIH/NCI grant (1R21CA218386), and the UCLA Career Enhancement Award (P50 CA211015), and the NIH National Center for Advancing Translational Science (NCATS) UCLA Clinical and Translational Science Institute (TL1TR001883). We thank J. He for help with plasma samples. We thank Dr. Susan Love for several fruitful discussions. We acknowledge the use of equipment at the Advanced Light, Electron, and Nano and Pico characterization laboratories at the CNSI, UCLA. We also thank the Bio-SPMs collaborative research program at WPI-NanoLSI, Kanazawa University for travel support and Dr. A. Yurtsever and Dr. T. Fukuma for help in imaging analysis.

**Chapter 6** is a manuscript in preparation for publication.

**Chapter 7** is a version of Yu, W., Lu, Q-Y., Sharma, S., Ly, C., Di Carlo, D., Rowat, A. C., **LeClaire, M.**, Kim, D., Chow, C., Gimzewski, J. K. & Rao, J. Single Cell Mechanotype and Associated Molecular Changes in Urothelial Cell Transformation and Progression. *Front. Cell Dev. Biol.* 8, (2020). The published manuscript carries the following acknowledgement: This study was supported by the Jonsson Comprehensive Cancer Center Impact Grant, and NCI/NIH R21 CA208196: Cancer Cell Mechanical Profiling Analysis.

# Vita

| | |
|---|---|
| 2012 | Avon Grove High School; West Grove, PA |
| 2012-2016 | University Honors Scholarship |
| | University of Pittsburgh; Pittsburgh, PA |
| 2016 | Bachelor of Science; Chemistry |
| | Certificate; Gender, Sexuality, and Women's Studies |
| | University of Pittsburgh; Pittsburgh, PA |
| 2018 | Master of Science; Chemistry |
| | University of California: Los Angeles; Los Angeles, CA |

**Publications: Peer-Reviewed Journals**

- Yu, W.; Lu, Q.-Y.; Sharma, S.; Ly, C.; Di Carlo, D.; Rowat, A. C.; **LeClaire, M.**; Kim, D.; Chow, C.; Gimzewski, J. K.; Rao, J.Single Cell Mechanotype and Associated Molecular Changes in Urothelial Cell Transformation and Progression. Front. Cell Dev. Biol. 2020, 8.
- **LeClaire, M**.; Gimzewski, J. K.; Sharma, S. A Review of the Biomechanical Properties of Single Extracellular Vesicles. Nano Select 2020, 1–16.
- Sharma, S.; **LeClaire, M**.; Wohlschlegel, J.; Gimzewski, J. K. Impact of Isolation Methods on the Biophysical Heterogeneity of Single Extracellular Vesicles. Scientific Reports 2020, 10 (1), 13327.
- Pohorilets, I.; Tracey, M. P.; **LeClaire, M**.; Moore, E. M.; Lu, G.; Liu, P.; Koide, K. Kinetics and Inverse Temperature Dependence of a Tsuji–Trost Reaction in Aqueous Buffer. ACS Catal. 2019, 9 (12), 11720–11733.
- Sharma, S.; **LeClaire, M**.; Gimzewski, J. K. Ascent of Atomic Force Microscopy as a Nanoanalytical Tool for Exosomes and Other Extracellular Vesicles. Nanotechnology 2018, 29 (13), 132001

# Chapter 1. Introduction

Scientific advancement seeks to extend beyond the human limitations of our five senses, particularly so in the field of microscopy where new technologies allow us to characterize materials at higher resolution and magnification than the human body alone can. For example, the development of light microscopes expanded the capability of our sense of sight: the first light microscopes developed by Hans and Zacharias Janssen in the late 16th century achieved a magnification of 3-9x. In 1667, Robert Hooke used a light microscope with improved magnification (250x) to identify pores in a piece of cork—in his book *Micrographia*, he provided drawings of these pores which he termed “cells” due to their similarity to cells in a monastery, paving the way for modern cell theory. Most optical light microscopes are constrained by the Abbe diffraction limit of light, restricting the resolution of images obtained from these microscopes to ~250 nm. The development of techniques such as super resolution microscopy,[1] scanning tunneling microscopies[2] such as electron microscopy,[3] and scanning probe microscopies[4] such as atomic force microscopy,[5] extend the resolving power of microscopes to the nanoscale and even allowing atomic resolution of materials such as carbon nanotubes.[6] Atomic force microscopy in particular is an especially interesting microscopy technique, leveraging physical contact with the sample to not only create a topography image, but also to probe the mechanical properties of a sample, thereby combining sight with touch, and extending our sense of touch beyond human capabilities.

To speak further to the sense of touch and its application in scientific settings, our fingers can be used to qualify the stiffness, adhesivity, or texture of a surface, and in a clinical setting, the sense of touch is useful to diagnose or identify disease, particularly cancerous tumors. At the macroscale, touch allows physicians to palpate breast tissue and identify cysts or tumors based on shape, size, and stiffness.[7] Biomechanical variations in cancerous cells and tissues are a useful target for diagnosis, evident in the development of instruments such as a handheld piezoelectric needle for rapid mechano-profiling of malignant thyroid lesions.[8] The utility of touch also extends to the microscale, where AFM can be combined with optical microscopy[9] allowing simultaneous optical imaging and characterization of the distinct biomechanical signature of cancerous cells[10,11] and tissues.[12] Further, AFM extends touch to the nanoscale, allowing simultaneous structural-mechanical characterization of nanomaterials such as liposomes,[13] DNA,[14] viruses,[15] and extracellular vesicles.[16]

Extracellular vesicles in particular are a fascinating class of nanosized vesicles (30-1000 nm) of particular interest for drug delivery or biomarker applications.[17] The study of nanosized EVs often approaches from the bulk or ensemble level, obtaining population level information about particle count, size, or biomolecular composition. Much is still unknown about the biophysical characteristics of EVs at the single vesicle level. EVs are known to have specific biochemical signatures linked to their cell of origin,[18] but little is known about their biomechanical signatures, especially as it relates to malignant transformation or the use of biomechanical signatures for disease diagnosis or monitoring.

This dissertation focuses on the biophysical characterization of cancer-derived cells and extracellular vesicles, driven by AFM. I focus on single vesicle-based analysis to identify structural and mechanical features with sub-nanometer resolution. My research seeks to elucidate these features at the single vesicle or cell level towards developing them towards biomarker applications, and to bridge the gap between biochemical knowledge and biophysical knowledge. First, I will discuss the history of the field of extracellular vesicles, as well as the basics of AFM and its applicability to the study of EVs (Chapter 2). Then, I will examine the impact of EV isolation method on single vesicle nanoscale structure (Chapter 3). Next, I will discuss the relevant biomechanical properties of EVs (Chapter 4) and examine EV biomechanical signatures in breast cancer cell-derived EVs (Chapter 5) and in cerebrospinal fluid-derived EVs (Chapter 6). Finally, I will discuss the single cell mechanotyping of urothelial carcinoma cells (Chapter 7).

## References

1. Schermelleh, L. *et al.* Super-resolution microscopy demystified. *Nat Cell Biol* **21**, 72–84 (2019).
2. Binnig, G. & Rohrer, H. Scanning tunneling microscopy. *Surface Science* **126**, 236–244 (1983).
3. Franken, L. E., Grünewald, K., Boekema, E. J. & Stuart, M. C. A. A Technical Introduction to Transmission Electron Microscopy for Soft-Matter: Imaging, Possibilities, Choices, and Technical Developments. *Small* **16**, 1906198 (2020).
4. Bian, K. *et al.* Scanning probe microscopy. *Nat Rev Methods Primers* **1**, 1–29 (2021).
5. Binnig, G., Quate, C. F. & Gerber, Ch. Atomic Force Microscope. *Phys. Rev. Lett.* **56**, 930–933 (1986).
6. Odom, T. W., Huang, J.-L., Kim, P. & Lieber, C. M. Atomic structure and electronic properties of single-walled carbon nanotubes. *Nature* **391**, 62–64 (1998).
7. Powell, R. W. Breast Examination. in *Clinical Methods: The History, Physical, and Laboratory Examinations* (eds. Walker, H. K., Hall, W. D. & Hurst, J. W.) (Butterworths, 1990).
8. Sharma, S., Aguilera, R., Rao, J. & Gimzewski, J. K. Piezoelectric needle sensor reveals mechanical heterogeneity in human thyroid tissue lesions. *Scientific Reports* **9**, 9282 (2019).
9. Geisse, N. A. AFM and combined optical techniques. *Materials Today* **12**, 40–45 (2009).
10. Cross, S. E., Jin, Y.-S., Rao, J. & Gimzewski, J. K. Nanomechanical analysis of cells from cancer patients. *Nat Nanotechnol* **2**, 780–783 (2007).
11. Cross, S. *et al.* AFM-based analysis of human metastatic cancer cells. *Nanotechnology* **19**, 384003–384003 (2008).
12. Lekka, M. *et al.* Cancer cell detection in tissue sections using AFM. *Archives of Biochemistry and Biophysics* **518**, 151–156 (2012).

13. Teschke, O. & de Souza, E. F. Liposome Structure Imaging by Atomic Force Microscopy: Verification of Improved Liposome Stability during Adsorption of Multiple Aggregated Vesicles. *Langmuir* **18**, 6513–6520 (2002).

14. Hansma, H. G., Sinsheimer, R. L., Li, M.-Q. & Hansma, P. K. Atomic force microscopy of single-and double-stranded DNA. *Nucleic Acids Research* **20**, 3585–3590 (1992).

15. Kuznetsov, Y. G. & McPherson, A. Atomic Force Microscopy in Imaging of Viruses and Virus-Infected Cells. *Microbiol Mol Biol Rev* **75**, 268–285 (2011).

16. Sharma, S. *et al.* Structural-Mechanical Characterization of Nanoparticle Exosomes in Human Saliva, Using Correlative AFM, FESEM, and Force Spectroscopy. *ACS Nano* **4**, 1921–1926 (2010).

17. Kalluri, R. & LeBleu, V. S. The biology, function, and biomedical applications of exosomes. *Science* **367**, (2020).

18. Hoshino, A. *et al.* Extracellular Vesicle and Particle Biomarkers Define Multiple Human Cancers. *Cell* **182**, 1044-1061.e18 (2020).

# Chapter 2. Ascent of Atomic Force Microscopy as a Nanoanalytical Tool for Exosomes and Other Extracellular Vesicles

## 2.1 Abstract

Over the last 30 years, atomic force microscopy (AFM) has made several significant contributions to the field of biology and medicine. In this review, we draw our attention to the recent applications and promise of AFM as a high-resolution imaging and force sensing technology for probing subcellular vesicles: exosomes and other extracellular vesicles. Exosomes are naturally occurring nanoparticles found in several body fluids such as blood, saliva, cerebrospinal fluid, amniotic fluid and urine. Exosomes mediate cell–cell communication, transport proteins and genetic content between distant cells, and are now known to play important roles in progression of diseases such as cancers, neurodegenerative disorders and infectious diseases. Because exosomes are smaller than 100 nm (about 30–120 nm), the structural and molecular characterization of these vesicles at the individual level has been challenging. AFM has revealed a new degree of complexity in these nanosized vesicles and generated growing interest as a nanoscale tool for characterizing the abundance, morphology, biomechanics, and biomolecular make-up of exosomes. With the recent interest in exosomes for diagnostic and therapeutic applications, AFM-based characterization promises to contribute towards improved understanding of these particles at the single vesicle and sub-vesicular levels. When coupled with complementary methods like optical super resolution STED and Raman, AFM could further unlock the potential of exosomes as disease biomarkers and as therapeutic agents.

## 2.2 Exosomes and other extracellular vesicles (EVs) are challenging to characterize due to their nanoscale size and heterogeneity of their origin and composition

Scanning probe microscopy (SPM) opened a new era in microscopy in the field of biology and medicine over 30 years ago. So far, atomic force microscopy (AFM) has contributed unique and novel nanoscale structural, biophysical and biomolecular information on a variety of sub-cellular structures such as DNA,[1–5] membrane proteins,[6–8] vesicles,[9–12] vaults,[13] actin[14] and actin-binding proteins,[15–17] viruses[18–21] as well as bacteria,[22–24] and mammalian cells.[25,26] Recently, attention has turned to a class of sub-cellular, lipid membrane bound, nanoscale vesicles called exosomes and related EVs for their potential use as novel circulating disease biomarkers.[27–32]

Exosomes were first discovered in the 1980s in mammalian reticulocyte cells and were initially thought to be cellular trash.[33] While their specific physiological functions are currently under investigation,[34] it is now widely recognized that secreted exosomes and other EVs contain specific molecular signatures of their cells of origin. Exosomes are ubiquitously found in our bodies, and can be isolated from blood, urine, saliva, and other bodily fluids, and have been aptly termed as 'cellular FedEx system' due to their implications in long-range intracellular communications and disease propagation.[35] Diseases such as cancer,[36–38] HIV infection,[39] and Alzheimer's[40] have been shown to propagate using exosomes, and it has been hypothesized that HIV viruses can spread through the body by hijacking healthy exosomes as a sort of 'Trojan Horse' enabling them to 'sneak' into healthy cells.[41] Because exosomes possess the additional ability to pass through the blood brain barrier, exosomes may be used as novel agents to deliver drugs or nucleic content to specific cell types in the central nervous system to treat diseases such as Huntington's disease, Alzheimer's disease, and multiple sclerosis.[42] Further, exosomes have also been shown to be the primary mediator of cell-to-cell communication for mesenchymal stem cells (MSCs), and could prove to be beneficial to therapeutic applications due to their ability to circumvent issues associated with stem cell-based therapies such as issues with transplantation and directed delivery of therapeutic content.[43] MSC-derived exosomes have been used to treat cardiac disease and osteoarthritis.[43,44]

Given their tremendous diagnostic and therapeutic potential, it is not surprising that, in recent years, exosomes have become a subject of intense biomedical research. But the nanoscale size of exosomes and the heterogeneity of their origin and composition make it challenging to precisely investigate the biogenesis, structure and function of individual exosomes to aid translational research and clinical applicability.

So far, there is no gold standard technique to isolate and determine precise physical, biochemical, and bio-molecular characteristics of exosome populations. The choice of characterization method is strongly associated with the type of sample, isolation strategy, and ultimately the downstream application requirements. Exosome characterization typically involves collection of biofluids or the supernatant of cultured cells; isolation or enrichment of vesicles; classification by size, size distribution; characterization of membrane receptors (type and distribution); and subsequent extraction and analysis of their RNA,[45,46] DNA,[47] protein,[48,49] and sometimes lipid content.[50] Particle sizing and counts for exosomes in isolated samples is commonly explored using light scattering methods and assessed qualitatively using electron microscopy (EM). The biologic and genomic content of exosomes is typically studied using ensemble proteomic and sequencing methods, where single exosome level information is lost.

### 2.3 High-resolution microscopic techniques to determine exosome shape, size and morphology

In general, the nanoscale size of exosomes (30–120 nm) and other EVs precludes the use of most optical microscopies from providing structural information on exosomes (**Figure 1**). Furthermore, exosomes obtained from different bodily fluids and cell types, isolation methods, and characterization methods show significant variations both in size, structure and molecular heterogeneity.[51] **Figure 2b** shows the typical molecular contents present in exosomes. EM techniques and more recently AFM[52] and other scanning probe microscopies have proved useful for studying exosome size distributions that typically fall below the diffraction limit of light[53] as outlined in **Figure 1**. Early examinations of exosome structure and morphology used EM techniques, which provided a wealth of information about the biogenesis pathway and secretion of these vesicles from originating cells. **Figure 2a** shows early electron microscopic evidence demonstrating the release of exosome bound transferrin receptor in reticulocytes upon fusion of the multivesicular body (MVB) with the plasma membrane.

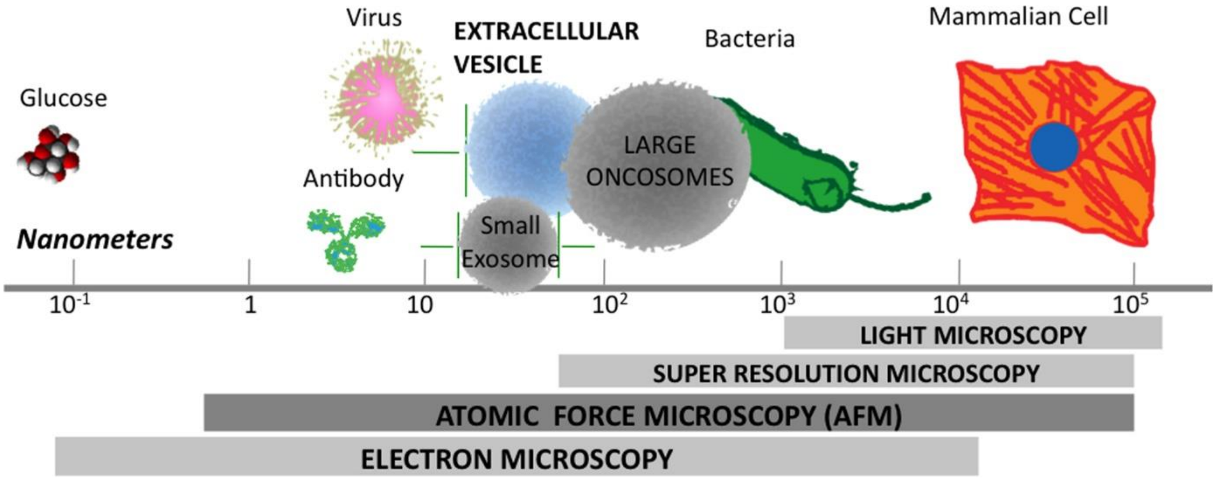

**Figure 1. Size scale for exosomes and extracellular vesicles and the different microscopic techniques available for structure and function studies**. Atomic force microscopy bridges the size scale between electron and optical microscopies as a label-free, quantitative, 3D nanoscale characterization tool. The relative abundance of exosomes, extracellular vesicles (EVs), large oncosome and presence of other extravesicular components within the purified exosome samples can be readily visualized by AFM imaging.

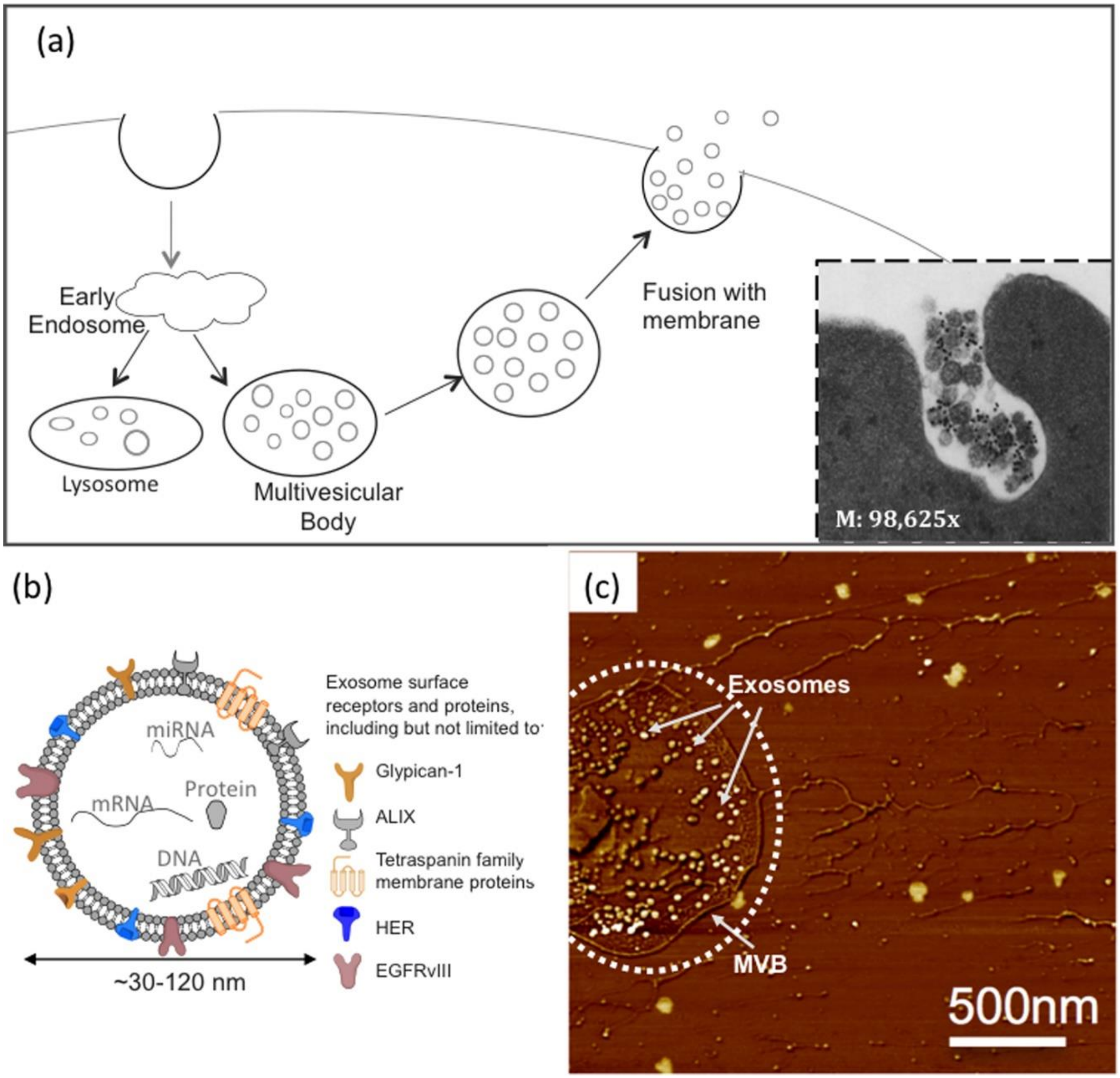

**Figure 2. Schematic illustrating the formation and release of exosomes from multivesicular bodies (MVB) at the cell surface.** (a) Inset (dashed lines) shows an electron microscopy (EM) image of an MVB releasing exosomes at the cell surface. Several small exosomes are observed within the MVB. The exosomes show surface-bound transferrin receptors labeled with gold nanoparticles, while the MVB itself does not show the presence of transferrin. (b) Magnified schematic of a single exosome displaying, mRNA, miRNA, protein, and DNA cargo, and surface proteins and receptors typically found on exosomes. (c) AFM image showing release of several nanosized exosomes from a large, micron size MVB. Limiting membrane of MVB is marked with dotted circle. MVB enclosed exosomes are marked with white arrows. Figure (a) reproduced with permission from Pan, B. T., Teng, K., Wu, C., Adam, M. & Johnstone, R. M. Electron microscopic evidence for externalization of the transferrin receptor in vesicular form in sheep reticulocytes. *Journal of Cell Biology* **101**, 942–948 (1985) and figure (c) is reprinted (adapted) with permission from Sharma, S., Gillespie, B. M., Palanisamy, V. & Gimzewski, J. K. Quantitative Nanostructural and Single Molecule Force Spectroscopy bio-molecular analysis of human saliva derived exosomes. *Langmuir* **27**, 14394–14400 (2011). Copyright (2011) American Chemical Society.

Traditional EM methods require dehydration, chemical fixation, or staining of samples that can influence the nanostructure of the exosomes, and cause to be mistakenly observed as cup-shaped vesicles instead of spherical vesicles.[12,55] Further, freezing exosome samples for scanning electron microscopy (SEM) may complicate distinction of exosomes from other vesicles secreted during cell death.[56] Cryo-EM has seen a tremendous recent improvement with the use of direct electron detectors. Advanced modes, such as the cryo-TEM, provide structure of exosomes in their native aqueous environment without staining or added fixatives. Cryo-EM[57] also enables 3D tomography, enabling spatial visualization of more complex structures, and is increasingly being used for imaging exosomes.[58,59] Detailed characterization of subpopulations of exosomes for more accurate phenotyping and enumeration in complex biofluidic environments has been achieved using Cryo-EM and immuno-gold labeling.[58,60,61] Field-emission cathodes in SEMs (FESEM) provide narrower probing beams at low and high electron energies resulting in improved spatial resolution, minimal sample charging and sample damage. FESEM provides lower electrostatic distortion, enabling a spatial resolution of 1.5 nm and has been used to differentiate morphological variations in individual exosomes as shown in **Figure 3a**.[12] Overall, EM is still the most common imaging method used to obtain qualitative information of exosome structure.

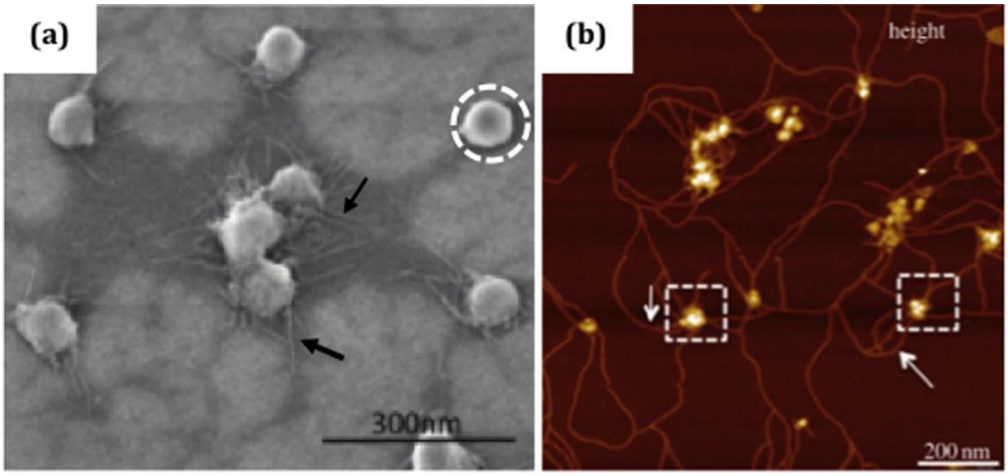

**Figure 3. Exosomes isolated from human patient saliva samples** (a) Field emission scanning electron microscopy (FESEM) image of exosomes isolated from human patient saliva samples. Round vesicular morphology outlined with white dashed circle. Intervesicular filaments are marked with black arrows. (b) Peak force AFM image of glioblastoma cell line-derived exosomes. Exosomes are marked with white dashed boxes while inter-vesicular filaments are marked with white arrows. Figure (a) reprinted (adapted) with permission Sharma, S. *et al.* Structural-Mechanical Characterization of Nanoparticle Exosomes in Human Saliva, Using Correlative AFM, FESEM, and Force Spectroscopy. *ACS Nano* **4**, 1921–1926 (2010). Copyright (2010) American Chemical Society. Figure (b) adapted from Sharma, S., Das, K., Woo, J. & Gimzewski, J. K. Nanofilaments on glioblastoma exosomes revealed by peak force microscopy. *J R Soc Interface* **11**, 20131150 (2014) with permission from The Royal Society of Chemistry.

AFM presents as a unique alternative to optical and electron diffraction techniques for studying exosomes. With its ability to quantify and simultaneously probe the abundance, structure, biomechanics, and biomolecular content of individual exosomes and other EVs (**Figure 2c and Figure 3b**) within heterogeneous populations such as tumors, AFM-based nanoscale analysis of exosomes isolated and purified from *in vitro* cell cultures or body fluids is an exciting, rapidly growing research field. In the following sections, we examine the current state of characterization methods currently utilized for exosomes and other EVs. Isolated exosomes can be immobilized and imaged on freshly cleaved mica substrate under ambient conditions, or under physiological buffer condition through non-specific surface immobilization or over specifically functionalized surfaces coated with antibodies, peptides or aptamers.[62,63] AFM works by raster scanning a tip over a sample, line-by-line, and adjusting tip height based on instrument feedback to obtain sample topography and mechanical information. This feedback can come from the force exerted on the cantilever by the surface, the frequency of oscillation of the tip, the amplitude of tip oscillation, or some combination of these. Some commonly used AFM imaging modes that have been applied to probe the structure and function of exosomes are summarized in **Figure 4**.

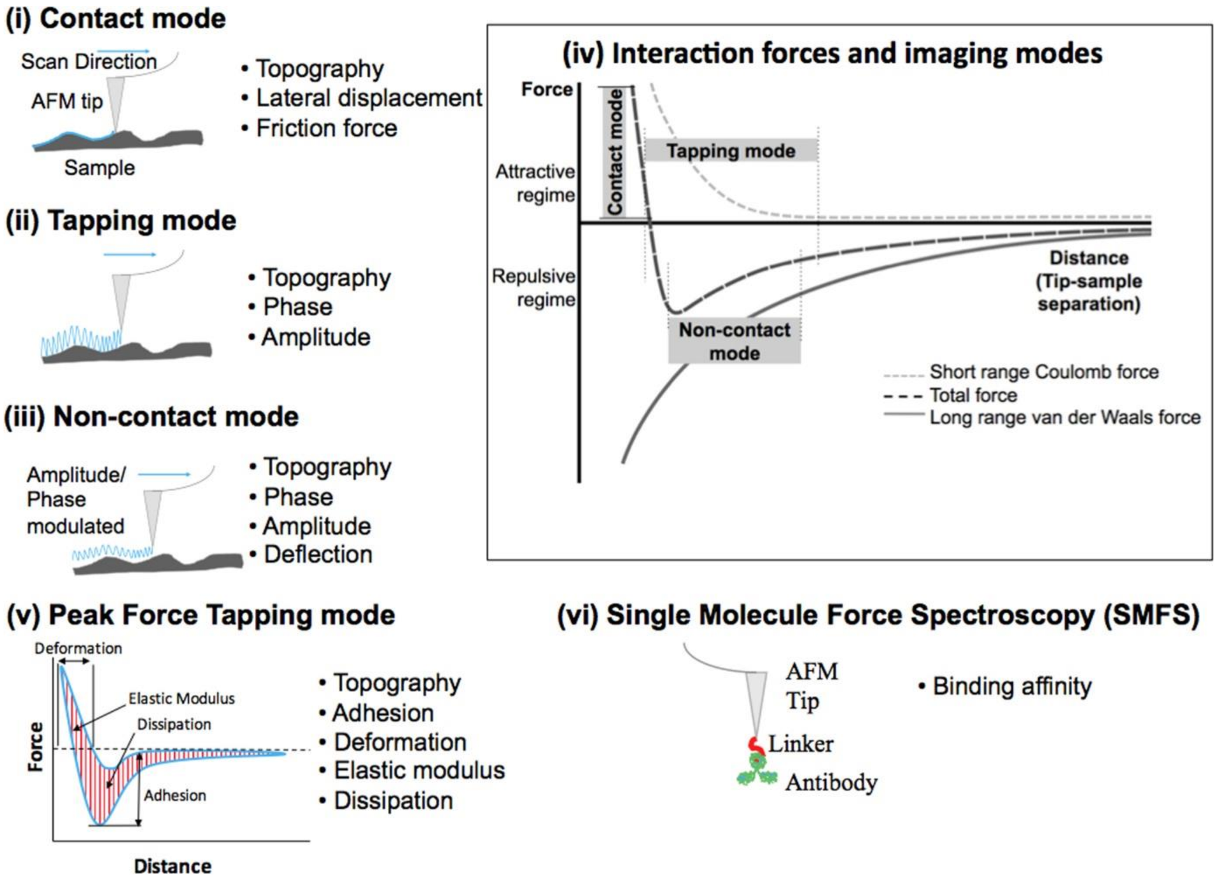

**Figure 4. Summary of the key AFM imaging and force modes applied to the study of single exosomes and extracellular vesicles**. Schematic diagram of (i) contact, (ii) tapping, (iii) non-contact and (v) peak force tapping AFM imaging modes with corresponding information obtained through each imaging mode. When an AFM tip is brought close to the sample, a number of forces may operate. Interaction forces on the tip corresponding to tip–sample separation distance are shown in (iv). Schematics for antibody functionalized single molecule force spectroscopy shown in (vi).

In *contact mode AFM* (**Figure 4i and Figure 4iv**), cantilever deflection is kept constant by adjusting the distance between tip and sample in response to topographic height change. Contact mode is difficult to use for soft biological samples due to unwanted friction and reversible or irreversible deformations in the sample[64] and therefore not frequently used in exosome imaging.

*Tapping mode AFM* (**Figure 4ii and Figure 4iv**) was invented to circumvent some of the issues associated with contact mode AFM. In tapping mode AFM, the tip is oscillated at near resonance frequency while scanning a sample, and the tip ideally only touches the sample at the downward extreme of this oscillation. Tapping mode is most commonly used for imaging of exosomes due to the simplicity of the use and less perturbation to the samples. Closely-related to tapping mode is *non-contact mode AFM* (**Figure 4iii and Figure 4iv**). In amplitude modulated AFM (AM-AFM) the oscillation amplitude is used as feedback to adjust tip height—this requires only one simple feedback loop as opposed to three in tapping mode AFM. Phase modulated AFM (PM-AFM) keeps the cantilever's oscillation amplitude constant, and instead uses the phase difference between the excitation and the oscillation as a feedback signal. Change in the phase difference reflects a change in the surface mechanical properties.[65,66] In AM-AFM and PM-AFM the tip does not touch the surface as in contact or tapping mode, but instead oscillates near the surface. Non-contact mode has been successfully used to image single exosomes.[12]

*Peak force tapping mode* (**Figure 4v**) uses low drive frequency and low drive amplitude to control the maximum force at the tip down to tens of piconewtons. The low forces used minimize sample damage and tip damage and permit sub-nm imaging of soft biological samples. Peak force tapping mode obtains adhesion force, elastic modulus, deformation, and dissipation, and is therefore useful for obtaining quantitative nanomechanical information.[67,68] Peak force mapping enable simultaneous evaluation of 3D morphology and physicochemical properties (elasticity and adhesion) of individual exosomes at sub-nm resolution with pico-Newton (pN) sensitivity.[10] 'Micro-scale' cellular extensions[69] and intercellular nanotubes[70] and their functional mechanisms in intercellular communication are currently being debated. However, using peak force mapping, our group revealed ultra-structural details of exosome surfaces.[12] Peak force images revealed distinct nanofilaments extending from the surface of glioblastoma exosomes[10] for the first time, as shown in **Figure 3b**. Individual nanofilaments within the network were measured to be 10–20 nm in diameter and up to several microns in length. The biochemical composition of these filaments needs detailed investigation into their specific role in intercellular interactions that may serve as long tethers for anchorage, increasing the probability of exosome binding to target cells. They may provide enhanced rigidity or structural integrity to parent exosomes. These rigid and adhesive nanofilaments may also harbor specific recognition motifs for cognate receptors on target cells, perhaps thereby further modulating exosome targeting, uptake, and effector functions.

Single molecule-force spectroscopy (SMFS) (**Figure 4vi**) uses tip–sample interactions to obtain force–distance curves for single molecules of interest. This is accomplished by functionalizing an AFM tip with specific chemical groups, ligands, or antibodies. When the functionalized tip comes in contact with the sample, a bond is formed, and as the tip is withdrawn from the sample, the cantilever is bent as the bond is stretched and eventually breaks.[64,71] Using either functionalized nanobeads or a functional probe tip, AFM enables complementary phenotyping of exosome subpopulations at the single-vesicle level.[11]

### 2.4 Isolation and characterization of 'purified' exosome sub-populations

Both the quality and quantity of purified exosomes affect their downstream structural and functional analysis. To date, the ideal choice of method for isolation and characterization of exosomes from bodily fluids, tissues, or cells of origin remain debatable, though is increasingly recognized to influence downstream exosome-based assays. A better understanding of the interdependence of isolation and characterization strategies would also help to clarify disparate results and lack of rigor and reproducibility in intra-laboratory findings on exosomes studied from similar cell models. Typically used exosome isolation procedures and commercial kits attempt to optimize and enrich exosomes, remove non-exosomal components and other contaminants, and evaluate the different kinds of exosome populations from specific cell types (**Table 1**). Subsequently, for each exosome sub-type the biophysical properties (size, size distribution, counts, buoyant density), cargo (e.g., tumor antigens) and surface markers with diagnostic or prognostic implications must be precisely determined. Conventional methods utilize sequential centrifugation and ultracentrifugation (UC) to spin down exosomes in cell culture media or bodily fluids.[72–75] Sucrose gradient density ultracentrifugation is used to minimize protein contamination by exploiting the density variations between exosomes and other membrane structures and viruses. Size exclusion chromatography relies on exosome physical dimensions. In immunoaffinity capture (IAC), antibodies targeting exosome surface markers such as CD9, CD63, CD81 and EpCAM are attached to magnetic beads to capture and purify exosomes.[72–74,76] A summary of main exosome isolation methods and their advantages and limitations are summarized in **Table 1**.

**Table 1. Comparison of exosome or other EVs isolation methods.**

| | **Isolation Method** | **Advantages** | **Limitations** | **References** |
|---|---|---|---|---|
| **Non-specific** | Ultracentrifugation (UC) | • Most commonly used method of isolation<br>• Produces regularly sized and shaped particles<br>• Isolated exosomes can be characterized using single particle methods such as AFM and EM | • Co-sedimented protein/RNA may affect downstream proteomics/genomics<br>• Time and labor intensive<br>• Requires >20ml starting material<br>• Requires expensive instrument | 72–75 |
| | ExoQuick kit | • Easy to perform<br>• Faster (minutes) | • Isolated particles with irregular shape and size<br>• Can co-isolate unwanted RNA content<br>• Not exosome specific<br>• Polymeric precipitates in isolated exosome samples make it difficult to probe using AFM and EM | 72,74,75 |
| | Density gradient ultracentrifugation | • Segregation of exosomes based on density profiles results in less abundance of other membrane vesicles and membrane debris in isolated samples<br>• Single particle methods such as AFM and EM can be used to study isolated populations<br>• Produces high purity RNA | • Low yielding, both of exosomes and RNA content | 74 |
| **Specific** | Immunoaffinity-Capture (IAC) | • Allows capture of exosomes/EVs containing specific surface proteins<br>• Higher specificity of exosome | • Antigen-antibody binding may modify exosomes<br>• Receptor target limited. While the exosome molecular make-up is recognized to be cell-type dependent, definitive markers for particular exosomes are yet to be established<br>• Exosomes need to be extracted from bead surface for specific assays and imaging of single vesicles using AFM and EM | 73,76 |

### 2.5 Biophysical characterization of 'purified' exosomes

Variations in the accuracy and precision of exosome isolation methods complicates the unbiased distinction of biological differences from sample-to-sample and methods variability in exosome isolation.[77] UC and precipitation can co-isolate proteins resulting in artifacts and false positive identification of exosome cargo components.[73] Precipitation introduces polyethylene glycol into the sample, which is an ion suppressor incompatible with mass spectrometry analysis.[78,79] Because of an incomplete understanding of how proteins are loaded in vesicles, it is often challenging to assess sample purity solely on the basis of protein analysis of specific proteins expected to be unrelated to exosome content.[80] A high ratio of particles-to-protein may indicate high vesicular purity,[80] but lacks distinction of vesicles from other particulate matter (protein aggregates, salts, or others) of the same size. Chemical residues from the purification process may necessitate post-isolation removal.[48] Certain sources of exosomes such as blood can introduce additional components like albumin that complicate downstream analysis.[48] Together, these current challenges in isolation, optimization and quality control of purified exosomes, highlight the significance of single vesicle characterization methods such as AFM to quantify not only the basic properties such as counts, size, morphology of purified exosomes, but also assess other phenotypes such as adhesivity, elasticity of the vesicles, extravesicular components and their surface biomolecular make-up, at the nanoscale.

Characterization of exosomes can be mainly classified into imaging methods and non-imaging methods and is used, post-exosome isolation, to assess sample purity, structure, bio-molecular content, and other biophysical characteristics. The International Society for Extracellular Vesicles (ISEV)[81] therefore recommends examining the size distribution of exosomes as a measure of the heterogeneity of a sample when studying exosomes—and recommends examining samples using EM or AFM to check the quality of a prepared sample.[72] However, the ISEV guidelines on exosome or other EVs' characterization are not limited to just those methods—a summary of some of the characterization methods is shown in **Table 2**. Non-imaging methods like nanoparticle tracking analysis (NTA) and dynamic light scattering (DLS), are fast and simple technique for examining particle size, but are hindered by polydispersity of vesicles that complicates accurate quantification of size. Imaging methods, on the other hand, can distinguish between particles of different size and have high resolution, but are limited by their low throughput.

## Table 2. Comparison of exosome and other EVs characterization methods.

| | **Characterization Method** | **Advantages** | **Limitations** | **References** |
|---|---|---|---|---|
| **Non-imaging** | Nanoparticle Tracking Analysis (NTA) | • Fast, simple | • Cannot distinguish between co-isolated particles of same size | 82,83 |
| | Dynamic Light Scattering (DLS) | | • Works best on mono-disperse samples | 84 |
| | Flow Cytometry | • Allows specific subpopulations to be analyzed via fluorescent tagging | • Assumes homogenous refractive index<br>• Poor detection limit<br>• Produces a population average | 85–88 |
| | Microfluidic Methods | • Enables multiplexing<br>• Small sample quantity needed<br>• Can be used to isolate and characterize simultaneously | • Limited by what receptors are available | 89 |
| **Imaging** | AFM | • Sub-nm resolution, ambient or fluid conditions<br>• Label-free- single vesicle morphology, size, counts<br>• Extra-vesicular components in purified samples<br>• Quantitative single vesicle adhesivity, elasticity, deformability<br>• Quantitative surface biomolecule assessment (Single molecule force spectroscopy) | • Low throughput<br>• Surface probing method<br>• Exosomes need to be stably attached on substrate | 10,12,84,85 |
| | Stimulated Emission Depletion Microscopy (STED) | • High spatial (~30 nm), temporal resolution (seconds) | • High intensity light needed<br>• Can cause phototoxicity<br>• Requires fluorescent tagging | 90 |
| | TEM | • Sub-nm resolution<br>• Can examine surface markers | • Harsh imaging conditions<br>• Can affect morphology<br>• Low throughput | 84,91,92 |
| | Cryo-EM | • Maintains morphology<br>• Allows for 3D imaging | • Specimen preparation may influence exosome size and distribution<br>• Low throughput | 55,85,93 |
| | Field Emission SEM | • Maintains morphology, high resolution | • Unconventional<br>• Rarely used | 12 |

AFM provides a significant advantage in evaluating the effects of different isolation methods on purified exosomes as it allows the size and structure to be directly visualized along with biophysical properties such as stiffness, adhesion, and deformation at single vesicle and sub-vesicle resolution. **Figure 5** illustrates one such example comparing exosomes obtained using UC and exosomes obtained using IAC. The increased surface roughness of the IAC-isolated exosome compared to those obtained using UC from the same cell type reflects the unique physiochemical and biological characteristics of purified vesicles that can be quantitatively determined at nanoscale resolution using AFM techniques.

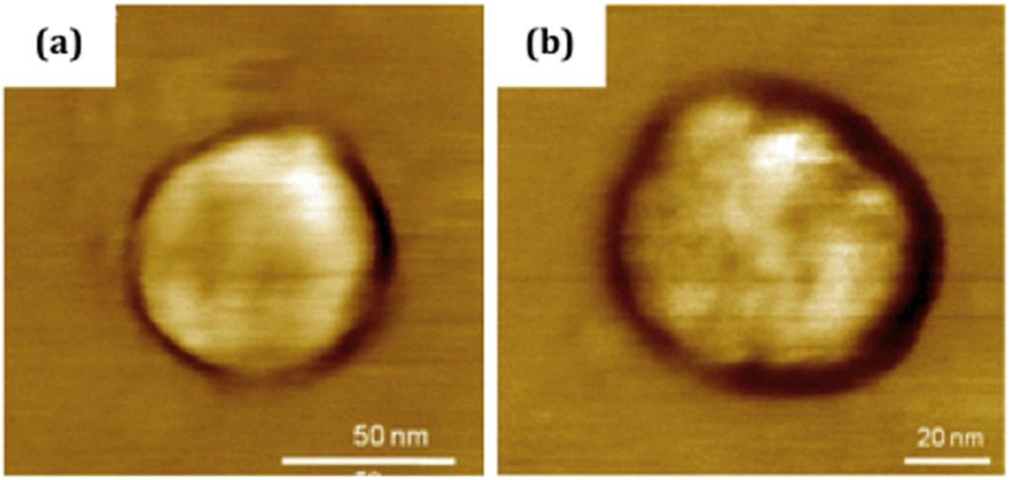

**Figure 5. Representative AFM images of U87 cell-derived exosome** isolated using ultracentrifugation (a) compared to exosome obtained using immunoaffinity capture (IAC) (b). The exosome obtained using IAC has a significantly rougher surface. Reproduced from Woo, J., Sharma, S. & Gimzewski, J. The Role of Isolation Methods on a Nanoscale Surface Structure and its Effect on the Size of Exosomes. *J Circ Biomark* **5**, 11–11 (2016).

### 2.6 Biomolecular characterization of 'purified' exosomes

Exosomes contain complex cargo of proteins and genetic material analyzed using various imaging and bioanalytical methods. Immuno gold label EM is a common imaging technique through where gold nanoparticles, labeled with specific antibodies, are bound to biological particulate of interest, and allows specific phenotypes to be studied, such as transferrin, CD235a, CD41, and CD63.[54,60,94] SMFS[95] permits AFM to go beyond imaging and probe the surface of biological matter. The technique works by specifically functionalizing an AFM tip to interact with a specific surface. As the tip approaches the surface, there is an attractive force until the two bind—then as the tip is retracted, it severs the binding of the tip and surface. This allows calculation of the specific ligand-receptor binding forces and mapping of chemical groups and receptors on a surface, and more. This interaction is shown for specific and non-specific interactions in **Figure 6** where the adhesive force between the functionalized tip and the surface receptor (**Figure 6a** and **Figure 6b**) allows a specific interaction to be differentiated from a non-specific interaction, and demonstrates a characteristic rupture force (**Figure 6c**). Cell-type specific markers such as CD63 have been visualized on the surface of exosomes by use of an antiCD63 IgG functionalized gold tip, and the antibody-antigen interaction has been reported to correlate to a difference in expression of the receptor in normal exosomes versus oral cancer derived exosomes from saliva samples.[12] Currently, force spectroscopy is hindered by the ability to only probe one type of receptor at a time, as there is only one tip, which is low throughput. However, force spectroscopy on exosomes is a largely unexplored area that is expected to advance through the combination of complementary approaches such as multiplexing and microfluidics[96] as well as multi-probe AFMs under development.[97]

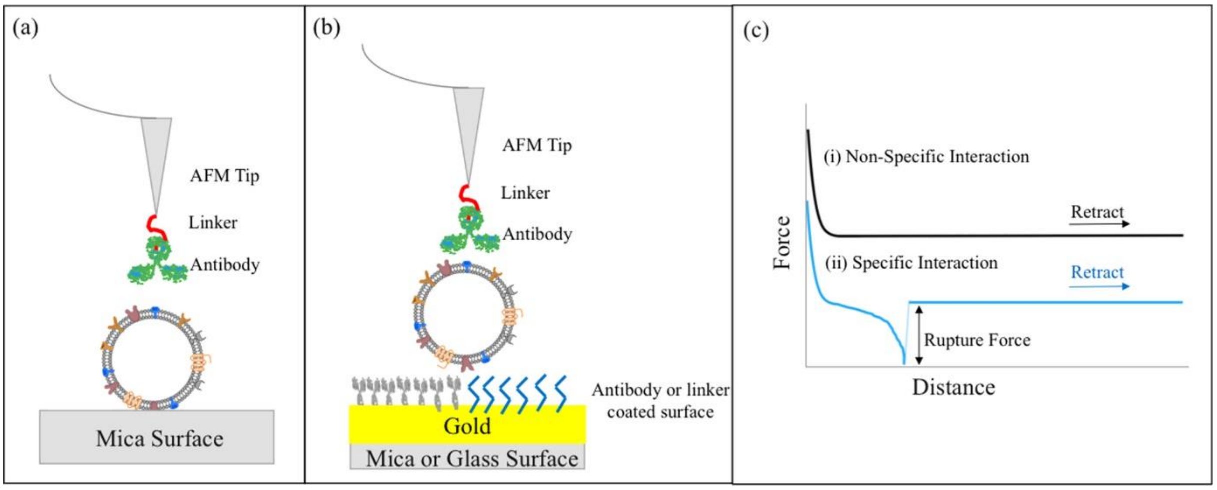

**Figure 6. AFM based single molecule force spectroscopy of exosomes using functionalized and unfunctionalized surfaces**. (a) A tip is functionalized with an antibody such as anti-CD9, anti-CD63, or anti-CD81 known to bind to a receptor on the surface of the exosome, and force–distance curves are taken. (b) This method can also be coupled with an antibody or linker coated surface (covalently or noncovalently bonded). (c) Characteristic force–distance curves are obtained that show either (i) no interactions or (ii) a specific interaction with signature rupture force marked with a double-headed arrow. Only the retraction curves are shown.

The ability to observe and understand detailed relationships between structure of exosomes and related EVs within a functional context can be further extended using correlative microscopic approaches such as AFM-Ramans.[98] Raman spectroscopy is a powerful label-free analytical technique, widely used in pharmaceutical industry, providing detailed vibrational fingerprints from the molecules under investigation. Surface-enhanced Raman scattering (SERS) offers signal enhancements of several orders of magnitude over conventional Raman scattering and has been used for characterizing exosomes.[50,99–101] However, the (often random) heterogeneity of SERS substrates leads to high variations in electromagnetic field enhancement across the sample surface, which limits its range of application. An alternative approach called tip-enhanced Raman spectroscopy (TERS) involves reducing the enhancing substrate to a single local '*enhancement* spot' at the end of a very sharp tip, which can be accurately positioned on the sample surface via AFM. TERS enables spectroscopic imaging with sub-diffraction spatial resolution (<50 nm) by scanning the local 'enhanced spot' at the end of the AFM tip across the sample surface. A typical TERS system combines a confocal laser scanning microscope with an AFM. The confocal microscope allows for rapid optical alignment of the laser focus with a metal-coated AFM tip and requires a movable sample stage to scan the sample relative to the prealigned laser-to-tip configuration. TERS[102] can potentially provide nanoscale chemical composition and morphology of biological samples such as exosomes in a label-free manner. It has been used to differentiate picomole quantities of surface adsorbed normal nucleobases A, T, G, C.[103] TERS spectra has been used to study both large protein assemblies[104] and filamentous structures such as amyloid fibrils[105] as well as to identify the contributions of surface lipid molecules, RNA and protein.[106] This promising method allows biomolecules to be studied in their native condition and reduces sample heating due to the laser and photobleaching, and it remains to be explored further within the context of exosomes. The quality and durability of the probes are often key to a successful TERS experiment. The data acquisition time for TERS mapping and the available scan range currently limit the application of TERS as a standard tool for spectroscopic imaging of exosomes. Development of new scanning modes for TERS, enabling a trade-off between image size and spatial resolution and robust probes will be needed to test the applicability of this technique for exosome biochemical characterization.

Exosomes typically comprise of luminal cargo, i.e., proteins, DNA, RNA, peptides, and lipid-derivatives, surrounded by a lipid bilayer membrane. In 2007, Valadi *et al* were the first to confirm the presence of RNA inside EVs and also showed that mRNA inside EVs could be translated into proteins *in vitro*.[107] EVs were shown to carry single-stranded DNA, amplified oncogene sequences and transposable elements,[108] and the presence of double stranded DNA in tumor-derived EVs has been reported by several research groups.[108–110] Two online databases, ExoCarta (http://exocarta.org), a database that lists proteins, RNA and lipids identified in exosomes, and Vesiclepedia (http://microvesicles.org), a community annotation compendium for all EVs, are available online. Mostly utilized as a surface-mapping tool, AFM has been previously employed to also probe intracellular molecules such as mRNA without compromising the viability of the targeted cell.[111,112] The AFM-based method involves pushing a bare AFM probe into a live cell by applying a compressive forces of 10–100 nN, holding the probe within the cell for a short time, and pulling it out for subsequent amplification and quantitation of retrieved mRNAs into cDNA through quantitative RT-PCR and PCR procedures. Measurement of the binding and unbinding forces between the oligonucleotides DNA probe on the AFM tip and the complementary target mRNA has also been demonstrated.[113] Through such combinations of molecular specificity, broader application fields can be opened for exosome phenotyping and genotyping.

**Table 3. Potential uses of exosomes as biomarkers**

| | Disease | Biomarker | References |
|---|---|---|---|
| **Cancers** | Prostate Cancer | PCA3, TMPRSS2-ERG | 27 |
| | Colon Cancer | miR-181 | 29 |
| | Pancreatic Cancer | Glypican-1, various miRNA | 28,44 |
| | Brain Cancer | EGFRvIII | 114,115 |
| | Lung Cancer | a6b4 and a6b1 integrins | 36 |
| | Bladder Cancer | HOTAIR | 116 |
| **Neurodegenerative Diseases** | Alzheimer's | Various miRNA, B-amyloid proteins released alongside exosomes | 31,32 |
| | Parkinson's | miR-19b, miR-24, and miR-195, a-synuclein | 117,118 |
| **Other Diseases** | Macular degeneration | cathepsin D, cytokeratin 8, more proteins | 30 |

### 2.7 Summary and outlook for AFM based exosome analysis

Current challenges impeding the use of exosomes in biomarkers and therapy include tumor origin specificity, the number of exosomes that can be obtained from samples, and the need for a renewable cell source for widespread therapeutic application.[119] Nonetheless, analysis of exosomes and other EVs in body fluids could, in the future, be the standard for diagnostics in medicine (prominent candidates of exosome based biomarkers under investigation are shown in **Table 3**). On one hand, the size, number, concentration, and composition of exosomes are influenced by diseases including cancer, neurodegenerative diseases, and other anomalies, and thus comprise clinically relevant information. On the other hand, the best utilization of this information warrants standardization of exosome-based analysis.[120] This is one area where AFM has already been acknowledged as a key exosome metrology tool.[81] As a next step in developing the EV field, ISEV produced a series of educational massive open online courses (MOOCs) titled 'basics of EVs'. A MOOC is an online course where recorded lectures and presentations are used. It is open access via the World Wide Web and can be accessed by an unlimited number of participants (the course is accessible at https://coursera.org/learn/extracellular-vesicles). Module five in this series highlights an example of the growing popularity of the AFM as a characterization tool for exosomes and EVs of different sources and beyond.

## 2.8 References

1. Lindsay, S. M. *et al.* STM and AFM Images of Nucleosome DNA Under Water. *Journal of Biomolecular Structure and Dynamics* **7**, 279–287 (1989).
2. Berg, F., Wilken, J., Helm, C. A. & Block, S. AFM-Based Quantification of Conformational Changes in DNA Caused by Reactive Oxygen Species. *J. Phys. Chem. B* **119**, 25–32 (2015).
3. Hansma, H. G. *et al.* Progress in sequencing deoxyribonucleic acid with an atomic force microscope. *Journal of Vacuum Science & Technology B: Microelectronics and Nanometer Structures Processing, Measurement, and Phenomena* **9**, 1282–1284 (1991).
4. Hansma, H. G., Sinsheimer, R. L., Li, M.-Q. & Hansma, P. K. Atomic force microscopy of single-and double-stranded DNA. *Nucleic Acids Research* **20**, 3585–3590 (1992).
5. Leung, C. *et al.* Atomic Force Microscopy with Nanoscale Cantilevers Resolves Different Structural Conformations of the DNA Double Helix. *Nano Lett.* **12**, 3846–3850 (2012).
6. Engel, A. & Müller, D. J. Observing single biomolecules at work with the atomic force microscope. *Nat Struct Mol Biol* **7**, 715–718 (2000).
7. Milhiet, P.-E. *et al.* High-Resolution AFM of Membrane Proteins Directly Incorporated at High Density in Planar Lipid Bilayer. *Biophysical Journal* **91**, 3268–3275 (2006).
8. Whited, A. M. & Park, P. S.-H. Atomic force microscopy: A multifaceted tool to study membrane proteins and their interactions with ligands. *Biochimica et Biophysica Acta (BBA) - Biomembranes* **1838**, 56–68 (2014).
9. Jena, B. P. ‘Porosome’ discovered nearly 20 years ago provides molecular insights into the kiss-and-run mechanism of cell secretion. *Journal of Cellular and Molecular Medicine* **19**, 1427–1440 (2015).
10. Sharma, S., Das, K., Woo, J. & Gimzewski, J. K. Nanofilaments on glioblastoma exosomes revealed by peak force microscopy. *J R Soc Interface* **11**, 20131150 (2014).

11. Sharma, S., Gillespie, B. M., Palanisamy, V. & Gimzewski, J. K. Quantitative Nanostructural and Single Molecule Force Spectroscopy bio-molecular analysis of human saliva derived exosomes. *Langmuir* **27**, 14394–14400 (2011).
12. Sharma, S. *et al.* Structural-Mechanical Characterization of Nanoparticle Exosomes in Human Saliva, Using Correlative AFM, FESEM, and Force Spectroscopy. *ACS Nano* **4**, 1921–1926 (2010).
13. Xia, Y. *et al.* Immobilization of Recombinant Vault Nanoparticles on Solid Substrates. *ACS Nano* **4**, 1417–1424 (2010).
14. Kronlage, C., Schäfer-Herte, M., Böning, D., Oberleithner, H. & Fels, J. Feeling for Filaments: Quantification of the Cortical Actin Web in Live Vascular Endothelium. *Biophysical Journal* **109**, 687–698 (2015).
15. Kodera, N., Yamamoto, D., Ishikawa, R. & Ando, T. Video imaging of walking myosin V by high-speed atomic force microscopy. *Nature* **468**, 72–76 (2010).
16. Sharma, S., Grintsevich, E. E., Phillips, M. L., Reisler, E. & Gimzewski, J. K. Atomic Force Microscopy Reveals Drebrin Induced Remodeling of F-Actin with Subnanometer Resolution. *Nano Lett.* **11**, 825–827 (2011).
17. Sharma, S., Zhu, H., E. Grintsevich, E., Reisler, E. & K. Gimzewski, J. Correlative nanoscale imaging of actin filaments and their complexes. *Nanoscale* **5**, 5692–5702 (2013).
18. W. Chen, S. *et al.* Nanoscale structural features determined by AFM for single virus particles. *Nanoscale* **5**, 10877–10886 (2013).
19. Hernando-Pérez, M. *et al.* Nanoindentation of Isometric Viruses on Deterministically Corrugated Substrates. *J. Phys. Chem. B* **120**, 340–347 (2016).
20. Kuznetsov, Yu. G., Malkin, A. J., Lucas, R. W., Plomp, M. & McPherson, A. Y. 2001. Imaging of viruses by atomic force microscopy. *Journal of General Virology* **82**, 2025–2034.

21. Malkin, A. J., Land, T. A., Kuznetsov, Yu. G., McPherson, A. & DeYoreo, J. J. Investigation of Virus Crystal Growth Mechanisms by In Situ Atomic Force Microscopy. *Phys. Rev. Lett.* **75**, 2778–2781 (1995).
22. F. Dufrêne, Y. AFM for nanoscale microbe analysis. *Analyst* **133**, 297–301 (2008).
23. Francius, G. *et al.* Detection, Localization, and Conformational Analysis of Single Polysaccharide Molecules on Live Bacteria. *ACS Nano* **2**, 1921–1929 (2008).
24. Liu, S. & Wang, Y. Application of AFM in microbiology: a review. *Scanning* **32**, 61–73 (2010).
25. Sreenivasappa, H. *et al.* Selective regulation of cytoskeletal tension and cell–matrix adhesion by RhoA and Src. *Integrative Biology* **6**, 743–754 (2014).
26. Sun, Z. *et al.* Mechanical properties of the interaction between fibronectin and α5β1-integrin on vascular smooth muscle cells studied using atomic force microscopy. *American Journal of Physiology-Heart and Circulatory Physiology* **289**, H2526–H2535 (2005).
27. Dijkstra Siebren *et al.* Prostate Cancer Biomarker Profiles in Urinary Sediments and Exosomes. *Journal of Urology* **191**, 1132–1138 (2014).
28. Melo, S. A. *et al.* Glypican-1 identifies cancer exosomes and detects early pancreatic cancer. *Nature* **523**, 177–182 (2015).
29. Ogata-Kawata, H. *et al.* Circulating Exosomal microRNAs as Biomarkers of Colon Cancer. *PLOS ONE* **9**, e92921 (2014).
30. Kang, G.-Y. *et al.* Exosomal Proteins in the Aqueous Humor as Novel Biomarkers in Patients with Neovascular Age-related Macular Degeneration. *J. Proteome Res.* **13**, 581–595 (2014).
31. Van Giau, V. & An, S. S. A. Emergence of exosomal miRNAs as a diagnostic biomarker for Alzheimer’s disease. *Journal of the Neurological Sciences* **360**, 141–152 (2016).

32. Vella, L. J., Hill, A. F. & Cheng, L. Focus on Extracellular Vesicles: Exosomes and Their Role in Protein Trafficking and Biomarker Potential in Alzheimer's and Parkinson's Disease. *International Journal of Molecular Sciences* **17**, 173 (2016).

33. Johnstone, R. M. Maturation of reticulocytes: formation of exosomes as a mechanism for shedding membrane proteins. *Biochemistry and Cell Biology* (2011) doi:10.1139/o92-028.

34. Sharma, S. & Gimzewski, J. K. The Quest for Characterizing Exosomes: Circulating Nano-Sized Vesicles. *J Nanomedic Nanotechnol* **03**, (2012).

35. Sharma, S. & Gimzewski, J. Exosomes: Nanoscale Packages Contain the Health-state [Status Quo] of the Cells that Secrete them. *Journal of Nanomedicine & Nanotechnology* **06**, (2015).

36. Becker, A. *et al.* Extracellular Vesicles in Cancer: Cell-to-Cell Mediators of Metastasis. *Cancer Cell* **30**, 836–848 (2016).

37. Kahlert, C. & Kalluri, R. Exosomes in tumor microenvironment influence cancer progression and metastasis. *J Mol Med* **91**, 431–437 (2013).

38. Peinado, H. *et al.* Melanoma exosomes educate bone marrow progenitor cells toward a pro-metastatic phenotype through MET. *Nat Med* **18**, 883–891 (2012).

39. von Schwedler, U. K. *et al.* The Protein Network of HIV Budding. *Cell* **114**, 701–713 (2003).

40. Rajendran, L. *et al.* Alzheimer's disease β-amyloid peptides are released in association with exosomes. *PNAS* **103**, 11172–11177 (2006).

41. Gould, S. J., Booth, A. M. & Hildreth, J. E. K. The Trojan exosome hypothesis. *Proc Natl Acad Sci U S A* **100**, 10592–10597 (2003).

42. Aryani, A. & Denecke, B. Exosomes as a Nanodelivery System: a Key to the Future of Neuromedicine? *Mol Neurobiol* **53**, 818–834 (2016).

43. Lai, R. C., Chen, T. S. & Lim, S. K. Mesenchymal stem cell exosome: a novel stem cell-based therapy for cardiovascular disease. *Regenerative Medicine* **6**, 481–492 (2011).

44. Toh, W. S., Lai, R. C., Hui, J. H. P. & Lim, S. K. MSC exosome as a cell-free MSC therapy for cartilage regeneration: Implications for osteoarthritis treatment. *Seminars in Cell & Developmental Biology* **67**, 56–64 (2017).

45. Chevillet, J. R. *et al.* Quantitative and stoichiometric analysis of the microRNA content of exosomes. *PNAS* **111**, 14888–14893 (2014).

46. Li, M. *et al.* Analysis of the RNA content of the exosomes derived from blood serum and urine and its potential as biomarkers. *Philosophical Transactions of the Royal Society B: Biological Sciences* **369**, 20130502 (2014).

47. Thakur, B. K. *et al.* Double-stranded DNA in exosomes: a novel biomarker in cancer detection. *Cell Res* **24**, 766–769 (2014).

48. Schey, K. L., Luther, J. M. & Rose, K. L. Proteomics characterization of exosome cargo. *Methods* **87**, 75–82 (2015).

49. Welton, J. L. *et al.* Proteomics Analysis of Bladder Cancer Exosomes*. *Molecular & Cellular Proteomics* **9**, 1324–1338 (2010).

50. Smith, Z. J. *et al.* Single exosome study reveals subpopulations distributed among cell lines with variability related to membrane content. *Journal of Extracellular Vesicles* **4**, 28533 (2015).

51. Chernyshev, V. S. *et al.* Size and shape characterization of hydrated and desiccated exosomes. *Anal Bioanal Chem* **407**, 3285–3301 (2015).

52. Binnig, G., Quate, C. F. & Gerber, Ch. Atomic Force Microscope. *Phys. Rev. Lett.* **56**, 930–933 (1986).

53. Harke, B., Chacko, J. V., Haschke, H., Canale, C. & Diaspro, A. A novel nanoscopic tool by combining AFM with STED microscopy. *Optical Nanoscopy* **1**, 3 (2012).

54. Pan, B. T., Teng, K., Wu, C., Adam, M. & Johnstone, R. M. Electron microscopic evidence for externalization of the transferrin receptor in vesicular form in sheep reticulocytes. *Journal of Cell Biology* **101**, 942–948 (1985).

55. Yuana, Y. *et al.* Cryo-electron microscopy of extracellular vesicles in fresh plasma. *Journal of Extracellular Vesicles* **2**, 21494 (2013).

56. Wu, Y., Deng, W. & Ii, D. J. K. Exosomes: improved methods to characterize their morphology, RNA content, and surface protein biomarkers. *Analyst* **140**, 6631–6642 (2015).

57. Dubochet, J. Cryo-EM—the first thirty years. *Journal of Microscopy* **245**, 221–224 (2012).

58. Höög, J. L. & Lötvall, J. Diversity of extracellular vesicles in human ejaculates revealed by cryo-electron microscopy. *Journal of Extracellular Vesicles* **4**, 28680 (2015).

59. Grey, M. *et al.* Acceleration of α-Synuclein Aggregation by Exosomes*,. *Journal of Biological Chemistry* **290**, 2969–2982 (2015).

60. Arraud, N. *et al.* Extracellular vesicles from blood plasma: determination of their morphology, size, phenotype and concentration. *Journal of Thrombosis and Haemostasis* **12**, 614–627 (2014).

61. Zabeo, D. *et al.* Exosomes purified from a single cell type have diverse morphology. *Journal of Extracellular Vesicles* **6**, 1329476 (2017).

62. Hardij, J. *et al.* Characterisation of tissue factor-bearing extracellular vesicles with AFM: comparison of air-tapping-mode AFM and liquid Peak Force AFM. *Journal of Extracellular Vesicles* **2**, 21045 (2013).

63. Jørgensen, M. *et al.* Extracellular Vesicle (EV) Array: microarray capturing of exosomes and other extracellular vesicles for multiplexed phenotyping. *Journal of Extracellular Vesicles* **2**, 20920 (2013).

64. Dufrêne, Y. F. *et al.* Imaging modes of atomic force microscopy for application in molecular and cell biology. *Nature Nanotech* **12**, 295–307 (2017).

65. Hölscher, H. Theory of phase-modulation atomic force microscopy with constant-oscillation amplitude. *Journal of Applied Physics* **103**, 064317 (2008).

66. Sugawara, Y. *et al.* Elimination of instabilities in phase shift curves in phase-modulation atomic force microscopy in constant-amplitude mode. *Appl. Phys. Lett.* **90**, 194104 (2007).

67. Adamcik, J., Berquand, A. & Mezzenga, R. Single-step direct measurement of amyloid fibrils stiffness by peak force quantitative nanomechanical atomic force microscopy. *Appl. Phys. Lett.* **98**, 193701 (2011).

68. Pittenger, B., Erina, N. & Su, C. Quantitative Mechanical Property Mapping at the Nanoscale with PeakForce QNM. *Bruker Application Note* **128**, 12.

69. Rustom, A., Saffrich, R., Markovic, I., Walther, P. & Gerdes, H.-H. Nanotubular Highways for Intercellular Organelle Transport. *Science* **303**, 1007–1010 (2004).

70. Gerdes, H.-H., Bukoreshtliev, N. V. & Barroso, J. F. V. Tunneling nanotubes: A new route for the exchange of components between animal cells. *FEBS Letters* **581**, 2194–2201 (2007).

71. Neuman, K. C. & Nagy, A. Single-molecule force spectroscopy: optical tweezers, magnetic tweezers and atomic force microscopy. *Nat Methods* **5**, 491–505 (2008).

72. Lener, T. *et al.* Applying extracellular vesicles based therapeutics in clinical trials – an ISEV position paper. *Journal of Extracellular Vesicles* **4**, 30087 (2015).

73. Tauro, B. J. *et al.* Comparison of ultracentrifugation, density gradient separation, and immunoaffinity capture methods for isolating human colon cancer cell line LIM1863-derived exosomes. *Methods* **56**, 293–304 (2012).

74. Deun, J. V. *et al.* The impact of disparate isolation methods for extracellular vesicles on downstream RNA profiling. *Journal of Extracellular Vesicles* **3**, 24858 (2014).

75. Zlotogorski-Hurvitz, A. *et al.* Human Saliva-Derived Exosomes: Comparing Methods of Isolation. *J Histochem Cytochem.* **63**, 181–189 (2015).

76. Woo, J., Sharma, S. & Gimzewski, J. The Role of Isolation Methods on a Nanoscale Surface Structure and its Effect on the Size of Exosomes. *J Circ Biomark* **5**, 11–11 (2016).

77. Abramowicz, A., Widlak, P. & Pietrowska, M. Proteomic analysis of exosomal cargo: the challenge of high purity vesicle isolation. *Molecular BioSystems* **12**, 1407–1419 (2016).
78. Keerthikumar, S. *et al.* Proteogenomic analysis reveals exosomes are more oncogenic than ectosomes. *Oncotarget* **6**, 15375–15396 (2015).
79. Keller, B. O., Sui, J., Young, A. B. & Whittal, R. M. Interferences and contaminants encountered in modern mass spectrometry. *Analytica Chimica Acta* **627**, 71–81 (2008).
80. Webber, J. & Clayton, A. How pure are your vesicles? *Journal of Extracellular Vesicles* **2**, 19861 (2013).
81. Araldi, E. *et al.* International Society for Extracellular Vesicles: first annual meeting, April 17–21, 2012: ISEV-2012. *Journal of Extracellular Vesicles* **1**, 19995 (2012).
82. Caponnetto, F. *et al.* Size-dependent cellular uptake of exosomes. *Nanomedicine: Nanotechnology, Biology and Medicine* **13**, 1011–1020 (2017).
83. Lötvall, J. *et al.* Minimal experimental requirements for definition of extracellular vesicles and their functions: a position statement from the International Society for Extracellular Vesicles. *Journal of Extracellular Vesicles* **3**, 26913 (2014).
84. Pol, E. V. D. *et al.* Optical and non-optical methods for detection and characterization of microparticles and exosomes. *Journal of Thrombosis and Haemostasis* **8**, 2596–2607 (2010).
85. Khatun, Z., Bhat, A., Sharma, S. & Sharma, A. Elucidating diversity of exosomes: biophysical and molecular characterization methods. *Nanomedicine* **11**, 2359–2377 (2016).
86. Nolan, J. P. & Jones, J. C. Detection of platelet vesicles by flow cytometry. *Platelets* **28**, 256–262 (2017).
87. Pospichalova, V. *et al.* Simplified protocol for flow cytometry analysis of fluorescently labeled exosomes and microvesicles using dedicated flow cytometer. *Journal of Extracellular Vesicles* **4**, 25530 (2015).

88. Pol, E. van der *et al.* Particle size distribution of exosomes and microvesicles determined by transmission electron microscopy, flow cytometry, nanoparticle tracking analysis, and resistive pulse sensing. *Journal of Thrombosis and Haemostasis* **12**, 1182–1192 (2014).
89. Im, H., Shao, H., Weissleder, R., Castro, C. M. & Lee, H. Nano-plasmonic exosome diagnostics. *Expert Review of Molecular Diagnostics* **15**, 725–733 (2015).
90. Tam, J. & Merino, D. Stochastic optical reconstruction microscopy (STORM) in comparison with stimulated emission depletion (STED) and other imaging methods. *Journal of Neurochemistry* **135**, 643–658 (2015).
91. Sokolova, V. *et al.* Characterisation of exosomes derived from human cells by nanoparticle tracking analysis and scanning electron microscopy. *Colloids and Surfaces B: Biointerfaces* **87**, 146–150 (2011).
92. Witwer, K. W. *et al.* Standardization of sample collection, isolation and analysis methods in extracellular vesicle research. *Journal of Extracellular Vesicles* **2**, 20360 (2013).
93. Kadiu, I., Narayanasamy, P., Dash, P. K., Zhang, W. & Gendelman, H. E. Biochemical and Biologic Characterization of Exosomes and Microvesicles as Facilitators of HIV-1 Infection in Macrophages. *The Journal of Immunology* **189**, 744–754 (2012).
94. Brisson, A. R., Tan, S., Linares, R., Gounou, C. & Arraud, N. Extracellular vesicles from activated platelets: a semiquantitative cryo-electron microscopy and immuno-gold labeling study. *Platelets* **28**, 263–271 (2017).
95. Dufrêne, Y. F., Martínez-Martín, D., Medalsy, I., Alsteens, D. & Müller, D. J. Multiparametric imaging of biological systems by force-distance curve–based AFM. *Nat Methods* **10**, 847–854 (2013).
96. Anderson, M. S. Microfluidics and Chromatography with an Atomic Force Microscope. *Anal. Chem.* **77**, 2907–2911 (2005).

97. Tsunemi, E. *et al.* Development of multi-environment dual-probe atomic force microscopy system using optical beam deflection sensors with vertically incident laser beams. *Review of Scientific Instruments* **84**, 083701 (2013).

98. Prats-Mateu, B. & Gierlinger, N. Tip in–light on: Advantages, challenges, and applications of combining AFM and Raman microscopy on biological samples. *Microscopy Research and Technique* **80**, 30–40 (2017).

99. Lee, C. *et al.* 3D plasmonic nanobowl platform for the study of exosomes in solution. *Nanoscale* **7**, 9290–9297 (2015).

100. Stremersch, S. *et al.* Identification of Individual Exosome-Like Vesicles by Surface Enhanced Raman Spectroscopy. *Small* **12**, 3292–3301 (2016).

101. Tatischeff, I., Larquet, E., Falcón-Pérez, J. M., Turpin, P.-Y. & Kruglik, S. G. Fast characterisation of cell-derived extracellular vesicles by nanoparticles tracking analysis, cryo-electron microscopy, and Raman tweezers microspectroscopy. *Journal of Extracellular Vesicles* **1**, 19179 (2012).

102. Sharma, G., Deckert-Gaudig, T. & Deckert, V. Tip-enhanced Raman scattering—Targeting structure-specific surface characterization for biomedical samples. *Advanced Drug Delivery Reviews* **89**, 42–56 (2015).

103. Domke, K. F., Zhang, D. & Pettinger, B. Tip-Enhanced Raman Spectra of Picomole Quantities of DNA Nucleobases at Au(111). *J. Am. Chem. Soc.* **129**, 6708–6709 (2007).

104. Yeo, B.-S., Mädler, S., Schmid, T., Zhang, W. & Zenobi, R. Tip-Enhanced Raman Spectroscopy Can See More:  The Case of Cytochrome c. *J. Phys. Chem. C* **112**, 4867–4873 (2008).

105. Tabatabaei, M., A. Caetano, F., Pashee, F., G. Ferguson, S. S. & Lagugné-Labarthet, F. Tip-enhanced Raman spectroscopy of amyloid β at neuronal spines. *Analyst* **142**, 4415–4421 (2017).

106. Cialla, D. *et al.* Raman to the limit: tip-enhanced Raman spectroscopic investigations of a single tobacco mosaic virus. *Journal of Raman Spectroscopy* **40**, 240–243 (2009).

107. Valadi, H. *et al.* Exosome-mediated transfer of mRNAs and microRNAs is a novel mechanism of genetic exchange between cells. *Nat Cell Biol* **9**, 654–659 (2007).

108. Balaj, L. *et al.* Tumour microvesicles contain retrotransposon elements and amplified oncogene sequences. *Nat Commun* **2**, 180 (2011).

109. Kahlert, C. *et al.* Identification of Double-stranded Genomic DNA Spanning All Chromosomes with Mutated KRAS and p53 DNA in the Serum Exosomes of Patients with Pancreatic Cancer*. *Journal of Biological Chemistry* **289**, 3869–3875 (2014).

110. Lee, T. H. *et al.* Oncogenic ras-driven cancer cell vesiculation leads to emission of double-stranded DNA capable of interacting with target cells. *Biochemical and Biophysical Research Communications* **451**, 295–301 (2014).

111. Osada, T., Uehara, H., Kim, H. & Ikai, A. mRNA analysis of single living cells. *J Nanobiotechnol* **1**, 2 (2003).

112. Uehara, H., Osada, T. & Ikai, A. Quantitative measurement of mRNA at different loci within an individual living cell. *Ultramicroscopy* **100**, 197–201 (2004).

113. Jung, Y. J. *et al.* Molecule-level imaging of Pax6 mRNA distribution in mouse embryonic neocortex by molecular interaction force microscopy. *Nucleic Acids Research* **37**, e10–e10 (2009).

114. D'Asti, E., Chennakrishnaiah, S., Lee, T. H. & Rak, J. Extracellular Vesicles in Brain Tumor Progression. *Cell Mol Neurobiol* **36**, 383–407 (2016).

115. Skog, J. *et al.* Glioblastoma microvesicles transport RNA and proteins that promote tumour growth and provide diagnostic biomarkers. *Nat Cell Biol* **10**, 1470–1476 (2008).

116. Berrondo, C. *et al.* Expression of the Long Non-Coding RNA HOTAIR Correlates with Disease Progression in Bladder Cancer and Is Contained in Bladder Cancer Patient Urinary Exosomes. *PLOS ONE* **11**, e0147236 (2016).

117. Cao, X.-Y. *et al.* MicroRNA biomarkers of Parkinson’s disease in serum exosome-like microvesicles. *Neuroscience Letters* **644**, 94–99 (2017).

118. Wu, X., Zheng, T. & Zhang, B. Exosomes in Parkinson’s Disease. *Neurosci. Bull.* **33**, 331–338 (2017).

119. Sun, D. *et al.* Exosomes are endogenous nanoparticles that can deliver biological information between cells. *Advanced Drug Delivery Reviews* **65**, 342–347 (2013).

120. Sharma, S. NANOANALYTICS OF EXTRACELLULAR VESICLES – Standards for isolation, characterization and reporting. *National Cancer Institute Hub* https://ncihub.org/resources/2034 (2017).

# Chapter 3. Impact of Isolation Method on the Biophysical Heterogeneity of Single Extracellular Vesicles

## 3.1 Abstract

Extracellular vesicles (EVs) have raised high expectation ns as a novel class of diagnostics and therapeutics. However, variabilities in EV isolation methods and the unresolved structural complexity of these biological-nanoparticles (sub-100nm) necessitate rigorous biophysical characterization of single EVs. Here, using atomic force microscopy (AFM) in conjunction with direct stochastic optical reconstruction microscopy (dSTORM), micro-fluidic resistive pore sizing (MRPS), and multi-angle light scattering (MALS) techniques, we compared the size, structure and unique surface properties of breast cancer cell-derived small EVs (sEV) obtained using four different isolation methods. AFM and dSTORM particle size distributions showed coherent unimodal and bimodal particle size populations isolated via centrifugation and immune-affinity methods respectively. More importantly, AFM imaging revealed striking differences in sEV nanoscale morphology, surface nano-roughness, and relative abundance of non-vesicles among different isolation methods. Precipitation-based isolation method exhibited the highest particle counts, yet nanoscale imaging revealed the additional presence of aggregates and polymeric residues. Together, our findings demonstrate the significance of orthogonal label-free surface characteristics of single sEVs, not discernable via conventional particle sizing and counts alone. Quantifying key nanoscale structural characteristics of sEVs, collectively termed ‘EV-nano-metrics’ enhances the understanding of the complexity and heterogeneity of sEV isolates, with broad implications for EV-analyte based research and clinical use.

## 3.2 Introduction

The emerging roles of secreted nanometer-sized exosomes or other extracellular vesicles (EVs),[1] in various physiological and pathological processes, has led to enormous interest in their potential clinical utility as cell-free biomarkers for cancer and other diseases.[2] Consequently, numerous efforts are underway to isolate, characterize, and optimize EVs.[3,4,5,6] However critical knowledge gaps still exist in our understanding of the biophysical properties of single EVs. There is no single “gold standard” method used for the isolation of EVs. Further, the current biophysical analyses of EVs typically encompass inadequate particle counting and size distribution determinations using various techniques. Together, to overcome the barriers due to the structural complexity (heterogeneity, small-to-large size ~30-1000nm) of these biological-nanoparticles, and isolation method dependent variabilities, improved biophysical analysis of EV isolates that complement and inform existing biomolecular analysis techniques is warranted prior to their subsequent use for reliable biomarkers or as therapeutics.

The small EV (sEV) isolates from commonly used methods such as ultracentrifugation (UC),[7] density ultracentrifugation (UCg),[8] size exclusion[9] or immuno-affinity (IA)[7,10] not only vary in purity and yield, but additionally demonstrate structural and biomolecular heterogeneity.[11,12] Further, precipitation (PT) based approaches represent an easy and fast approach for EV isolation which is mostly exploited by commercial kits. Several biophysical techniques estimate the particle counts and size distributions,[13–17] including nano-flow cytometry,[6,18] resistive pulse sensing,[19] nanoparticle tracking analysis,[20] and micro-fluidic approaches.[11,21–24] Yet, uncertainties and challenges exist with respect to reliable EV enumeration and comparisons of EV isolates obtained using different isolation techniques. Notably, most particle characterization approaches for evaluating EV isolates rely heavily upon particle size and count determinations but invariably fail to capture additional high-resolution characteristics such as structure, surface topography, adhesiveness or elasticity of single EVs which may offer novel orthogonal markers to precisely quantify the EV biophysics and nanoscale effects of isolation strategies used.

Structurally, electron microscopy (EM)[25] has provided a wealth of information on sEVs[12] given their nanoscale size range,[5,6,26] and while EM gives qualitative 3D information, quantitative computations on particle surfaces are challenging. Advancements in optical super-resolution imaging approaches further bring new capabilities to visualization of labeled sEVs. By contrast, atomic force microscopy (AFM)[27] enables deriving label-free, 3D, quantitative information of sEV isolates at sub-nanometer scale resolution.[28] Nevertheless, only a limited range of biophysical characteristics have been explored to date to assess the nanoscale scale impact of isolation methods on EV isolates. Here, using atomic force microscopy (AFM) in conjunction with direct stochastic optical reconstruction microscopy (dSTORM), micro-fluidic resistive pore sizing (MRPS), and multi-angle light scattering (MALS) techniques, we compared the size, structure and unique surface properties of breast cancer cell-derived sEVs obtained using different isolation methods. We identify novel biophysical properties to benchmark both the biophysical "quantity and quality" of EV isolates that largely remain obscured in the ensemble or other characterization techniques. Our findings reveal that the quantification of key biophysical parameters within sEV isolates collectively termed 'EV-nano-metrics' provides novel orthogonal markers to precisely quantify the nanoscale effects of isolation strategies at the single particle level. The findings hold significant potential implications for EV-based downstream applications particularly where molecular markers of sEVs are not established or not available.

### 3.3 Materials and Methods

**3.2.1 Cell culture and isolation of EVs:** To examine the biophysical characteristics of secreted exosomes, we first isolated exosomes from cultured cells that represent different metastatic potentials. We chose MCF-7 and MDA-MB-231 cells, two well-established breast cancer cell lines.[29,30] Also see Supplementary Information for characterization of cells and EVs. MCF-7 cells are tumorigenic but non-metastatic and represent the low metastatic potential. MDA-MB-231 cells are highly metastatic, with altered adhesion and motility properties.

**3.2.2 Small EV (sEV) isolation:** The MCF-7 and MDA-MB-231 (ATCC) breast cancer cell lines were cultured in Dulbecco's modified eagles medium (DMEM; Gibco, Thermo Fischer Scientific, Carlsbad CA) supplemented with 10% fetal bovine serum (FBS; Atlanta Biologicals), 100U/mL penicillin, and 100μg/mL streptomycin, in a 5% CO2 humidified atmosphere at 37°C. Cells were cultured in six 60 mm Petri dishes (Corning, CA) with FBS-originated-exosome-free media (as per protocol by Théry; FBS was ultra-centrifuged at 100 000 g for 2 hours at 4ºC, then filtered with a 0.22 µm sterile filter). After 48 hours incubation, the media containing sEVs were isolated. Total cell count was 2x10$^7$ and 24 mL of sEV-containing media was obtained. sEV isolation was performed as outlined in **Figure 1**. Successful sEV isolation was confirmed by electron microscopy, immune labeling (CD63, CD81 and CD9), and enrichment of sEV associated proteins determined using Mass Spectrometry (Supplemental Information).

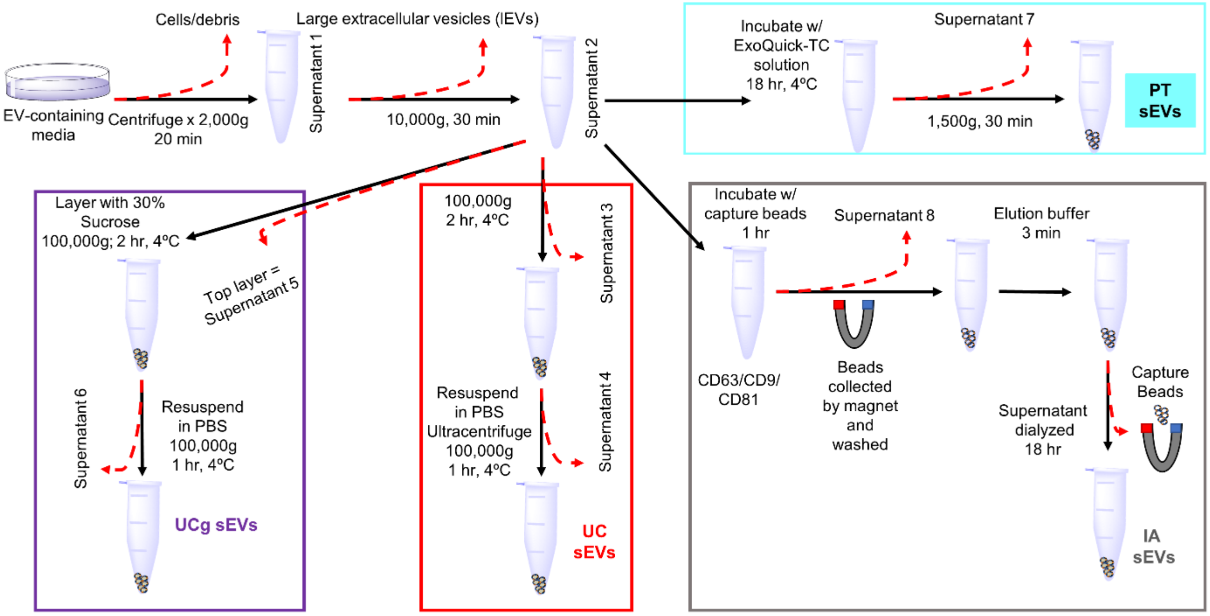

**Figure 1. Protocol used for simultaneous isolation of sEVs from breast cancer cells** (MCF7, MDA-MB-231) using four different isolation methods (i.e., ultracentrifugation- UC, sucrose density ultracentrifugation- UCg, Immune Affinity-IA, and polymeric precipitation-PT).

*Ultracentrifugation (UC):* As outlined in Fig 1, the sEV-containing media was centrifuged at 2,000g for 20 min at 4°C to remove cells and other debris. Subsequently, the isolated supernatant (supernatant 1) was centrifuged at 10,000g for 30 min at 4°C to remove large EVs and supernatant 2 was carefully isolated. To isolate sEVs, supernatant 2 was ultra-centrifuged at 100, 000g (type 70 Ti rotor in a Beckman Coulter Optima L-100 XP ultracentrifuge, Beckman

Coulter, Inc. USA) for 2 hours at 4°C and supernatant 3 was discarded. The pellet containing sEVs was re-suspended in 1 mL PBS, ultra-centrifuged at 100,000g for 1 hour at 4°C, and supernatant 4 was discarded. Purified sEVs were re-suspended in 1mL of PBS and stored at 4°C for subsequent imaging and analysis within < 1 week.

*Density gradient ultracentrifugation (UCg):* sEV isolation was performed using sucrose cushion as described previously.[7] Briefly, 0.5 ml 30% sucrose solution in PBS was carefully layered beneath 2.5 mL supernatant 2 in an ultracentrifuge tube, and was ultra-centrifuged at 100,000g using a type 70 Ti rotor in a Beckman Coulter Optima L-100 XP ultracentrifuge (Beckman Coulter, Inc., USA) for 2 hours at 4°C. The top 2.5 mL of solution was discarded, and the 30% sucrose bottom layer (0.5 mL) was collected, re-suspended in 3 mL PBS, and the mixture was spun at 100,000g for 1 hour at 4°C, and the resulting supernatant was discarded. Purified sEVs were re-suspended in 1mL of PBS and stored at 4°C (< 1 week).

*Immune affinity (IA): Immune affinity (IA):* As per previously described techniques,[31] magnetic immune affinity beads (JSR Life Science, Tokyo, Japan) coated with CD63, CD81 and CD9 antibodies were used to isolate sEVs from cell culture supernatants. Briefly, the sEV-containing media (200 µL) were incubated with 100 µL of capture beads for 60 min at room temperature (RT) with gentle shaking. Using magnets, beads were separated from the supernatant and washed three times using 0.5mL of wash buffer; beads were gently re-suspended in 50 µL of elution buffer, then incubated without mixing for 3 min at RT. Beads were magnetically removed and the supernatant was diluted to 1 mL with PBS and then dialyzed against PBS (using Slide-A-Lyzer Dialysis Cassette, Thermo Fisher Scientific, CA). Isolated sEVs were stored at 4°C and analyzed within a week.

*Precipitation (PT):* Commercial reagents for sEV isolation by PEG precipitation—ExoQuick (System Biosciences, CA) were used according to the manufacturer guidelines. Briefly, 200 µL of MCF7 or MDB-231 sEVs-containing media was combined with 1 mL ExoQuick-TC Solution in sterile Eppendorf tubes, mixed by inverting the tube several times, and incubated at 4°C for 18 hours. The solution was centrifuged at 1,500 g for 30 minutes in an Eppendorf MiniSpin Plus (Eppendorf, Germany). The supernatant was discarded, and the pellet was suspended in 1 mL PBS and stored at 4°C.

**3.2.3 AFM imaging, particle size, and single particle nano-roughness analysis:** sEV samples were incubated on freshly cleaved mica substrates (TedPella Inc, CA) for 5 min, washed with de-ionized water to remove any unbound EVs and air-dried overnight. Samples were imaged by Dimension Icon (Bruker Instruments, CA, USA) using the amplitude mode via TESP probes (Bruker Instruments, CA, USA) and images were recorded at 1024 samples per line at 1 Hz.

In our study, AFM imaging of isolated sEVs was performed at room temperature (22 ± 1 $^0$C) and ambient humidity ranging from 40-45 % relative humidity for all samples studied. Both temperature and humidity (with impact on factors such as capillary forces, friction, lubrication) play significant role in local-tip sample interactions. While the detailed influencing mechanisms of environment conditions such as temperature and humidity, were beyond the scope of these current investigations, the use of controlled environmental chamber enclosing the sample and the probe should be carefully considered, especially for metrological applications of AFM for EV analysis.

Image processing was done using SPIP (Image Metrology, Denmark) software to quantify particle diameters and counts using grain analysis function. For sEV yield calculation, images at sizes of 1 µm x 1 µm and 8 µm x 8 µm at a resolution of 1024 samples per line, at 1 Hz, were used. As per previously described for glioblastoma cell line derived EVs, to evaluate surface nano-roughness we employed 1 µm x 1 µm AFM topographic images.[32] The z (x, y) profiles, exported from AFM topographic scans were plane flattened to mitigate the effects of mostly curved nature of the nanoparticles. The apical regions (sub-tending typically 10% of the total area) were fitted with smooth spherical profiles, using least squares regression to obtain the average radius and center location for each nanoparticle (See supplemental information). Subsequently, the radial component of the spherical fit was subtracted from the distance between the center of the smooth profile and each (x, y, z) surface location. The resulting radial roughness amplitudes (**Figure 4**) were then used to calculate RMS for single sEVs.[33] Casein micelles from bovine milk without and without protease treatment were used to validate the quantitative nano-roughness analysis of single particles using AFM analysis.

**3.2.4 dSTORM image acquisition and data analysis:** *Sample preparation:* Isolated sEVs were labeled with 0.0025 mM carbocyanine dye (Vybrant DiO, Molecular Probes, OR) in PBS[34]. Samples were incubated over poly-lysine coated glass coverslips at RT for 20 mins and washed twice before imaging. The *d*STORM[35] acquisition was performed in an oxygen-scavenger buffer solution (ethanolamine, OxyFluor, and DL-Lactase adjusted to PH 7.5-8.5. A total internal reflection fluorescence microscope (Leica GSD SR, IL, US) with a 100× oil-immersion objective featuring a numerical aperture of 1.46 was used.[34] Lasers 405 nm and 642 nm were used for activation and excitation of DiO, respectively. For a single acquisition, 20,000 images of 32.56×32.56 µm were recorded with a cooled, electron multiplying charge-coupled device camera (Leica, IL, US) using 50 ms for exposure time. Calibration experiments were done with known size fluorescent beads (20 and 100 nm). EV-free samples [DiO in PBS] used as controls indicated no detectable (or <100 times lower) photo-blinking events in the far-red channel, suggesting the absence of non-specific fluorescence from the unbound dye. The images were recorded using Leica software (LAX Life Sciences).

**3.2.5 Micro-fluidic Resistive Pulse Sensing (MRPS):** For MRPS measurements, the supernatants and all solutions were filtered through a 0.2 *μ*m filter (Millipore) prior to use, as per the manufacturer's recommendation. Measurements were performed using an nCS1 machine (Spectradyne LLC, Torrance, CA) utilizing single use poly-dimethylsiloxane cartridges (TS-400) with pore size ranging from 65-400 nm (as per the manufacturer's manual). According to the manufacturer's recommendation, about three micro-liters of filtered sEV supernatants were used for each measurement and at least five-hundred individual events (particles) were assessed for analysis. Each cartridge was calibrated using standard polystyrene beads (100 ± 2 nm in size). Data were analyzed via nCS1 Data Analyzer (Spectradyne LLC, Torrance, CA) and employed similar user-defined transit time, signal-to-noise ratios and characteristics peak setting across all samples analyzed. The particle size and counts were determined using the average of triplicate measurements on two independent samples.

**3.2.6 Dynamic and multi-angle laser light scattering (MALS) for particle size determination:** Using Dyna Pro (Wyatt Technologies, Santa Barbara, CA), sixty micro-liters of sEV samples were analyzed in triplicates to obtain *R*g and absolute nanoparticle concentrations. Light scattering measurements were taken continuously at 18 angles between 15° and 151°; the captured data were integrated and analyzed using the DYNAMICS software (Wyatt Technologies).

### 3.4 Results

To quantify the nanoscale variations in sEV isolates obtained using different isolation methods (**Figure 1**) and cell types, key biophysical sEV-nano-metrics (namely particle morphology, counts, size distributions, surface roughness) were derived using multiple techniques (as summarized in **Table 1**).

**Table 1. Biophysical characteristics of sEV particles obtained from breast cancer cells, using different isolation methods**

| | | **AFM** | | | | | | **dSTORM** | | **MALS** | | **MRPS** | |
|---|---|---|---|---|---|---|---|---|---|---|---|---|---|
| Isolation Method | Cell line | Particle counts | Mean ± St dev. Particle diameter (nm) | | Average Particle Rms Surface Roughness (nm) | | | Mean ± Std dev. Particle diameter (nm) | | Median Particle diameter (nm) | | Median Particle diameter (nm) | |
| | | | *Pk 1* | *Pk 2* | *Mean* | *Std dev.* | *variance* | *Pk 1* | *Pk 2* | *Pk 1* | *Pk 2* | *Pk 1* | *Pk 2* |
| **UC** | MDA-MB-231 | 727 | 69.3 ± 18 | - | 0.23 | 0.03 | 0.001 | 74 ± 22 | - | 46.6 | - | < limit of detection | - |
| | MCF7 | 724 | 62.2 ± 6 | - | 0.26 | 0.04 | 0.001 | 70 ± 16 | - | | | | |
| **UCg** | MDA-MB-231 | 174 | 70.5 ± 18.9 | - | 0.42 | 0.01 | 3.8 X10$^{-4}$ | 70 ± 20 | - | 120.6 | - | - | - |
| | MCF7 | 163 | 71.0 ± 16 | - | 0.48 | 0.01 | 2.2X10$^{-4}$ | 76 ± 12 | - | | | | |
| **IA** | MDA-MB-231 | 628 | 82.0 ± 38 | 140 ± 8 | 0.71 | 0.09 | 0.008 | 54 ± 12 | 79 ± 10 | 99.7 | 213.4 | 65 | - |
| | MCF7 | 505 | 75.5 ± 22 | 135 ± 18 | 0.59 | 0.04 | 0.001 | 48 ± 12 | 86 ± 8 | | | | |
| **PT** | MDA-MB-231 | 1190 | 88.4 ± 36.4 | - | 3.5 | 0.37 | 0.13 | na | na | 99 | 210 | | |
| | MCF7 | 1515 | 100.4 ± 73.0 | - | 2.83 | 0.55 | 0.30 | | | | | | |

### 3.4.1 Comparative AFM based structural characterization of sEV isolates

First, we visualized sEVs from four different isolation methods (UC, UCg, IA, and PT as outlined in **Figure 1**) from well-established breast cancer cell lines[29] (described, as $sEV_{MCF7}$ and $sEV_{MDA-MB-231}$ respectively) at the single-particle level using AFM imaging under ambient conditions. The sEVs adsorbed on mica exhibit flat, roundly shaped morphologies. Simultaneously obtained AFM height (**Figure 2a**-*h*), amplitude (**Figure 2a**-*am*), and phase images (**Figure 2a**-*Ph*) emphasize differences in surface topography, standard deviation of topography, and contrast associated with biophysical properties such as elasticity respectively, among the different EV isolates are shown in corresponding panels (**Figure 2**; left to right: i-iii). As illustrated in **Figure 2**, the overall architecture observed in UC, UCg, and IA isolates reveal frequently occurring circular sub-100nm particle populations. However, in striking morphological contrast, PT isolates under identical imaging conditions showed relatively large and more heterogeneous particles (>100 nm) exhibiting irregular morphologies, as shown in representative images (**Figure 2a**). At this magnification, no significant substructures were detected on the EV surfaces (AFM-*h, -am*), however, distinct phase differences (AFM-*Ph*) observed for PT isolates indicate high likelihood of presence of polymeric residues on the nanoscale surface features of sEVs (**Figure 2**) compared to sEVs from other isolation methods (i.e., UC, UCg, IA).

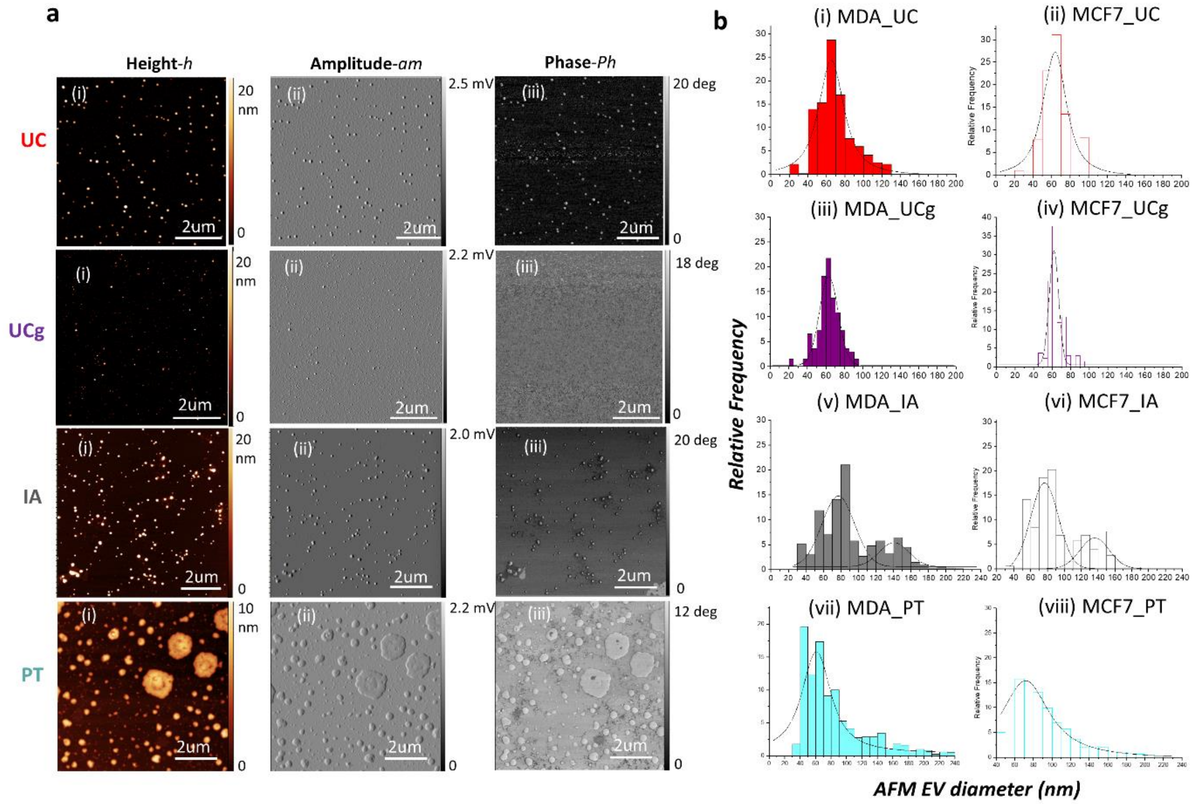

**Figure 2. AFM based structural characterization of single sEVs obtained from different isolation methods.** (a) AFM topographic height-*h* (i) showing 20 nm z range, amplitude-*am* (ii) and phase-*Ph* (iii) images for sEVs using UC, UCg, IA and PT isolations are shown from top to bottom respectively. AFM images exhibit least, and highest particle counts per micron square for UCg and PT isolation methods respectively. **(b)** Particle size distribution histograms with Gaussian fits obtained from AFM topography images. While minimal variance in particle size distributions was observed for UCg and largest variations for PT isolates, IA shows two distinct particle size populations, consistent among both cell types (MCF7 and MDA-MB-231), that were found to be significant based on two-way ANOVA (*$p < 0.05$).

Further, we determined AFM topography-based particle size (**Figure 2b**) and counts, *i.e.,* the number of particles imaged per square micron, in various sEV isolates (summarized in **Table 1**). Particles displaying a minimum threshold topographic height (>1nm), circularity with aspect ratio < 0.5, and a characteristic phase shift under amplitude-modulated AFM, were measured to minimize the influence of any soluble proteins or lipoprotein aggregates. Higher particle counts were noted for MDA-MB-231 compared to MCF7 cell-derived sEVs across three independent isolation techniques (UCg, UC, and IA). In addition to overall higher counts as described using different techniques,[5] and consistent with excess sEVs known to be shed by metastatic cancer cells, AFM particle analysis further resolved the distinct modalities of the size distributions among the four isolation methods. The UC and UCg methods exhibited unimodal distributions but minimal particle size variance, suggesting more homogeneously sized particle populations. The PT method exhibited unimodal but broader, heterogeneously size distributions. In contrast, the IA method exhibited more complex bimodal distributions showing two distinctly sized particle populations. These findings were consistent among sEVs derived from both cell types (i.e., $sEV_{MCF7}$ and $sEV_{MDA\text{-}MB\text{-}231}$) analyzed in three independent experiments. For each experimental run, cell culture supernatants from ~10^6 cells were split and processed in parallel for the four sEV isolation methods probed (**Figure 1**).

### 3.4.2 Particulate to the non-particulate ratio in sEV isolates

Second, we employ enhanced resolution AFM imaging as a means to structurally fingerprint and differentiate the sEV isolate components among the various isolates. Most nanoparticle sizing techniques extrapolate particle sizes assuming the spherical shape of the particles within sEV isolates, in addition to an inherent lack of sensitivity to detect additional non-vesicular structures that frequently exist on or associated with sEVs.[36] Here, from a structural standpoint, we used the high-resolution, label-free imaging analysis to biophysically characterize sEV isolates regardless of form and size. Not surprisingly, a systematic survey of sub-nanometer-resolution AFM images of sEVs obtained from different isolation methods revealed the co-existence of nano-sized particles, alongside additional varying filamentous structures albeit at varying abundance based on the isolation methods employed. A few such examples are illustrated in **Figure 3a.** Relative ratios of particles (ranging from 10-1000nm in size) and filamentous components detected in different sEV isolates are quantified in **Figure 3b.** The presence of relatively small but reproducible (experimental triplicates) populations of filaments and large (<500 nm in size) vesicles in UC, and IA sEV isolates for both cell types were noted, which were minimal in case of

UCg isolates. In contrast, PT isolates frequently showed large aggregates for both cell types that obscured further structural distinction of constituents within the complexes. The origins or functional relevance of identified co-isolates need to be further investigated. Nevertheless, high-resolution structural determination and quantification of non-vesicle components enabled orthogonal pre-analytical purity assessment criteria for sEV isolates, irrespective of the heterogeneous size, structure, or need for molecular labels.

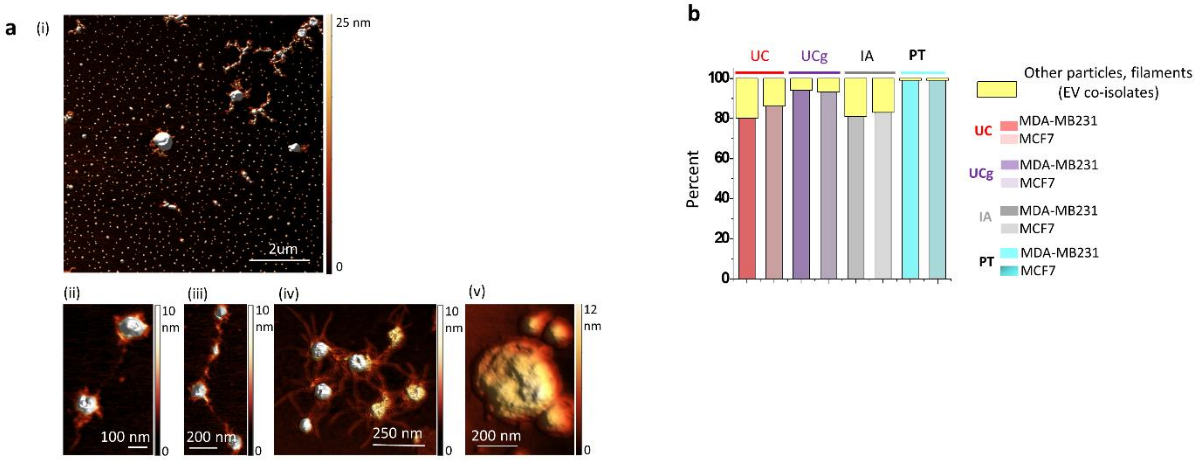

**Figure 3. Higher resolution structural analysis of sEV isolates obtained from different isolation methods show the presence of other particles, non-particles and filaments (together called EV co-isolates), at varying abundances**. **(a)** Higher resolution AFM images of sEV isolates reveals majority of round circular sEV particles but also structurally diverse sEV co-isolates illustrated in (i-v). Examples of nanoscale filamentous extensions and larger (>200nm) particles are shown **(b)** Relative abundances of sEV co-isolates from breast cancer cells varied among different isolation methods.

### 3.4.3 Surface nano-roughness of sEV isolates

Another striking yet underutilized biophysical feature of sEVs is their surface topography. Owing to the relatively large surface to volume ratios with key bio-interfacial roles, surface interactions of sEVs affect different biological and analytical processes.[37] Expanding on our previous findings,[31] we evaluated the topographic root-mean-square (RMS) nano-roughness of individual sEVs, representing the standard deviation of the height profile belonging to the surface asperities

(**Figure 4**). Our data demonstrate substantial isolation-method dependent variations in RMS nano-roughness of sEVs in breast cancer cells. The RMS nano-roughness of sEVs decreased in the order from PT> IA> UCg> UC isolates for both sEV$_{MCF7}$ and $_{s}$EV$_{MDA\text{-}MB\text{-}231}$ (**Figure 4; Table 1)**. Among these, the highest average roughness values of 3.1 nm and 2.9 nm were observed for PT isolated EV$_{MCF7}$ and EV$_{MDA\text{-}MB\text{-}231}$ respectively. Taken together, the sub-nm resolution mapping of the three-dimensional surface topology of individual sEVs offered a novel metrics to quantify the isolation-method influenced surface complexity of single sEVs with potential implications for biological and analytical behaviors of sEVs that primarily elude typical approaches confined to sEV particle size distribution analysis.

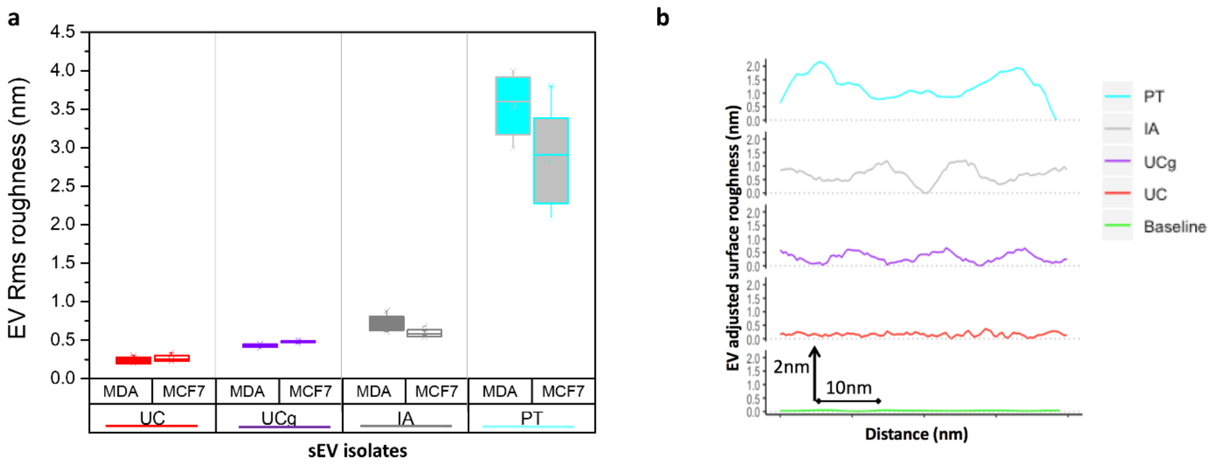

**Figure 4. Isolation method influences nanoscale surface topography of sEV isolates**. The impact of EV isolation methods on the surface topography of single sEVs was quantified as RMS roughness obtained from AFM topographic images (a) Assessment of RMS roughness of different isolates reveal greatest surface undulations in PT derived sEVs for both MCF7 and MDA-MB-231 cells (b) Representative roughness cross-sectional profiles illustrate variations in surface roughness of different sEVs. Over thirty single sEVs were analyzed for each cell type and isolation method under identical imaging conditions, resolution of topographic images obtained, using identical imaging probes.

### 3.4.4 Comparative optical, light scattering, and microfluidics-based resistive pulse sensing particle size measurements of sEV isolates

The localization super-resolution microscopy techniques now enable the resolution of light microscopy down to a few tens of nanometers- a scale closer to the typical lateral resolution of AFM when imaging sEVs. This provides an opportunity to contrast the impact of isolation methods on sEVs between scanning probe and optical detection techniques. Therefore, we exploited the resolution capabilities of direct stochastic optical reconstruction microscopy (dSTORM) imaging,[38] to further assess particle size distributions from all four sEV isolation methods and two cell lines studied. A representative reconstructed dSTORM image showing individual lipid labeled sEV nanoparticles is shown in **Figure 5.** The measured particle sizes (mean ± Std.dev) for sEVs are reported in **Table 1**. Overall, the UC and UCg isolation methods displayed unimodal Gaussian distributions for both $sEV_{MCF7}$ and $sEV_{MDA-MB-231}$ (**Figure 5b**). In contrast, the IA method showed bimodal size distributions for both the cell types measured i.e., $sEV_{MCF7}$ and $sEV_{MDA-MB-231,}$ respectively indicating the presence of two major sub-populations distinctly differing in particle sizes. Thus, the distinct EV subpopulations in case of IA method were independently noted from both AFM and dSTORM particle size distribution analyses. However, the bimodal particle size distributions were undetectable when probed using intensity-weighted light scattering MALS (**Figure 6a**) analysis run in parallel on similar samples, despite considerable shifts observed in particle distributions towards larger particle sizes (>200nm). We further assessed nanoparticle-sensing technologies based on resistance measurements, in an attempt to better resolve size distributions via particle-by-particle readouts, particularly in case of IA method derived sEV isolates, while requiring a lower sample concentration (~$10^7$ particles/mL) and smaller sample volume (~40 µL). To assess diverse sEV populations independent of light scatter measurements, we probed IA sEV isolates ($EV_{MCF7}$; and $EV_{MDA-MB-231}$) using MRPS[39] **(Figure 6b)**. The MRPS based particle concentrations, which correspond to the density of particles per mL of solution per nm of particle diameter (particles/mL*nm) are displayed in **Figure 6b**. The IA method exhibited four times higher particle counts in MDA-MB-231 compared to MCF7 sEV isolates. Very few particles were detected in UC isolates (shown in green curve in Fig. 6b). The higher number of particles noted in IA isolated $sEV_{MCF7}$ compared to $sEV_{MDA\text{-}MB\text{-}231}$ concurred with both AFM and dSTORM analysis. However, only a single peak particle size ~65 nm was observed on repeat MRPS analysis. Together, the multitude of particle size distribution findings on parallel EV isolates demonstrate that single particle AFM and dSTORM approaches enable better resolution and quantification of sEVs than MALS or MRPS alone, and to determine heterogeneity that presumably represent sEV sub-populations or other co-isolates.

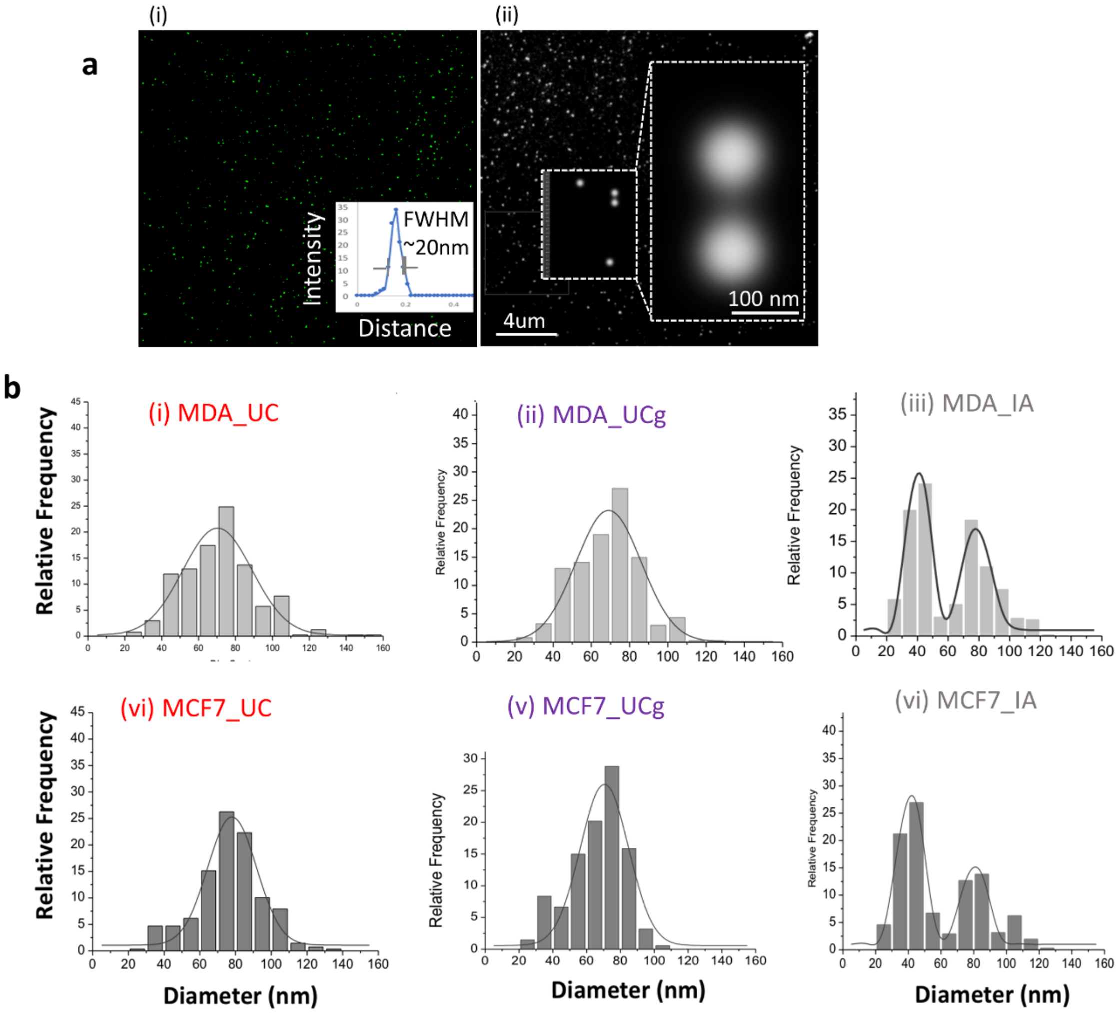

**Figure 5. The dSTORM based particle size characterization of single sEVs obtained from different isolation methods. (a)** Representative super-resolution dSTORM reconstructed image showing individual lipid labeled sEVs. (i) The full-width half-maximum (FWHM) of the fluorescence intensity distribution ~20nm obtained for dSTORM imaging, ~10 times better resolution compared to conventional fluorescence imaging (ii) Zoom-in and inset view showing two well-resolved sEVs,

~100nm in size. **(b)** Histograms showing the size distributions of particles with Gaussian fits obtained for various isolation methods and breast cancer cell types. *direct stochastic optical reconstruction microscopy.

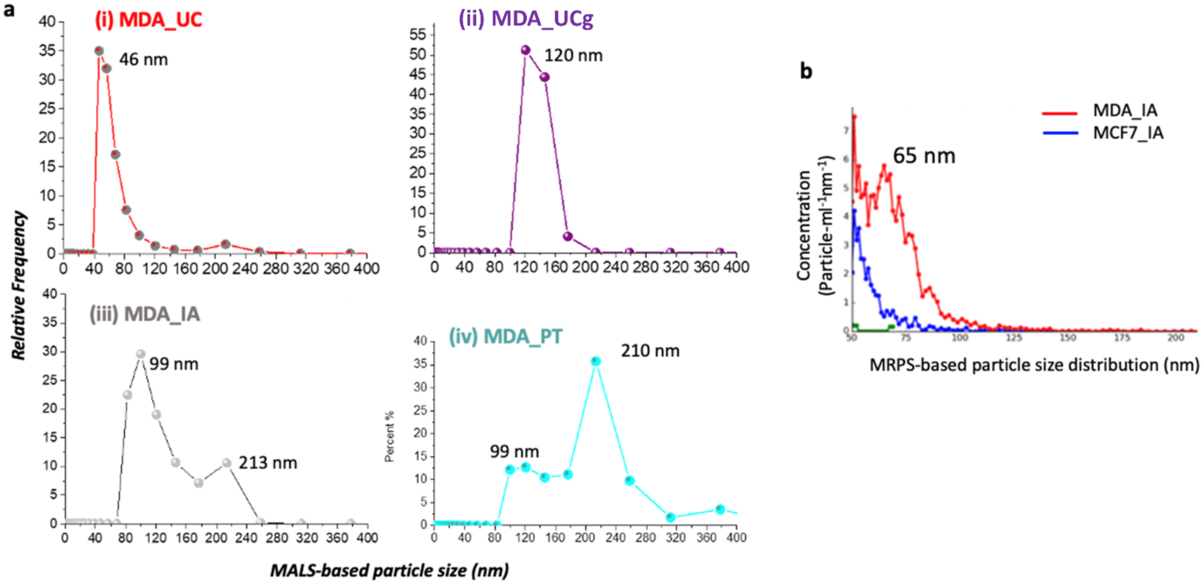

**Figure 6. Comparative particle size characterization of breast cancer cell sEVs isolates from different isolation methods** via **(a)** MALS based root-mean square radius (Rg) analysis showing averaged results from duplicate runs of each sample **(b)** Microfluidic resistive pulse sensing (MRPS) showed clear differences between particle concentrations and size distributions among MCF7 and MDA-MB-231 sEVs isolated using IA method within the 50-300nm size range.

### 3.5 Discussion

Isolation methods impact the biophysical characteristics of sEV isolates at the nanoscale level but elude detection when sEV isolates are assessed based on the particle counts and size distributions alone. Previous studies from our group and others demonstrated the applicability of correlative AFM, EM, and single-molecule force spectroscopy techniques as valuable tools for single sEV biophysical characterization.[28,32,40–42] Additionally, AFM based nanoscale imaging has been successfully applied to improve quantitative understanding of the impact of isolation methods on surface topographies of sEVs[31,43] with significant implications for downstream proteomic or transcriptomic assays.[8,44–46] When employing AFM based single particle analysis, the influence of key factors such as AFM imaging mode, magnitudes of imaging forces applied, and the choice of probes and substrates need to be carefully examined.[31,47–51] In this paper, we have conducted a systematic multi-dimensional comparative analysis (between cell types and isolation methods) of *in vitro* cancer cell-derived sEVs isolates using breast cancer cell models. Direct, high-resolution sEV surface features, quantification of sEV co-isolates, and particle size distributions using multiple sizing techniques were employed to improve our current understanding of nanoscale variations in single sEVs. In contrast to the biological fingerprint of sEVs, we focused on label-free biophysical fingerprinting of sEVs to evaluate the impact of isolation methods at the single-particle level.

Our study introduced nanoscale biophysical characteristics of label-free sEV isolates that differ among four main isolation methods. First, we show variable particle counts and sizes detected among different sEV isolation methods and cell types. The AFM based particle counts reduced from IA>UC>UCg for both $sEV_{MCF7}$ and $sEV_{MDA\text{-}MB\text{-}231}$ (**Table 1**). The highest particle counts were detected among PT isolates. However, when probed individually (**Figure 2**) the large (>150-200 nm in diameter) irregular structures and presence of polymeric residues observed via AFM imaging in these sEV isolates reflect the limitations and uncertainties associated with the quality of sEVs in the absence of direct structural mapping. More interestingly, the sEV isolates showed unimodal particle size distribution probabilities, except in the case of IA where the bimodal distributions of $sEV_{MCF7}$ and $sEV_{MDA\text{-}MB\text{-}231}$ were determined. The AFM-based bimodal distributions of IA derived $sEV_{MCF7}$ and $sEV_{MDA\text{-}MB\text{-}231}$ were found to be strikingly coherent with findings from the dSTORM particle size determinations, showing reproducible bimodal distributions among the sEV isolates. While MRPS noted about four-folds higher particle counts for $sEV_{MDA\text{-}MB\text{-}231}$ for IA isolates, the two size populations were not distinguished either via MALS or MRPS based analysis (**Figure 6**). While AFM mapped the surfaces of sEV isolates, dSTORM provided complementary information via lipid labeling to reveal particle sizes. The structural mapping of single sEVs thus provides a mechanism to de-convolute isolation method dependent sEV yields (quantity) that may be associated but not necessarily synonymous with greater isolation efficiency (quality).

Second, as a label-free approach, AFM based structural fingerprinting allowed differentiating the sEV isolate components (few nanometers-1000nm) among the various isolation methods studied. We envision that coupling of high-speed AFM-correlative dSTORM imaging of sEV isolates with machine learning algorithms[52] for multi-parametric data analysis, such as simultaneous sub-nanometer resolution structural mapping of single sEVs while spatially locating the fluorescently labeled molecules, offers exciting new directions in EV metrology.

Further, we illustrate the applicability of RMS roughness to the repertoire of single sEV biophysical characteristics to provide enhanced inter-methods comparisons of the residual impurities or co-isolates. The sub-nm resolution of z-height measurements in AFM enabled quantitative analysis of surface undulations, separate from the overall particle shapes or sizes. Topographic nano-surface roughness of single sEVs revealed significantly higher surface undulations in IA, and UCg isolates compared to UC. The RMS nano-roughness of sEVs decreased in the order from PT> IA> UCg> UC isolates for both $sEV_{MCF7}$ and $_{s}EV_{MDA\text{-}MB\text{-}231}$ (**Figure 4; Table 1)**. The greater than average roughness values of 3.1 nm and 2.9 nm observed for PT isolated $sEV_{MCF7}$ and $sEV_{MDA\text{-}MB\text{-}231}$ respectively compared to other methods, together with the visualization of aggregates in high-resolution images, strongly suggest that PT isolation results in localization of residual polymeric matrix on sEV surface[43]. Nonetheless, our findings demonstrate the usefulness of orthogonal particle shape/size independent sEV RMS roughness that may be particularly suitable for higher stringency assessment of sEVs isolated from various isolation methods. It is important to note that sEV surfaces are associated with numerous complexes interactions with proteins and other molecules within the dynamic environment (e.g., medium pH, ionic strength or biofluids). The quantitative determination of sEV surface characteristics such as RMS roughness may thus be vital for downstream applications of sEVs including as biomarkers, for functional assays or as therapeutics.

## 3.6 Conclusions

In summary, the rigorous biophysical characterization of sEVs is a crucial step for their use in diagnostic and clinical medicine. Our work highlights the limitations of comparing sEV isolates based primarily on particle counts and size distributions. Further, we show that correlative and spatially mapped particle metrics (topography, RMS roughness, particle ratios) add unique dimensions for more rigorous and reproducible biophysical characterization of sEVs, overcoming the limitations of conventional particle sizing approaches. The introduction of nanoscale structural characteristics of EV isolates represents a label-free, orthogonal framework to resolve differences in the heterogeneity and purity of sEVs from different cell types and isolation techniques. To the best of our knowledge, this is the first report on correlative scanning probe, optical super-resolution imaging in conjunction with commercial single particle counters to assess the nanoscale impact of sEV isolation methods. These results promise enhanced opportunities for quantitatively evaluating the biophysical quality and purity of sEV isolates that are urgently needed for more reliable sEV based research and clinical utility.

## 3.7 Supporting Information

### 3.7.1 Structural and biomolecular characterization of small EV isolates:

The following key measures were undertaken to minimize hitchhiker contaminations, from interfering with the analysis of EV isolation and characterizations in our study.

1. A prerequisite for any EV-related study is the use of contamination-free cells. Mycoplasma or other microbes can also release vesicles interfering with the purity and characterization of EVs. We employed rigorous testing of any contamination of the cells, cell culture media, other reagents, or chemicals. Cell cultures (ATCC) were regularly tested and found

negative for mycoplasma contamination using the culture medium (Mycoplasma broth, Millipore Sigma) and microscopic analysis.

2. In case of cell culture derived sEVs, of major importance are medium components, which are highly enriched in proteins and contain EVs, such as fetal bovine serum (FBS). Taking into account that sEVs present in FBS that reportedly co-isolate with cultured cells, we used EV depleted media. The EV-free media was also evaluated microscopically to validate the depletion of EV sized particles. Further, since a full depletion of EVs may not be possible, as per the recommendations of the ISEV guidelines (Thery et al. JEV 2018), we used fresh media not cultured with cells and a blank buffer as controls. Based on MALS and AFM particle sizing, no particulate materials within the size range of sEVS were detectable in these controls.
3. Consistent cell seeding protocols and cell viability tests were used across multiple EV isolation runs to ensure the reproducibility and quality of the isolated sEVs. All chemicals, buffers and other reagents used were molecular grades.

Additional References:

1. Théry, C. et al., Minimal Information for Studies of Extracellular Vesicles 2018 (MISEV2018): A Position Statement of the International Society for Extracellular Vesicles and Update of the MISEV2014 Guidelines. *Journal of Extracellular Vesicles* **2018**, *7* (1), 1535750. https://doi.org/10.1080/20013078.2018.1535750.
2. Kornilov, R. et al., Efficient ultrafiltration-based protocol to deplete extracellular vesicles from fetal bovine serum. *J. Extracell. Vesicles* **2018**, 7.
3. Thierry, C.; Amigorena, S.; Raposo, G.; Clayton, A. Isolation and Characterization of Exosomes from Cell Culture Supernatants. *Curr. Protoc. Cell Biol.* **2006**, 3, 1–29.

The sEV samples were vitrified to preserve the native structure of the samples. Freshly prepared samples were plunge frozen in liquid propane using a Vitrobot (FEI). Cryo-EM was performed on TF20 High-Resolution CryoEM (FEI). The tetraspanin assay, utilizing common sEV surface marker antibodies immobilized on substrates- CD81, CD63 and CD9 was used to confirm the isolation of sEVs obtained from breast cancer cells.

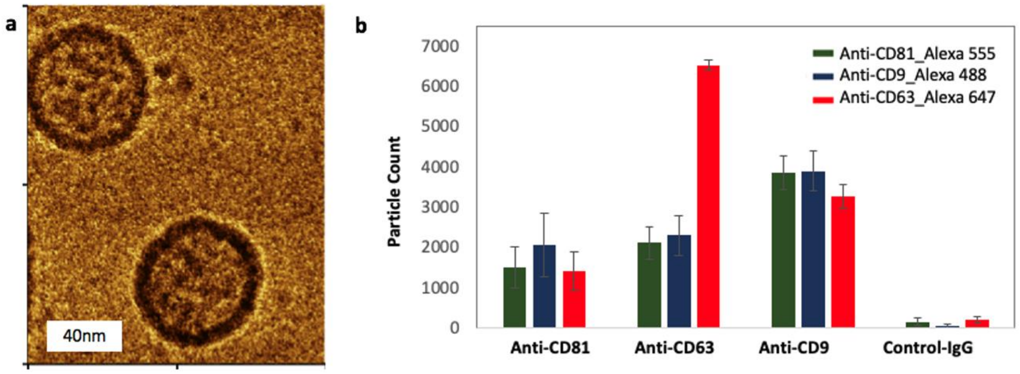

**Figure S1. Complementary sEV characterization**. (a) The cryo-EM reveals lipid bilayer membrane enclosed vesicle structure of isolated sEVs (b) Graph shows particle counts (sEVs) bound via various validated capture antibodies using ExoView technology (NanoView Biosciences). Error bars show standard deviations of mean particle counts.

### 3.7.2. Mass Spectrometry Proteomic Analysis of sEV isolates

We employed a shotgun proteomics workflow in which isolated sEVs were lysed, digested by sequential addition of lys-C and trypsin proteases, fractionated online using reversed phase chromatography and analyzed by tandem MS on a Thermofisher Fusion Lumos mass spectrometer. Data analysis was conducted using an in-house Galaxy-based bioinformatics pipeline utilizing MS-GF+, percolator, and Fido for database searching and filtering (<1% FDR at both peptide and protein levels using decoy database approach). Our sEV isolates were highly-enriched for EV proteins (i.e. 203 proteins annotated with the GO term “extracellular exosome” corresponding to an enrichment p-value of 2.8E-89) as well as membrane proteins (i.e. 104 proteins annotated with GO term “membrane” corresponding to an enrichment p-value of 1.7E-33).

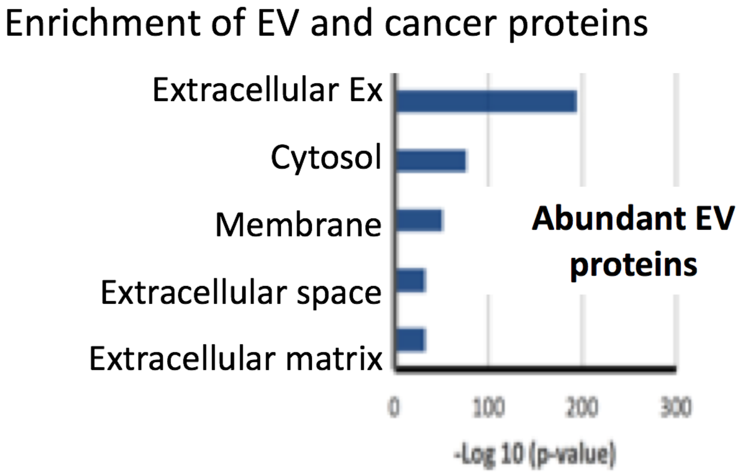

**Figure S2. The breast cancer cell culture derived sEV isolates showed enrichment of sEV and cancer proteins in Mass Spectrometric analysis.**

### 3.7.3: dSTORM single-particle averaging

The spatial alignment and averaging of localization data from measurements of multiple structurally identical particles permitted a dataset to be obtained with much increased signal-to-noise ratio. Particle averaging analysis was applied to super-resolution image analysis. Reconstruction and data processing of recorded sEV images was performed using Fiji and QuickPALM software. The *d*STORM images were reconstructed with a pixel size of 10 nm. Output text files containing a list of the x and y coordinates and the precision of all detected molecules in the time-series, were used to further assess variations in the average particle sizes between sEV samples. To increase the efficiency and accuracy of our dSTORM analysis, we performed a quality check to discard all signals not corresponding to individual nanoparticles. We excluded very small objects (likely single fluorescent or soluble lipid molecules) and very big objects (likely aggregates of multiple nanoparticles), and high aspect ratio objects (e.g., dimers of nanoparticles, microvesicles).

Additional References:

1. Sigal, Y. M., Zhou, R. & Zhuang, X. Visualizing and discovering cellular structures with super-resolution microscopy. *Science* 361, 880–887 (2018).
2. Henriques, R. et al. QuickPALM: 3D real-time photoactivation nanoscopy image processing in ImageJ. *Nature Methods* 7, 339–340 (2010).

### 3.7.4: STED imaging

A Leica TCS SP5 STED confocal system (Leica Microsystems, Wetzlar, Germany), equipped with a 640-nm pulsed diode laser (PicoQuant, Berlin, Germany) was used for excitation combined with a pulsed ultrafast Ti:sapphire infrared laser (Mai Tai Broadband; Spectra-Physics, Santa Clara, California), fully tunable from 710 nm to 990 nm. The sEVs were fixed and CD63 stained with Abberior STAR 635 anti- CD63 (Abberior® Dyes | Sigma-Aldrich). Images were filtered and flattened using SPIP 5.8 Image Metrology, Horsholm, Denmark. STED imaging was used as a comparative technique in parallel to the dSTORM analysis.

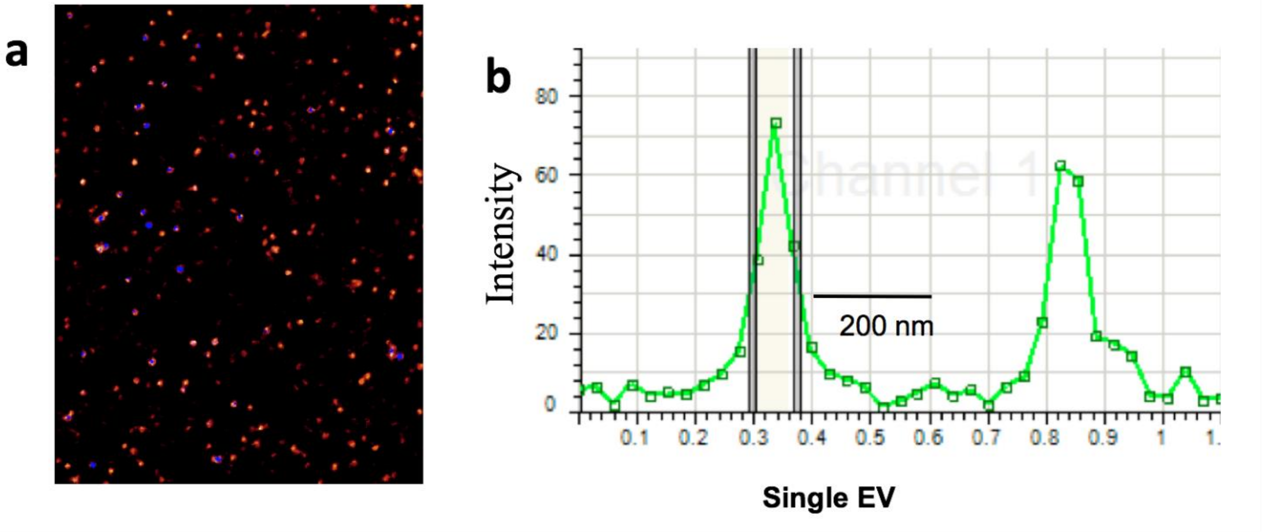

**Figure S3. The dSTORM measurements on sEV isolates were validated using STED imaging in parallel**. (a) STED imaging of sEV isolates (b) Representative line profile indicating the resolution of STED imaging enabling the resolution of single particles in sEV isolates.

### 3.7.5: Biophysical characteristics of sEV particles obtained from MCF-10A breast cancer cells

Compared to MCF-7 and MDA-MB-231 small EVs, the measured size for MCF-10A derived sEVs were larger, and roughly two-folds less abundant based on AFM and MALS data (**Table S1**).

**Table S1. Biophysical characteristics of sEV particles obtained from MCF-10A breast cancer cells.**

| | | **AFM** | | **MALS** |
|---|---|---|---|---|
| **Isolation Method** | **Cell line** | **Particle counts** | **Mean ± St dev.<br>Particle diameter (nm)** | **Median<br>Particle diameter (nm)** |
| **UC** | MCF-10A | 325 | 80.0 ± 8.3 | 78.0 |
| **UCg** | MCF-10A | 180 | 77.0 ± 1.6 | 74.2 |

### 3.7.6: AFM topographic scans show differences in residual particulates among blank controls from polymeric (PT) solution and immune-affinity (IA) beads method.

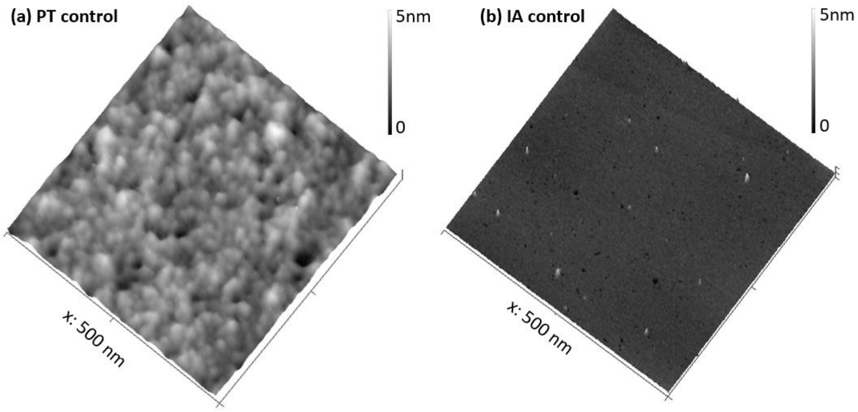

**Figure S4. Differences in residual in residual particulates among blank controls from polymeric (PT) solution and immune-affinity (IA) beads sEV isolation methods**.

### 3.7.7: Roughness profiles of single EVs

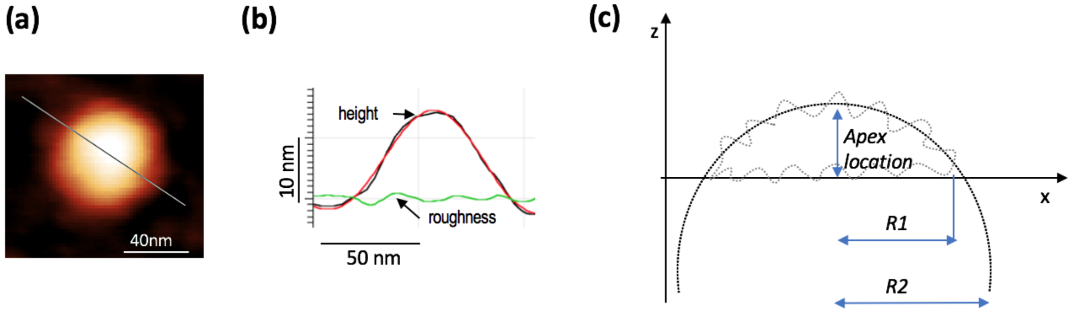

**Figure S5. AFM based roughness analysis of single sEVs** (a) AFM topographic image of single sEV and (b) cross section profiles. A quantitative surface roughness (green line) analysis of EVs involves subtracting the surface topography from the spherical fit. (c) A two-dimensional schematic illustration of a non- linear least squares fit of an AFM EV particle topography to a spherical shape showing radius of the sphere fit (R2), the apex, and radius of the particle (R1) at z=0, after reduction of the substrate background roughness.

### Additional References:

1. Woo, J.; Sharma, S.; Gimzewski, J. The Role of Isolation Methods on a Nanoscale Surface Structure and Its Effect on the Size of Exosomes. *J Circ Biomark* **2016**, *5*. https://doi.org/10.5772/64148.
2. Hsu, C.-P.; Ramakrishna, S. N.; Zanini, M.; Spencer, N. D.; Isa, L. Roughness-Dependent Tribology Effects on Discontinuous Shear Thickening. *PNAS* **2018**, *115* (20), 5117–5122. https://doi.org/10.1073/pnas.1801066115.

### 3.8 References

1. Théry, C. Exosomes: secreted vesicles and intercellular communications. *F1000 Biol Rep* **3**, (2011).
2. Xu, R. *et al.* Extracellular vesicles in cancer — implications for future improvements in cancer care. *Nature Reviews Clinical Oncology* **15**, 617 (2018).
3. Théry, C. *et al.* Minimal information for studies of extracellular vesicles 2018 (MISEV2018): a position statement of the International Society for Extracellular Vesicles and update of the MISEV2014 guidelines. *Journal of Extracellular Vesicles* **7**, 1535750 (2018).
4. Jeppesen, D. K. *et al.* Reassessment of Exosome Composition. *Cell* **177**, 428-445.e18 (2019).
5. Zhang, H. *et al.* Identification of distinct nanoparticles and subsets of extracellular vesicles by asymmetric flow field-flow fractionation. *Nat. Cell Biol.* **20**, 332–343 (2018).
6. Choi, D., Spinelli, C., Montermini, L. & Rak, J. Oncogenic Regulation of Extracellular Vesicle Proteome and Heterogeneity. *PROTEOMICS* **19**, 1800169 (2019).
7. Théry, C., Amigorena, S., Raposo, G. & Clayton, A. Isolation and characterization of exosomes from cell culture supernatants and biological fluids. *Curr Protoc Cell Biol* **Chapter 3**, Unit 3.22 (2006).
8. Tauro, B. J. *et al.* Comparison of ultracentrifugation, density gradient separation, and immunoaffinity capture methods for isolating human colon cancer cell line LIM1863-derived exosomes. *Methods* **56**, 293–304 (2012).
9. Böing, A. N. *et al.* Single-step isolation of extracellular vesicles by size-exclusion chromatography. *J Extracell Vesicles* **3**, (2014).
10. Bobrie, A., Colombo, M., Krumeich, S., Raposo, G. & Théry, C. Diverse subpopulations of vesicles secreted by different intracellular mechanisms are present in exosome preparations obtained by differential ultracentrifugation. *Journal of Extracellular Vesicles* **1**, 18397 (2012).

11. Maas, S. L. N. *et al.* Possibilities and limitations of current technologies for quantification of biological extracellular vesicles and synthetic mimics. *J Control Release* **200**, 87–96 (2015).
12. Rupert, D. L. M., Claudio, V., Lässer, C. & Bally, M. Methods for the physical characterization and quantification of extracellular vesicles in biological samples. *Biochimica et Biophysica Acta (BBA) - General Subjects* **1861**, 3164–3179 (2017).
13. Van Deun, J. *et al.* EV-TRACK: transparent reporting and centralizing knowledge in extracellular vesicle research. *Nature Methods* **14**, 228–232 (2017).
14. Pol, E. van der *et al.* Particle size distribution of exosomes and microvesicles determined by transmission electron microscopy, flow cytometry, nanoparticle tracking analysis, and resistive pulse sensing. *Journal of Thrombosis and Haemostasis* **12**, 1182–1192 (2014).
15. Khatun, Z., Bhat, A., Sharma, S. & Sharma, A. Elucidating diversity of exosomes: biophysical and molecular characterization methods. *Nanomedicine* **11**, 2359–2377 (2016).
16. Pol, E. van der, Böing, A. N., Gool, E. L. & Nieuwland, R. Recent developments in the nomenclature, presence, isolation, detection and clinical impact of extracellular vesicles. *Journal of Thrombosis and Haemostasis* **14**, 48–56 (2016).
17. Pol, E. V. D. *et al.* Optical and non-optical methods for detection and characterization of microparticles and exosomes. *Journal of Thrombosis and Haemostasis* **8**, 2596–2607 (2010).
18. Morales-Kastresana, A. *et al.* High-fidelity detection and sorting of nanoscale vesicles in viral disease and cancer. *Journal of Extracellular Vesicles* **8**, 1597603 (2019).
19. Weatherall, E. & Willmott, G. R. Applications of tunable resistive pulse sensing. *Analyst* **140**, 3318–3334 (2015).
20. Gardiner, C., Ferreira, Y. J., Dragovic, R. A., Redman, C. W. G. & Sargent, I. L. Extracellular vesicle sizing and enumeration by nanoparticle tracking analysis. *J Extracell Vesicles* **2**, (2013).

21. Arraud, N. *et al.* Extracellular vesicles from blood plasma: determination of their morphology, size, phenotype and concentration. *Journal of Thrombosis and Haemostasis* **12**, 614–627 (2014).
22. Chandler, W. L., Yeung, W. & Tait, J. F. A new microparticle size calibration standard for use in measuring smaller microparticles using a new flow cytometer. *Journal of Thrombosis and Haemostasis* **9**, 1216–1224 (2011).
23. Kormelink, T. G. *et al.* Prerequisites for the analysis and sorting of extracellular vesicle subpopulations by high-resolution flow cytometry. *Cytometry Part A* **89**, 135–147 (2016).
24. Pasalic, L. *et al.* Enumeration of extracellular vesicles by a new improved flow cytometric method is comparable to fluorescence mode nanoparticle tracking analysis. *Nanomedicine: Nanotechnology, Biology and Medicine* **12**, 977–986 (2016).
25. Pan, B. T., Teng, K., Wu, C., Adam, M. & Johnstone, R. M. Electron microscopic evidence for externalization of the transferrin receptor in vesicular form in sheep reticulocytes. *J Cell Biol* **101**, 942–948 (1985).
26. Chiang, C. & Chen, C. Toward characterizing extracellular vesicles at a single-particle level. *Journal of Biomedical Science* **26**, 9 (2019).
27. Binnig, G., Quate, C. F. & Gerber, Ch. Atomic Force Microscope. *Phys. Rev. Lett.* **56**, 930–933 (1986).
28. Sharma, S. *et al.* Structural-Mechanical Characterization of Nanoparticle Exosomes in Human Saliva, Using Correlative AFM, FESEM, and Force Spectroscopy. *ACS Nano* **4**, 1921–1926 (2010).
29. Neve, R. M. *et al.* A collection of breast cancer cell lines for the study of functionally distinct cancer subtypes. *Cancer Cell* **10**, 515–527 (2006).
30. Nagaraja, G. M. *et al.* Gene expression signatures and biomarkers of noninvasive and invasive breast cancer cells: comprehensive profiles by representational difference analysis, microarrays and proteomics. *Oncogene* **25**, 2328–2338 (2006).

31. Woo, J., Sharma, S. & Gimzewski, J. The Role of Isolation Methods on a Nanoscale Surface Structure and its Effect on the Size of Exosomes. *J Circ Biomark* **5**, (2016).
32. Sharma, S., Das, K., Woo, J. & Gimzewski, J. K. Nanofilaments on glioblastoma exosomes revealed by peak force microscopy. *J R Soc Interface* **11**, (2014).
33. Hsu, C.-P., Ramakrishna, S. N., Zanini, M., Spencer, N. D. & Isa, L. Roughness-dependent tribology effects on discontinuous shear thickening. *PNAS* **115**, 5117–5122 (2018).
34. Heilemann, M. *et al.* Subdiffraction-Resolution Fluorescence Imaging with Conventional Fluorescent Probes. *Angewandte Chemie International Edition* **47**, 6172–6176 (2008).
35. van de Linde, S. *et al.* Direct stochastic optical reconstruction microscopy with standard fluorescent probes. *Nature Protocols* **6**, 991–1009 (2011).
36. Tkach, M., Kowal, J. & Théry, C. Why the need and how to approach the functional diversity of extracellular vesicles. *Philos Trans R Soc Lond B Biol Sci* **373**, (2018).
37. Buzás, E. I., Tóth, E. Á., Sódar, B. W. & Szabó-Taylor, K. É. Molecular interactions at the surface of extracellular vesicles. *Semin Immunopathol* **40**, 453–464 (2018).
38. Hell, S. W. Far-field optical nanoscopy. *Science* **316**, 1153–1158 (2007).
39. Fraikin, J.-L., Teesalu, T., McKenney, C. M., Ruoslahti, E. & Cleland, A. N. A high-throughput label-free nanoparticle analyser. *Nature Nanotechnology* **6**, 308–313 (2011).
40. Yuana, Y. *et al.* Atomic force microscopy: a novel approach to the detection of nanosized blood microparticles. *J. Thromb. Haemost.* **8**, 315–323 (2010).
41. Ashcroft, B. A. *et al.* Determination of the size distribution of blood microparticles directly in plasma using atomic force microscopy and microfluidics. *Biomed Microdevices* **14**, 641–649 (2012).
42. Siedlecki, C. A., Wen Wang, I., Higashi, J. M., Kottke-Marchant, K. & Marchant, R. E. Platelet-derived microparticles on synthetic surfaces observed by atomic force microscopy and fluorescence microscopy. *Biomaterials* **20**, 1521–1529 (1999).

43. Paolini, L. *et al.* Residual matrix from different separation techniques impacts exosome biological activity. *Scientific Reports* **6**, 23550 (2016).
44. Van Deun, J. *et al.* The impact of disparate isolation methods for extracellular vesicles on downstream RNA profiling. *J Extracell Vesicles* **3**, (2014).
45. Varga, Z. *et al.* Towards traceable size determination of extracellular vesicles. *J Extracell Vesicles* **3**, (2014).
46. Lozano-Ramos, I. *et al.* Size-exclusion chromatography-based enrichment of extracellular vesicles from urine samples. *J Extracell Vesicles* **4**, (2015).
47. Thomson, N. H. Imaging the substructure of antibodies with tapping-mode AFM in air: the importance of a water layer on mica. *Journal of Microscopy* **217**, 193–199 (2005).
48. Dokukin, M. E., Guz, N. V., Gaikwad, R. M., Woodworth, C. D. & Sokolov, I. Cell Surface as a Fractal: Normal and Cancerous Cervical Cells Demonstrate Different Fractal Behavior of Surface Adhesion Maps at the Nanoscale. *Phys. Rev. Lett.* **107**, 028101 (2011).
49. Sharma, S., Gillespie, B. M., Palanisamy, V. & Gimzewski, J. K. Quantitative Nanostructural and Single-Molecule Force Spectroscopy Biomolecular Analysis of Human-Saliva-Derived Exosomes. *Langmuir* **27**, 14394–14400 (2011).
50. Vorselen, D., MacKintosh, F. C., Roos, W. H. & Wuite, G. J. L. Competition between Bending and Internal Pressure Governs the Mechanics of Fluid Nanovesicles. *ACS Nano* **11**, 2628–2636 (2017).
51. Calò, A. *et al.* Force measurements on natural membrane nanovesicles reveal a composition-independent, high Young's modulus. *Nanoscale* **6**, 2275–2285 (2014).
52. Ito, K. *et al.* Host Cell Prediction of Exosomes Using Morphological Features on Solid Surfaces Analyzed by Machine Learning. *J. Phys. Chem. B* **122**, 6224–6235 (2018).

# Chapter 4. A Review of the Biomechanical Properties of Single Extracellular Vesicles

## 4.1 Abstract

Extracellular vesicles (EVs) are a unique, heterogeneous class of biological nanoparticles secreted by most cells. As potential a class of novel diagnostics and therapeutics, the physio-chemical characterization as well as the biomolecular composition of EVs are widely investigated. However, there is emerging evidence suggesting that biomechanical analysis of lipid-bilayer membrane-bound single EVs may provide key insights into their biological structure, biomarker functions, and potential therapeutic functions. In this review, we focus on the unique biomechanical properties of single EVs such as elasticity, stiffness, and deformability. We compare common indentation models used in atomic force microscopy (AFM)-based biomechanical analysis of EVs, as well as the benefits and drawbacks of each model encompassing the heterogeneous EV sub-populations—mainly the small EVs (or exosomes). Next, we discuss high-throughput approaches to determine the biomechanical landscape of EVs that may overcome some of the challenges associated with the accurate determination of particle sizes and particle-by-particle indentations. Finally, we highlight exciting new opportunities for EV biomechanical fingerprinting emanating from machine learning capabilities. In particular, we propose multi-parametric AFM structure-mechanical analysis to further advance label-free, orthogonal biophysical understanding of EVs beyond biomolecular or particle size analysis, with significant implications for research and clinical use.

## 4.2 Introduction: The diverse extracellular vesicle (EV) landscape

Extracellular vesicles (EVs) are biologically-produced nanoparticles comprised of a lipid bilayer membrane surrounding internal DNA, RNA, protein, and lipid cargo.[1,2] These nanovesicles are known to participate in long-range intracellular communication—though the specific mechanisms underlying this long-range communication are still under investigation.[3] EVs have been implicated in the propagation of diseases such as cancer,[4–6] HIV,[7,8] and Alzheimer's;[9] and are known to carry molecular signatures linked to their parent cells.[3] EVs are readily available from biofluids (e.g.

urine,[10] blood,[11] saliva,[12,13] cerebrospinal fluid,[14] amniotic fluid[15]) that makes liquid biopsy an attractive option for EV-based diagnostics.[1] Therapeutically, EVs are attractive potential drug delivery agents due to the ease of uptake by target cells and their ability to pass the blood-brain barrier.[16] Mesenchymal stem cell (MSC)-derived EVs show therapeutic benefits for cardiovascular disease in multiple studies.[17] Clinical trials are also underway to investigate the anti-inflammatory therapeutic effects of EVs in alleviating acute respiratory distress syndrome (ARDS) in patients with SARS-CoV-2.[18–20] To date over 4400 published research articles have been reported on EVs. The global EV-based diagnostics and therapeutics market is projected to reach USD 264 million by 2024. Despite the exponential rise in biomedical potential, one of the main obstacles currently hampering the utility of EVs for functional and clinical studies is the lack of well-characterized EVs.

EVs have heterogeneous subpopulations, as displayed in **Figure 1**. EVs vary in size, interior cargo, lamellarity, biogenesis, and more.[1,21–23] The small EVs such as exosomes are lipid bilayer membrane particles with subpopulations varying in size from roughly 40-160 nm.[1] Larger EVs include micron-size range particles such as the multivesicular bodies,[24,25] microvesicles,[26] apoptotic bodies,[27] migrasomes,[28,29] exophers,[30] and the large oncosomes (up to 10 µm in size).[31–33] The discovery of exomeres, a sub-50 nm non-membranous nanoparticle population with distinct molecular cargo further augments the complex and heterogeneous extracellular vesicle landscape.[34]

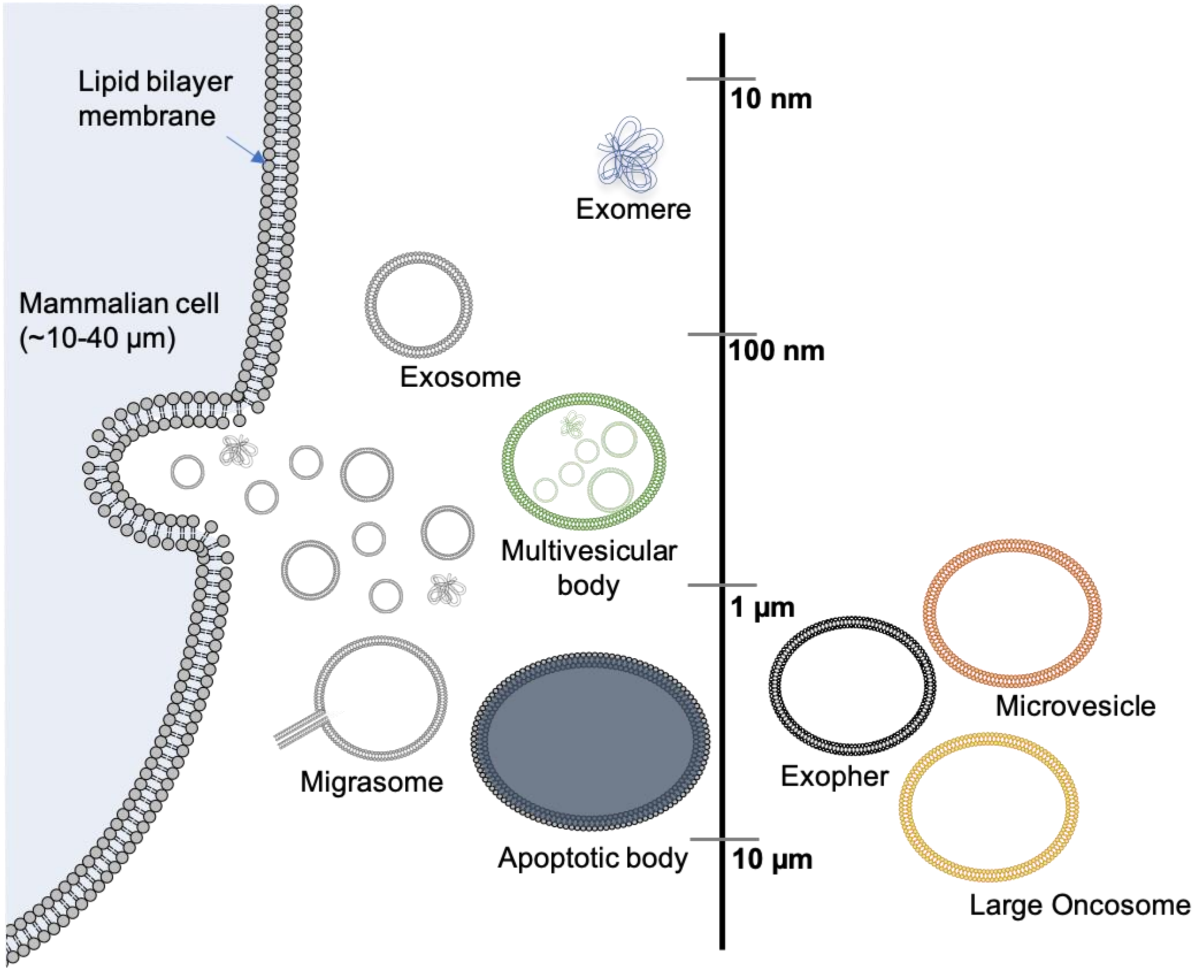

**Figure 1. The structural landscape of extracellular particles:** EVs and other particles released from a typical mammalian cell vary in size, content, and biomolecular composition. While several populations may overlap in size (and content), typically, exomeres are the smallest sized (~35nm) particle populations and are non-membranous particles, i.e., known to be devoid of lipid-bilayer membranes. Exosomes, 30-120 nm particles, possess a lipid bilayer membrane enclosing the protein, DNA, RNA, and lipid cargo. Exosomes are produced through endosomal pathways involving the formation of multivesicular bodies that fuse with the plasma membrane. The multivesicular bodies (~100-600 nm) are bilayer membrane-bound particles containing smaller exosomes and other EVs inside. Microvesicles bud (mostly < 1 µm) directly from the plasma membrane. Cancer cells also secrete large oncosomes (1-10 µm) containing oncogenic material. In addition, the apoptotic bodies (1-5 µm) are membranous particles containing discarded cellular components and may carry large cellular organelles including nuclear fragments. Migrasomes (up to 3 µm in size) have also been reported that form as large vesicle-like structures on retraction fibres of migrating cells. Exophers (~ 4 µm) contain protein aggregates and organelles are known to be released by neurons in *C. elegans*.

To quantify and structurally probe this diverse landscape of various EV sub-populations, several characterization techniques have been applied.[35–37] Structurally, though the sub-200 nm diameter of most EVs precludes the use of many optical microscopies to image EVs and necessitates the use of nanoscale methods such as electron microscopy (EM), direct stochastic optical reconstruction microscopy,[38] and atomic force microscopy (AFM) to successfully image EVs at the single vesicle level.[2,37] So far, little research has focused on quantifying the biophysical characteristics of single EVs beyond size, counts, and biomolecular composition assessments. In particular, the analysis of mechanical properties of individual EVs further provides key label-free insights into the biophysical variations among EV sub-populations, and ultimately their biological role[39] and potential biomarker functions.[13,40] This review seeks to explore the current state of the art in biomechanical characterization techniques applied to EVs, and the role of label-free, multi-parametric, structural-mechanical properties for advancing EV-based diagnostics and therapeutics. In this review, we primarily focus on lipid bilayer membrane-limited small EVs such as exosomes, which constitute the most commonly studied EV sub-populations to date.

### 4.3 Beyond Size: The Relevance of EV Mechanical Properties

Mechanical properties refer to the mechanical characteristics of materials (synthetic or biological such as tissues, cells, or sub-cellular EVs) under different environments and various external loads. Different materials exhibit different mechanical properties. Within the biological milieu, the mechanical properties of nanoparticles (synthetic or natural) affect their uptake by cells, life in circulation, tissue targeting, and release of biomolecules.[41,42] Likewise, in its lifetime, a biological nanoparticle such as an EV can be exposed to multiple mechanical forces including but not limited to their intercellular and extracellular transport, internalization and externalization by cells, and adhesion to surfaces.[39,43–46] These various stresses will deform the EV, and the extent of deformation will be affected by the unique EV's mechanical properties. However, before delving into the determination of the mechanical properties of EVs, we first briefly describe the main mechanical characteristics when considering the mechanical properties of EVs (as well as liposomes and other similarly sized nanovesicles) such as mechanical stiffness, elasticity, and other closely related properties that are most relevant. These properties are summarized in **Table 1** and described below.

**Table 1. Summary of the key mechanical properties related to unique EVs mechanical characteristics.**

| Property | Symbol | Units | Definition | Features | References |
|---|---|---|---|---|---|
| Mechanical Stiffness | $K$ | N $m^{-1}$ | • The resistance to deformation caused by an applied force | • Extrinsic property<br>• Dependent on EV geometry<br>• Obtained from linear fit on force-indentation curve | 59 |
| Young's Modulus | $E$ | Pa<br>[N $m^{-2}$] | • A measure of the relationship of stress and strain in the linear elasticity region of deformation along a single axis | • Intrinsic property<br>• Independent of EV geometry<br>• Extracted from force-distance curves using Hertz model, Thin Shell Model | 59,78 |
| Bending Modulus | $\kappa$ | J<br>[N·m] | • Tendency of an object to oppose bending<br>• Energy required to deform bilayer from its intrinsic curvature to a different curvature | • Intrinsic property<br>• Independent of EV geometry<br>• Extracted from force-distance curves using Thin Shell Model or Canham-Helfrich Theory<br>• For vesicles, often expressed in $k_BT$ | 65,78 |

Broadly, elasticity is the ability of a material to return to its original state after exposure to stress. An elastic structure will return to its original state, while a plastic structure will be permanently deformed. Elastic behavior has been observed in EVs and liposomes—this is an important characteristic, as the mechanical stability provided by elasticity will prevent irreversible changes due to forces encountered in a vesicle's lifespan.[40,47,48] In contrast, *mechanical stiffness, K,* describes the linear resistance of an elastic body such as an EV to deformation by an applied force $F$ for a displacement or indentation $\delta$, with units N $m^{-1}$, as shown in **Equation 1**:

$$K = \frac{F}{\delta} \tag{1}$$

Notably, the mechanical stiffness is not solely dependent on the inherent properties of an EV. Instead, both the size and geometry determine the stiffness of an EV. Furthermore, the elasticity of a material may be described by several moduli (expressed as Pa or N $m^{-2}$) such as the bulk modulus, shear modulus, and Young's Modulus ($E$). Of these moduli, Young's Modulus is the most relevant of the elastic moduli and describes the response of a material to a force applied along a single axis (such as compression via an AFM tip). Additionally, while not an elastic modulus, bending modulus or bending rigidity ($\kappa$) describes an EV's opposition to bending and is expressed in J (N·m). The bending modulus is the energy required to deform a membrane from its intrinsic curvature to a different curvature, and is often expressed in units of $k_BT$.

Given the complexity and heterogeneity of cell-secreted EVs, none of these discussed mechanical properties may adequately capture the complex mechanical behavior of EVs, an emerging concept is the inherent variations in mechanical properties of EVs.[49] Yet, assessing these mechanical properties at the single vesicle level, through a combination of stiffness, Young's Modulus, and bending modulus while considering variations in size and structure of EV sub-populations is advantageous, and promises novel, orthogonal, label-free insights into the EV subpopulations, and potential new avenues of physiological and clinical use of EVs.[38,39,50] With regards to techniques available for mechanical analysis of single cells, AFM, micropipette aspiration,[51] and several microfluidic approaches[52] have been widely adopted. While micropipette aspiration and deformability assessment techniques relying on optical imaging of shape fluctuations have been developed for micron-sized cells and large vesicles, these methods are less suitable for nanometer-sized vesicles such as EVs.[53,54] Electrodeformability techniques have been applied to measure the deformation of giant vesicles and now extend to smaller EVs using nanopores.[53]

## 4.4 Measurement of Mechanical Properties at the Nanoscale: Atomic Force Microscopy

### 4.4.1 EV imaging

The AFM, in particular, has become a favored method for imaging of soft biological nanoparticles such as EVs derived from cells[39,49,55] and various body fluids such as saliva,[13] blood plasma,[56] and serum,[57] enabling nanometer-level spatial resolution and piconewton force sensitivity.[58] Several AFM imaging modes have been applied to resolve the structure, mechanics, and biomolecular features of EVs.[2,59] Typically, first the isolated EVs are adhered to a relatively flat surface using physical adsorption, electrostatic interactions, chemical bonds, hydrophobic interactions, or other methods of adhesion. Imaging can be done under air[40] or fluidic buffer conditions[48] where the spherical shape of the EV is better preserved.[60] A molecularly sharp tip is raster-scanned over the EV-covered surface, and tip height is adjusted to contour surface features according to instrument feedback.[2,59] By recording tip height and tip deflection, topographical and mechanical information about the surface is obtained. Topographical information obtained from an AFM image allows the visualization of individual EV size and geometry.[13] AFM has been recommended by the International Society for Extracellular Vesicles (alongside EM) as a method for characterization of individual vesicles from a mixture (obtained from biofluid or cell supernatant) to indicate the heterogeneity of an EV sample based on these variations in size.[23]

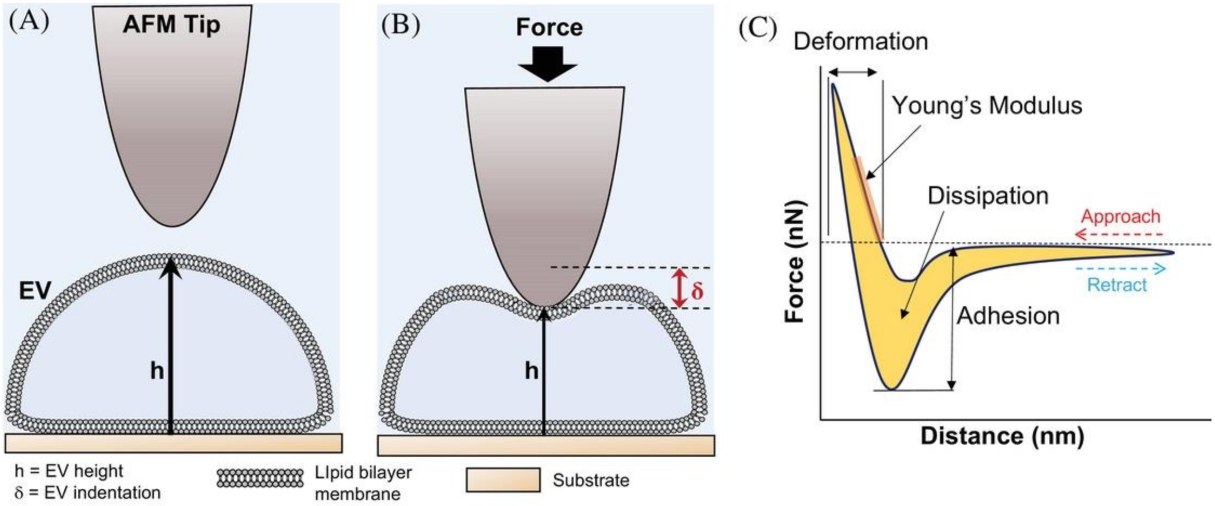

**Figure 2. An AFM tip indents an EV, and a force-distance curve is recorded.** a) In suspension, EVs are spherically shaped. When the EV adheres to a relatively flat substrate, it adopts a hemispherical shape, with height h, before it is indented by the AFM tip. b) The AFM tip indents the EV and deforms the lipid bilayer membrane. The indentation depth, δ, is calculated as the difference between the vesicle's original height and its new height. c) A force-distance curve is taken on the EV surface. Initially, the AFM tip is distant from the EV surface and there is no interaction between the AFM tip and the EV. The AFM tip approaches the EV, indents the surface to a preset maximum force, then retracts to its original position away from the EV. From a force-distance curve, quantities such as Young's Modulus (obtained by fitting an indentation model to the approach curve, highlighted with an orange bar), dissipation (the area between the approach and the retract curve, shaded in yellow), adhesion (the force between the baseline and the lowest point on the retract curve, marked with a double-headed arrow), and deformation (the depth of indentation into the sample from the approach curve, marked with a horizontal double-headed arrow) can be extracted. The direction of the approach is marked with a dashed red arrow, and the direction of the retract is marked with a dashed blue arrow. The approach features a baseline at zero force where the tip has not interacted with the sample yet, marked with a black dotted line.

### 4.4.2 EV mechanics

AFM provides unique mechanical information due to its physical contact with the sample. The mechanical information is primarily obtained either using AFM-based force spectroscopy or the PeakForce tapping mode (and other related modes such as Quantitative Imaging).[61,62] These modes extract a force-distance curve linked to a position on the EV surface, which plots the force exerted on the EV by the AFM tip as the tip indents the EV. A typical force-distance curve is comprised of an approach curve recorded as the tip indents the sample from a baseline of zero force, and a retract curve recorded as the tip pulls away from the sample and returns to its original position. Ideally, initially when the AFM tip is far from the sample surface, as the AFM tip approaches the surface the force between tip and surface is zero. But various environmental factors may cause thermal or mechanical drifts resulting in a non-zero force baseline. A non-zero force baseline is corrected by applying linear regression to the pre-contact region of the force-distance curve, and subtracting the linear regression from the curve to produce a horizontal force baseline at zero. **Figure 2** shows a schematic of an EV indented by an AFM tip during a force spectroscopy experiment and the resulting force-distance curve. From a force-distance curve, several mechanical parameters can be extracted. Young's Modulus is often obtained by fitting an indentation model (discussed in Section 4) to the approach curve. Adhesion is calculated by measuring the force between the baseline and the lowest point on the retract curve, and deformation is calculated as the depth of indentation into the sample on the approach curve. Dissipation, in units eV, is calculated from the area between the approach and retract curve. These mechanical parameters can be calculated for individual force-distance curves recorded over single localized EVs or mapped spatially across the surface of the EV.[39]

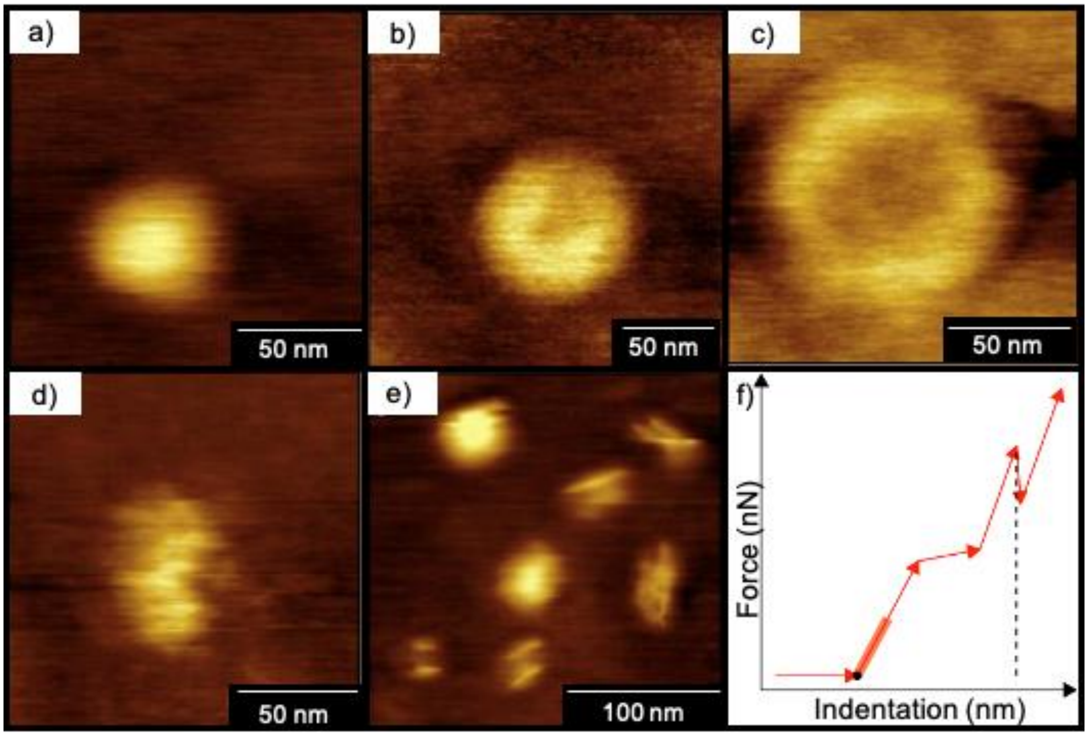

**Figure 3. Changes associated with an individual EV under increasing AFM imaging (or indentation) forces** a) Initially, the EV is characterized by round morphology (~50nm lateral dimension). b) An increase in imaging force results in an increase in the lateral dimension of the EV (~75 nm) and a force-induced central depression can be observed. c) Further increase in imaging force leads to a two-fold increase in particle lateral dimensions (~100nm), and the force-induced central depression occupies most of the EV surface area. Interestingly, until this point, the EV undergoes reversible elastic deformation, and reducing the applied imaging forces will cause the structure to return to the round morphology seen in (a). d) However, further increasing the applied force causes inelastic deformation of the EV and rupture of the lipid bilayer membrane of the EV and irreversible change in morphology as noted in an oblate morphology. e) Smaller, intact EV fragments can be seen following the vesicle rupture. These fragments likely correspond to intact EV substructures and membrane fragments. f) A representative force indentation curve showing EV response. As an AFM tip indents the EV (red arrows), changes in the indentation regime can be identified by a change in slope. Initially, after the point of contact, there is a linear relationship between force and indentation (relates to mechanical stiffness). At around 30-40% the radius of curvature of the EV, the response to indentation softens and the force-indentation curve flattens. Subsequently, the response to indentation stiffens due to increased contact area between tip and membrane. Eventually, the EV ruptures under enough force (labeled with a dotted line). *Reprinted (adapted) with permission from ACS Nano **2010**, 4 (4), 1921–1926. https://doi.org/10.1021/nn901824n. Copyright (2010) American Chemical Society.*

**Figure 3 (a-e)** shows an EV imaged by AFM, using varying force such that the EV is originally minimally perturbed, flattens as the force increases above 2 nN, but ruptures after 5 nN applied force—demonstrating the force sensitivity needed when using AFM to image soft biological samples such as EVs. EVs can be imaged and easily sized without disturbing their structure drastically, though proper deconvolution methods must be taken when calculating the true size of the EV due to deformation from the AFM tip while using Tapping Mode, even at low forces.[13,48,50,63–65] Besides the tip size and shape, the obtained EV image can be affected by regions of inhomogeneous elasticity within the EV, imaging forces, scan rate as well as the interaction between the planar substrate surface and the adhered EV.

A force-distance curve can be converted to a force-indentation curve as shown in **Figure 3f**. First, the tip is positioned above the EV surface, where the force acting in the tip is negligible. Subsequently, the tip approaches the EV surface at a defined velocity, makes initial contact with the EV surface, and then indents the EV. The contact point, labeled with a black dot, is defined as the point at which the tip makes initial contact with the EV surface resulting in change (increase) in the force vs indentation slope, indicating that the tip is applying force to the sample. As the AFM tip further indents the EV, different regimes such as the outer lipid bilayer membranes undergo deformation. Eventually further increase in the indentation force results in irreversible deformation and rupture of the EV as illustrated in **Figure 3f**, where the dotted line indicates the membrane rupture event on the force indentation curve. The force-indentation curves are used to derive quantitative biomechanical characteristics of single EVs particularly, the mechanical stiffness, Young’s Modulus, and bending modulus obtained using various indentation models, and indentation depth-dependent elasticity and plasticity.

**Table 2. Summary of the mechanical indentation models as applied to EVs and key findings.**

| Indentation Model | Summary | Benefits | Drawbacks | Reported Studies on Vesicles | | | | |
|---|---|---|---|---|---|---|---|---|
| | | | | Vesicle | $K$ [mN/m] | $E$ [MPa] | $\kappa$ [$k_BT$] | Reference |
| Hertz-contact | • EV assumed to be elastic, infinitely large, homogenous in composition<br>• No interactions between tip/sample | • Independent of EV size<br>• Simple | • Only valid for small indentations<br>• Assumed homogeneity not valid for EVs | Phosphatidylcholine | | 1.97 ± 0.75 | | 68 |
| | | | | Cholinergic Synaptic Vesicles | | 0.2-1.5 | | 71 |
| | | | | Saliva EV | | 0.89 ± 0.07 | | 69 |
| | | | | Exomere | | 145-816 | | 34 |
| | | | | Large EV | | 26-73 | | 34 |
| | | | | Small EV | | 70-420 | | 34 |
| Thin Shell | • Bilayer membrane treated as a single mechanical layer<br>• EV is assumed to be hollow | • Accounts for membrane's unique mechanical response | • Only valid for small indentations<br>• EVs do not have hollow interior<br>• Sensitive to assumed vesicle size and membrane thickness | Human malignant metastatic bladder cell-derived EVs | | 280 | | 55 |
| | | | | Human malignant non-metastatic bladder cell-derived EVs | | 95 | | 55 |
| | | | | Human non-malignant non-metastatic bladder cell-derived EVs | | 1527 | | 55 |
| | | | | Mouse hepatocyte EVs | 49 ± 12 | | | 49 |
| | | | | Rat hepatocyte EVs | 13 ± 9 | | | 49 |

| | | | | | | | | |
|---|---|---|---|---|---|---|---|---|
| Modified Canham-Helfrich | • Accounts for fluidity of bilayer membrane<br>• Assumes fluid-filled EV | • Valid for all indentation depths<br>• Accounts for pressurization due to adhesion to surface | • Labor-intensive<br>• Clean tether force needed on retract curve | Red blood cell-derived EV | Varied between patient samples | | 15±1 | 82 |
| | | | | Hereditary spherocytosis EV | 11 ± 2 | | 9±1 | 82 |

### 4.5 Indentation Models

Next, we will discuss the three predominant models of indentation that have been applied to date to determine the biomechanical properties of EVs by AFM, namely the Hertz model, the Thin Shell Model, and a model based on Canham-Helfrich Theory. The key findings describing the mechanical properties of EVs using these models are summarized in **Table 2** and described in detail below. Other models for vesicle indentation[66] or compression by parallel plates[67] have been used for micron-sized vesicles, but have not yet been applied to EV mechanical analysis.

#### 4.5.1 Hertz Model of Indentation

The Hertz model of indentation is the simplest and most commonly used model applied to AFM force indentation curves obtained on soft matter such as EVs. The model assumes EVs act as an infinitely large, isotopic, elastic mass with no interaction, adhesive or otherwise, between the tip and the sample. The original Hertz model was derived for a spherical tip: here, we discuss specifically the adaptation of the model for parabolic tips. Similar models are available for differently shaped tips (e.g. spherical, conical, cylindrical, pyramidal).[59] Irrespective of the shape of the indenter (the AFM probe), the Hertz model describes the dependence of force on indentation as in **Equation 2**, where $R_t$ is the tip radius, E is the Young's Modulus, *v* is Poisson's ratio (taken as 0.5 for EVs):

$$F(\delta) = \frac{4\sqrt{R_t}}{3}\frac{E}{1-v^2}\delta^{3/2} \tag{2}$$

Fitting of this equation to force-indentation curves obtained over single EVs allows for Young's Modulus to be extracted. The simplicity of this model is apparent. Little needs to be known about the sample itself; calculation of the intrinsic mechanical properties of an EV only depends on the tip radius and the (known) Poisson's ratio. Several previous studies have used the Hertz model to examine liposomes, exosomes, exomeres, and other EVs.[34,68–71] However, despite the simplicity of the Hertz model, its application to soft nanoparticles such as single EVs is complicated by tip-sample interactions and errors resulting from applying linear elastic representations beyond their validity range or at small indentation ranges prone to measurement uncertainties.[47,48,59,72] The Hertz model is only valid for small indentations past the point of contact such that the indentation depth is less than the radius of curvature of the probe, and that the indentation depth is less than 10% of the thickness of the sample.[59] Particularly for small EVs ( ~100 nm in diameter) such as exosomes, artificial stiffening due to the substrate may also affect calculated Young's Modulus—deeper indentations relative to the thickness of the sample show a larger Young's Modulus due to the tip sensing the hard substrate beneath.[73,74]

Several corrections have been proposed for the Hertz model that may prove beneficial for the study of EVs, as they accommodate for some of the drawbacks of the original model as they relate to EV composition and structure. One such example is the thin-film correction for the Hertz model has been developed, which accounts for AFM experiments in which the thickness of the layer is small compared to the contact radius of the indentation,[75] which our group has previously employed when calculating the Young's Modulus of EVs.[39] Recently, an adaptation of the Hertz model has been described for indentations where the indentation depth approaches the indenting tip size—this can allow for more accurate calculation of Young's Modulus of EVs, especially where small indentations record a response that is indiscernible from instrumental noise.[76] Also, the Derjagin-Muller-Toropov (DMT) model, may be appropriate when addressing adhesion between the EV surface and the AFM tip.[77] Still, these adaptations do not account for complex inherent inhomogeneity of an EV—such as the presence of the fluid bilayer membrane and internal cargo that are likely to deform differently under similar indentation forces. Other models that account for the inhomogeneity of EVs may, therefore, be necessary for accurate mechanical analysis.

### 4.5.2 Thin Shell Theory of Indentation

The Thin Shell Theory (TST) of indentation assumes that an EV acts as a hollow shell with a thin wall of thickness $t$, with no interior cargo, and has a nonzero shear modulus.[78] The dependence of force on indentation is described by **Equation 3**, where E is the Young's Modulus as before, $\alpha$ is a geometry-dependent proportionality factor, and $R_C$ is the radius of curvature of the vesicle.

$$F(\delta) = \frac{\alpha E t^2}{R_C}\delta \tag{3}$$

The calculation of the Young's Modulus *E* (and therefore the calculation of the bending modulus) relies on several assumptions about the vesicle's geometry and thickness of the limiting bilayer membrane. EVs are assumed to have a membrane thickness of ~5 nm. However, an increase in shell thickness to ~6 nm leads to a roughly 30% decrease in E due to the inverse square dependence of E on thickness.[48] Further, as the shell thickness increases, the predicted linearity at small indentation disappears, and instead superlinear behavior predicted by the Hertz model dominates. This model predicts a linear relationship between force and indentation for indentations less than the shell thickness—for EVs, this amounts to indentation depths roughly in the range of ~5 nm beyond the point of contact between the probe and the EV surface. Beyond these indentation depths, the model predicts a buckling effect, where the curvature of the top of the vesicle becomes inverted and the response to indentation softens due to shear.[47] However, this predicted early buckling is not always observed experimentally. While expected to begin at an indentation depth of 5 nm, buckling in similarly-sized nanovesicles has been observed at larger indentation depths, around the 15-20 nm range.[48,49] Primarily, the failure of the TST-based models to accurately predict observed experimental mechanical behavior past small indentations warrants further analysis of EV mechanical characteristics, particularly for larger indentations.

### 4.5.3 Nanoindentation based on Canham-Helfrich Theory

A recently developed model based on the Canham-Helfrich Theory (CHT), describes the elastic properties of a vesicle due to its fluid membrane.[79,80] Here, the bilayer membrane is assumed to be completely fluid, and the inner and outer layers simply slide past each other when indented—the shear modulus is zero. In this model, the shape of the vesicle is solved such that the free energy of bending is minimized, as in **Equation 4**. This will be based on a vesicle's bending modulus $\kappa$, mean curvature H, intrinsic curvature $C_0$, and surface tension $\sigma$.

$$FreeEnergy_{Helfrich} = \int \left(\frac{\kappa}{2}(2H - C_0)^2 + \sigma\right) dA \qquad (4)$$

Importantly, the intrinsic curvature is taken to be 0 for systems where the inner and outer membranes are symmetric—such as in liposomes, a common model system for cells and EVs, although in the case for EVs, the presence of membrane proteins and receptors is likely to result in asymmetric lipid bilayer limiting membranes.

Vorselen et al. developed a model for EV nanoindentations based on CHT, calculating the shape of the vesicle at various indentation depths and the vesicle's internal pressure.[65] The model predicts three regimes of vesicle deformation for a tip with a radius of about 10% of the radius of the curvature of the vesicle. First, a slightly superlinear response as the vesicle apex flattens, followed by a second regime characterized by a softened response at about an indentation depth 35-40% of the vesicle's radius of curvature due to the formation of an inward tether (a tubular segment of the membrane). The final region of tip-dominated stiffening occurs at an indentation depth of 80% of the vesicle's radius of curvature. This model is notably sensitive to both tip size and vesicle size.

Here, the model accounts for the contribution of pressure resulting from surface adhesion of EVs to the measured vesicle stiffness. A surface-bound vesicle will deform based on its affinity for the surface, and this deformation will cause a decrease in internal volume due to the inability of the lipid bilayer membrane to stretch more than a few percent.[65] This decrease in volume leads to an increase in concentration for the internal components of the EV, which causes an osmotic pressure difference between the interior cargo of the vesicle and the liquid in which it is imaged. This osmotic pressure difference is the major component of the observed vesicle stiffness, on the order of $10^{-2}$ N $m^{-1}$, while the bending modulus only contributes $10^{-5}$ N $m^{-1}$. An estimation of this osmotic pressure difference, required to determine the bending modulus, is accomplished using an outward tether force obtained from the retraction curve following small indentations.[65,81] Although liposomes may readily show a single, well-defined detachment event, EVs do not always show a well-defined tether force, and instead show multiple complex detachment events,[82,83] likely due to additional proteins or surface receptors adhering to the tip. Failure to obtain this single, well-defined detachment event tether force prevents the calculation of the bending modulus and limits the use of this model for investigating EV mechanical properties.

Overall, across the three main models employed to the understanding of EV indentation analysis, several aspects need to be carefully addressed for the determination of the EV mechanical properties. Amongst these, the accurate calculation of EV size, in particular, is especially relevant to the TST and CHT-based models, where the uncertainties in vesicle size determination. Care must be taken when calculating EV size from AFM images. Soft biological samples such as EVs are prone to deformation due to the force applied during imaging. This factor is exceptionally relevant when using tapping mode and other related modes, as images obtained by these modes can underestimate the true height of an EV. Where precise knowledge of individual EV size is relevant to downstream calculations, several studies have instead used the height obtained from force spectroscopy and provided various corrections due to different geometry and tip deconvolution.[48,65] Several studies have successfully employed the elastic properties of EVs from AFM force-indentation experiments for biomarkers and other applications, including changes associated with various pathological conditions such as cancer,[39,49,55] and in malaria-infected

RBCs.[84–86] Given the diversity of EVs and various sub-populations, as the potential for use of the biomechanical features to characterize various EV sub-populations becomes more widespread, it is increasingly important to suitably address the main confounders for more robust and reproducible measurements.

### 4.6 Towards High-Throughput Mechanical Analysis of EVs

Given the small size of the EVs, substrate effects further complicate the measurement of the mechanical properties of EVs. As discussed above, indentation past about 10% of the sample thickness into a nanoparticle can produce an artificially large Young's Modulus due to the stiff substrate beneath.[73,74] Furthermore, the choice of imaging substrates has also been shown to affect EV deformation on the surface, as demonstrated in **Figure 4**. EVs carry a negative surface charge and will deform more on positively-charged surfaces such as poly-L-lysine, and deform less on negatively-charged surfaces such as unmodified mica.[87] This feature complicates the collection of force-distance curves during imaging—highly deformed vesicles may be so soft that determining the initial point of contact between the EV surface and the AFM tip becomes challenging. High vesicle deformability is linked to increased spreading on the surface, to the point of partial or complete rupture and leaking of interior cargo.[87] Thus, fine-tuning a surface for AFM imaging appears to be a necessity in some cases, such that a strong affinity for a surface can cause an already soft vesicle to undergo irreversible deformation, while a stiff vesicle with a weak affinity for a surface may not adequately adhere to withstand the imaging forces. A population of stiffer EVs near the end of this limit for a surface may skew towards softer subpopulations because stiffer EVs simply do not adhere to the surface. Deformation of EVs can also cause them to adopt varying geometries (hemispherical, spherical cap, ellipsoidal) that further challenges the precise determination of EV size. The prerequisite to precisely size individual EVs for accurate mechanical analysis constrains the high-throughput mechanical analysis of EVs.

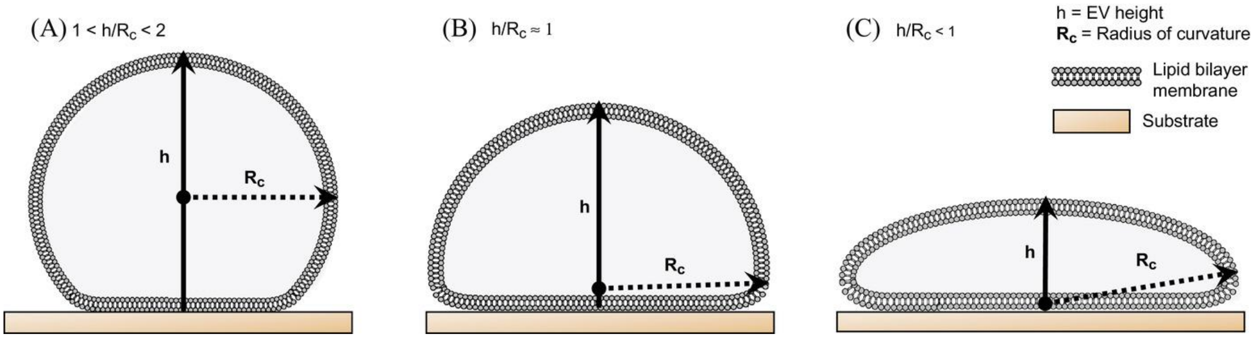

**Figure 4. EVs deform differently based on their affinity for the substrate, and this deformation can be measured by the ratio of the EV height, h, to the radius of curvature, Rc**. a) For a weakly surface-bound EV, structural deformation is low, causing it to adopt a spherical cap shape. The $h/R_C$ ratio approaches 2, the maximum value. b) In the case of an EV moderately adhered to the substrate, the structural deformation is moderate, causing it to adopt a nearly hemispherical shape. The $h/R_C$ is around 1. c) For an EV strongly adhered to the substrate, EV structural deformation is high, causing it to adopt a flattened and oblate shape. The $h/R_C$ ratio is much less than 1.

In addition to biomechanical analysis, AFM methods that allow simultaneous imaging and mechanical mapping have previously demonstrated spatial insights into the mechanical properties of EVs. Our group has previously used AFM to map adhesion and Young's Modulus over the surface of glioblastoma-derived EVs.[39] Phase imaging, in which the difference between the phase of the oscillating cantilever and the excitation signal is recorded, has been used to examine changes in EV structure under different applied forces, and to visually demonstrate compositional differences in bacteria membrane-originated EVs based on adhesion, elasticity, and friction arising from biochemical variations in the EV membrane.[40,88] While force spectroscopy on single EVs is an attractive option to understand their mechanical properties in-depth, it is a time-consuming and low-throughput approach. A small sample size may also fail to capture the complexity introduced by the heterogeneity of EVs[23] further warranting alternative higher-throughput methods to quantitatively evaluate EV structural and mechanical characteristics. Some efforts in this direction encompass exploiting the differential height versus diameter profiles of EVs on various surfaces, for example, by estimating the mechanical stiffness of individual EVs based on their deformation on the surface, using the vesicle-surface contact angle.[83] While two

EVs may have the same diameter in solution, their stiffness and affinity for the surface affect deformation on the surface. A linear calibration curve relating mechanical stiffness to vesicle-surface contact angle was constructed from a series of liposomes and used to extrapolate the mechanical stiffness of EVs from two sources based solely on the measured vesicle-surface contact angle. The calibration curve-obtained EV mechanical stiffness data matched well to EV mechanical stiffness obtained directly from force-spectroscopy and demonstrates a high-throughput method of determining stiffness without the need to obtain force-distance curves for individual EVs.

Similarly, Yokota et al. used nanopatterned chips and used AFM to probe immobilized EVs.[89] EVs individually immobilized on polyethylene-glycol nanospots, and strong hydrophobic interactions caused single EVs to adopt an oblate, ellipsoidal shape. The extent of this deformation, calculated as the ratio of height to diameter on the surface, was attributed both to their affinity for the nanospot and to their intrinsic mechanical properties and showed statistically significant differences in deformation between cancerous and noncancerous EVs. In the future, optimization of patterned EVs allowing for selective adhesion of EV subpopulations of interest may be combined with techniques already used with nanoarray methods such as surface-enhanced Raman spectroscopy, enzyme-linked immunosorbent assay, matrix-assisted laser desorption time of flight mass spectroscopy (MALDI-TOF). The potential to assess the biochemical properties of EV subpopulations complementing single vesicle characterization by AFM seems promising.

Notably, such methods capture EV mechanical properties, without the need for obtaining individual force-indentation curves for single EVs. As mentioned previously, force spectroscopy on individual EVs followed by the fitting of an indentation model, while informative, is time-consuming and complicated by the necessity to sort force-distance curves to find usable or characteristic curves for each vesicle.[82,83] Calculation of EV deformation using features identified by standard topographical three-dimensional surface mapping of EVs provides a higher-throughput alternative to stringent mechanical analysis. Thus far, it is obvious that EV deformation on a substrate is influenced by multiple factors such as surface binding affinity, intrinsic mechanical properties such as bending modulus or Young's Modulus, as well as the size of the vesicle in solution. While the links between these properties, and the extent to which they influence deformation, are currently under investigation, it is evident that automated, robust, and high-throughput analysis of structural-mechanical analysis of EVs, both for force-indentation or surface topography-based evaluation of EV mechanics.

### 4.7 AFM and Machine Learning Methods

The past decade has seen remarkable advances in machine learning methods[90,91] employed for automated, high-throughput imaging, and analysis. Whereas typical AFM analysis of EVs frequently reported variables such as size, height, phase, stiffness, Young's Modulus, or bending modulus, machine learning methods facilitate additional features of the force-indentation curve at different indentation depths, mean or median height value, boundary length, and surface area. Even more important is the potential to discover correlations between these variables, not achievable through human-driven analysis alone. Machine learning methods have demonstrated the capability to utilize the multifaceted AFM-based structural and mechanical analysis,[92] and could be a powerful tool in the study of EV structure and function. On a related note, Ito et al. used a combination of supervised and unsupervised learning to predict the parent cell of EVs using EV mechanical deformation based on morphological features.[87] Multiple EV morphology features were extracted, and subjected to dimensionality reduction. Using support vector machine learning the study achieved high accuracy for EV parent cell prediction, using EV volume and deformation as predictive features. Here, the substrate affected the accuracy of prediction, as the choice of substrate affected the smallest incremental change in the aspect ratio that could be detected and used to discriminate between EV types—a phenomenon necessitating further study.

Another study applied deep learning methods to successfully identify cancer and non-cancer regions in brain tissue samples based on force-indentation curves.[93] In contrast to traditional AFM-based mechanical analysis of tissues which fit a segment of the approach curve to obtain Young's Modulus, the neural networks used the full indentation depth of the approach curve and the retract curve of the force-indentation profiles to classify the tissue surface. In general, the calculation of Young's modulus by fitting the Hertz or TST models of indentation only uses a fraction of the force-distance approach curve, and these models require operator-driven baseline correction, optimization of contact point determination, and model fitting. Neural networks circumvent these operator-driven steps and utilize mechanical information contained in other parts of the approach curve or the retract curve—not currently represented by the discussed indentation models—to classify the surface. Further, the binary output of the neural networks (cancer or non-cancer) does not require operator-driven classification based on Young's Modulus, a benefit for future implementation in diagnostic settings.

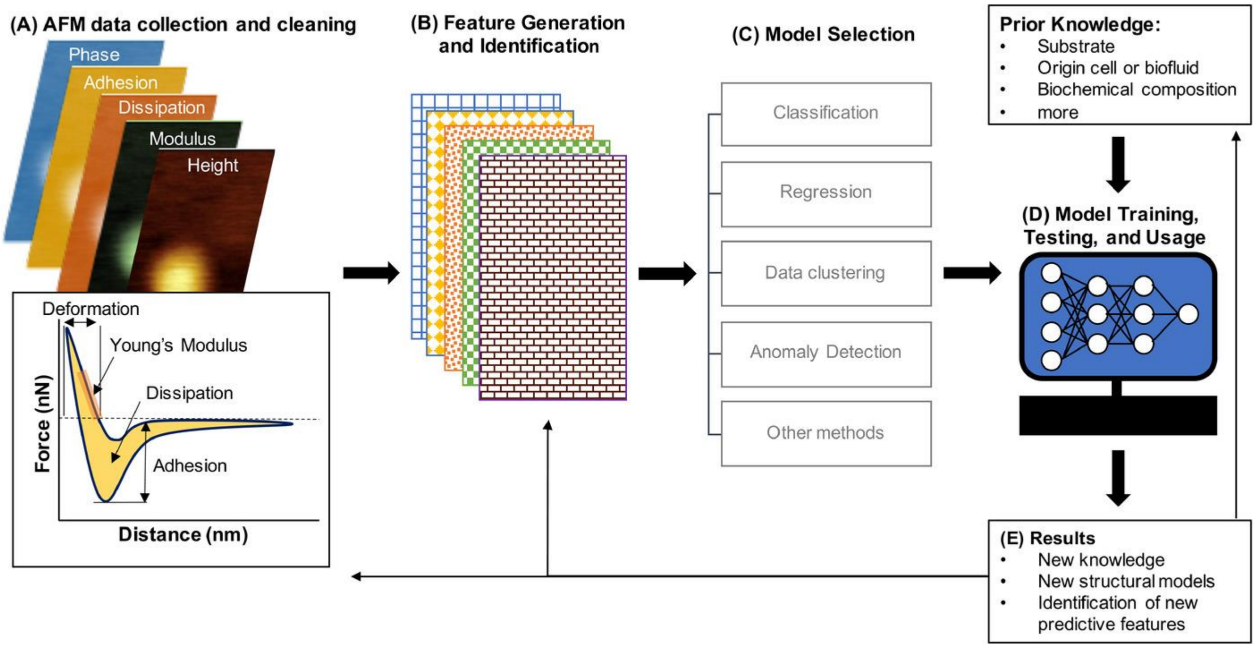

**Figure 5. A flowchart describing the incorporation of machine learning methods to an AFM structure-mechanics workflow.** (a) Single EVs are imaged in an automated AFM experiment to generate multidimensional data quantifying features such as from channels such as but not limited

to height, dissipation, adhesion, phase, and force-distance curves for each pixel; which is cleaned using image-processing software. Inset shows a typical force-distance curve, from which mechanical properties such as Young's Modulus, dissipation, adhesion, and deformation can be extracted. (b) This data is mined to identify features by human-driven methods or deep learning-driven methods, and (c) a machine learning model based on desired output such as classification, regression, data clustering, anomaly detection, or more. (d) The chosen machine learning model is trained, tested, and applied, in conjunction with prior knowledge. (e) This analysis leads to new knowledge of EVs, new or improved models, or the identification of new predictive structural or mechanical features that are used to inform future data collection and analysis.

Therefore, it is interesting to speculate the implications of machine learning methods to robust, high-throughput assessment of EV structural-mechanical properties. We believe that there is conceivable merit in combining the multidimensional data provided by AFM with the demonstrated power of machine learning to dissect large amounts of data. One of the key advantages of machine learning workflows, as outlined in **Figure 5**, is the ability to identify correlation in large datasets, which is used to improve further studies.[94] We postulate that the main steps in a generalized AFM imaging and analysis workflow for EVs incorporating machine learning methods may include a) AFM structure-mechanics data collection and cleaning via image-processing software, b) feature generation and selection, either human-driven via image-processing software or AI-driven via deep learning methods, c) model selection based on the research question or desired output, d) model training, testing, and usage, and e) use of knowledge obtained from models to further refine models or inform new experiments and data collection.

Such workflows are increasingly feasible to implement due to the streamlining, ease of use, and development of open-source machine learning materials and software. The development of plugins like DeepImageJ bridge the gap between traditional image-processing software and machine learning methods.[95] Open-source machine learning packages are available in multiple coding languages, including R language,[96] MATLAB,[97] and Python.[98] Within the field of EVs, open data initiatives such as EV-Track[99] provide a plethora of datasets that could be reassessed using machine learning methods to identify new features and structure in data not previously delineated in the human-driven analysis. The adoption of machine learning methods by the EV community will be accompanied by new challenges and biases—both numerical and researcher-introduced—inherent to machine learning methods.[94] Fortunately, the drive towards "smart data" will inevitably help those seeking to implement machine learning analysis into EV studies to collaborate and obtain feedback from the broader community, and help to minimize biases and at the same time educate users on the best practices in machine learning.[100]

### 4.8 Conclusions

Improved biomechanical understanding of single EVs provides an opportunity to address the missing links between physical properties and biological function of heterogeneous EVs. AFM has proven itself to be a powerful nanoscale tool to characterize the unique structural and mechanical properties of single EVs, the latter of which can be extracted using various indentation models. While no single model emerges as a definitive frontrunner, these models highlight the inherent biomechanical heterogeneity of membranous EVs and non-membranous exomeres, beyond variations in particle size and morphology. Such ability to quantitatively profile label-free biomechanical properties of circulating EVs in bio-fluids such as blood, urine and saliva may have significant implications for orthogonal disease biomarker development. Further, a comprehensive characterization of EV mechanical properties and the establishment of assays to tune or modify EV mechanical properties could improve drug delivery applications, in parallel to efforts that focus on optimizing the biochemical properties of EVs for targeted delivery. It is also imminent that incorporating machine learning methods into AFM-driven studies of EVs are on the horizon to create powerful information feedback loops that identify patterns and features in EV structure not evident in human-driven analysis, and inform future experiments. In summary, the single EV structure-mechanical analysis is an emerging concept augmented by significant advances in technology and computing capabilities. Label-free, orthogonal biomechanical and biophysical understanding of EVs beyond biomolecular or particle size analysis promises significant implications for EV research and clinical use.

## 4.9 References

1. Kalluri, R. & LeBleu, V. S. The biology, function, and biomedical applications of exosomes. *Science* **367**, (2020).
2. Sharma, S., LeClaire, M. & Gimzewski, J. K. Ascent of atomic force microscopy as a nanoanalytical tool for exosomes and other extracellular vesicles. *Nanotechnology* **29**, 132001 (2018).
3. Murphy, D. E. *et al.* Extracellular vesicle-based therapeutics: natural versus engineered targeting and trafficking. *Experimental & Molecular Medicine* **51**, 1–12 (2019).
4. Peinado, H. *et al.* Melanoma exosomes educate bone marrow progenitor cells toward a pro-metastatic phenotype through MET. *Nat Med* **18**, 883–891 (2012).
5. Kahlert, C. & Kalluri, R. Exosomes in Tumor Microenvironment Influence Cancer Progression and Metastasis. *J Mol Med (Berl)* **91**, 431–437 (2013).
6. Becker, A. *et al.* Extracellular vesicles in cancer: cell-to-cell mediators of metastasis. *Cancer Cell* **30**, 836–848 (2016).
7. von Schwedler, U. K. *et al.* The Protein Network of HIV Budding. *Cell* **114**, 701–713 (2003).
8. Gould, S. J., Booth, A. M. & Hildreth, J. E. K. The Trojan exosome hypothesis. *PNAS* **100**, 10592–10597 (2003).
9. Rajendran, L. *et al.* Alzheimer’s disease β-amyloid peptides are released in association with exosomes. *PNAS* **103**, 11172–11177 (2006).
10. Pisitkun, T., Shen, R.-F. & Knepper, M. A. Identification and proteomic profiling of exosomes in human urine. *PNAS* **101**, 13368–13373 (2004).
11. Skog, J. *et al.* Glioblastoma microvesicles transport RNA and protein that promote tumor growth and provide diagnostic biomarkers. *Nat Cell Biol* **10**, 1470–1476 (2008).

12. Ogawa, Y., Kanai-Azuma, M., Akimoto, Y., Kawakami, H. & Yanoshita, R. Exosome-Like Vesicles with Dipeptidyl Peptidase IV in Human Saliva. *Biological and Pharmaceutical Bulletin* **31**, 1059–1062 (2008).
13. Sharma, S., Gillespie, B. M., Palanisamy, V. & Gimzewski, J. K. Quantitative Nano-structural and Single Molecule Force Spectroscopy bio-molecular analysis of human saliva derived exosomes. *Langmuir* **27**, 14394–14400 (2011).
14. Akers, J. C. *et al.* miRNA contents of cerebrospinal fluid extracellular vesicles in glioblastoma patients. *J Neurooncol* **123**, 205–216 (2015).
15. Beretti, F. *et al.* Amniotic fluid stem cell exosomes: Therapeutic perspective. *BioFactors* **44**, 158–167 (2018).
16. Zhuang, X. *et al.* Treatment of Brain Inflammatory Diseases by Delivering Exosome Encapsulated Anti-inflammatory Drugs From the Nasal Region to the Brain. *Mol Ther* **19**, 1769–1779 (2011).
17. Lai, R. C., Chen, T. S. & Lim, S. K. Mesenchymal stem cell exosome: a novel stem cell-based therapy for cardiovascular disease. *Regenerative Medicine* **6**, 481–492 (2011).
18. O'Driscoll, L. Extracellular vesicles from mesenchymal stem cells as a Covid-19 treatment. *Drug Discovery Today* **25**, 1124–1125 (2020).
19. Tsuchiya, A. *et al.* Therapeutic potential of mesenchymal stem cells and their exosomes in severe novel coronavirus disease 2019 (COVID-19) cases. *Inflammation and Regeneration* **40**, 14 (2020).
20. Abraham, A. & Krasnodembskaya, A. Mesenchymal stem cell-derived extracellular vesicles for the treatment of acute respiratory distress syndrome. *Stem Cells Transl Med* **9**, 28–38 (2019).
21. Zabeo, D. *et al.* Exosomes purified from a single cell type have diverse morphology. *J Extracell Vesicles* **6**, (2017).

22. Xu, R., Greening, D. W., Zhu, H.-J., Takahashi, N. & Simpson, R. J. Extracellular vesicle isolation and characterization: toward clinical application. *J Clin Invest* **126**, 1152–1162 (2016).
23. Théry, C. *et al.* Minimal information for studies of extracellular vesicles 2018 (MISEV2018): a position statement of the International Society for Extracellular Vesicles and update of the MISEV2014 guidelines. *Journal of Extracellular Vesicles* **7**, 1535750 (2018).
24. Piper, R. C. & Katzmann, D. J. Biogenesis and Function of Multivesicular Bodies. *Annu Rev Cell Dev Biol* **23**, 519–547 (2007).
25. Hanson, P. I. & Cashikar, A. Multivesicular Body Morphogenesis. *Annual Review of Cell and Developmental Biology* **28**, 337–362 (2012).
26. Sedgwick, A. E. & D'Souza-Schorey, C. The biology of extracellular microvesicles. *Traffic* **19**, 319–327 (2018).
27. Caruso, S. & Poon, I. K. H. Apoptotic Cell-Derived Extracellular Vesicles: More Than Just Debris. *Front Immunol* **9**, (2018).
28. Ma, L. *et al.* Discovery of the migrasome, an organelle mediating release of cytoplasmic contents during cell migration. *Cell Res* **25**, 24–38 (2015).
29. Tavano, S. & Heisenberg, C.-P. Migrasomes take center stage. *Nature Cell Biology* **21**, 918–920 (2019).
30. Melentijevic, I. *et al.* C. elegans neurons jettison protein aggregates and mitochondria under neurotoxic stress. *Nature* **542**, 367–371 (2017).
31. Di Vizio, D. *et al.* Large Oncosomes in Human Prostate Cancer Tissues and in the Circulation of Mice with Metastatic Disease. *Am J Pathol* **181**, 1573–1584 (2012).
32. Minciacchi, V. R. *et al.* Large oncosomes contain distinct protein cargo and represent a separate functional class of tumor-derived extracellular vesicles. *Oncotarget* **6**, 11327–11341 (2015).

33. Minciacchi, V. R., Freeman, M. R. & Di Vizio, D. Extracellular Vesicles in Cancer: Exosomes, Microvesicles and the Emerging Role of Large Oncosomes. *Semin Cell Dev Biol* **40**, 41–51 (2015).
34. Zhang, H. *et al.* Identification of distinct nanoparticles and subsets of extracellular vesicles by asymmetric-flow field-flow fractionation. *Nat Cell Biol* **20**, 332–343 (2018).
35. Zaborowski, M. P., Balaj, L., Breakefield, X. O. & Lai, C. P. Extracellular Vesicles: Composition, Biological Relevance, and Methods of Study. *Bioscience* **65**, 783–797 (2015).
36. Hartjes, T. A., Mytnyk, S., Jenster, G. W., van Steijn, V. & van Royen, M. E. Extracellular Vesicle Quantification and Characterization: Common Methods and Emerging Approaches. *Bioengineering* **6**, 7 (2019).
37. Khatun, Z., Bhat, A., Sharma, S. & Sharma, A. Elucidating diversity of exosomes: biophysical and molecular characterization methods. *Nanomedicine* **11**, 2359–2377 (2016).
38. Sharma, S., LeClaire, M., Wohlschlegel, J. & Gimzewski, J. Impact of isolation methods on the biophysical heterogeneity of single extracellular vesicles. *Scientific Reports* **10**, 13327 (2020).
39. Sharma, S., Das, K., Woo, J. & Gimzewski, J. K. Nanofilaments on glioblastoma exosomes revealed by peak force microscopy. *J R Soc Interface* **11**, (2014).
40. Sharma, S. *et al.* Structural- mechanical characterization of nanoparticles- Exosomes in human saliva, using correlative AFM, FESEM and force spectroscopy. *ACS Nano* **4**, 1921–1926 (2010).
41. Anselmo, A. C. *et al.* Elasticity of Nanoparticles Influences Their Blood Circulation, Phagocytosis, Endocytosis, and Targeting. *ACS Nano* **9**, 3169–3177 (2015).
42. Anselmo, A. C. & Mitragotri, S. Impact of particle elasticity on particle-based drug delivery systems. *Advanced Drug Delivery Reviews* **108**, 51–67 (2017).
43. Franzen, C. A. *et al.* Characterization of Uptake and Internalization of Exosomes by Bladder Cancer Cells. *Biomed Res Int* **2014**, (2014).

44. French, K. C., Antonyak, M. A. & Cerione, R. A. Extracellular Vesicle Docking at the Cellular Port: Extracellular Vesicle Binding and Uptake. *Semin Cell Dev Biol* **67**, 48–55 (2017).

45. Tian, T. *et al.* Dynamics of exosome internalization and trafficking. *Journal of Cellular Physiology* **228**, 1487–1495 (2013).

46. Kowal, J., Tkach, M. & Théry, C. Biogenesis and secretion of exosomes. *Current Opinion in Cell Biology* **29**, 116–125 (2014).

47. Li, S., Eghiaian, F., Sieben, C., Herrmann, A. & Schaap, I. A. T. Bending and Puncturing the Influenza Lipid Envelope. *Biophys J* **100**, 637–645 (2011).

48. Calò, A. *et al.* Force measurements on natural membrane nanovesicles reveal a composition-independent, high Young's modulus. *Nanoscale* **6**, 2275–2285 (2014).

49. Royo, F. *et al.* Differences in the metabolite composition and mechanical properties of extracellular vesicles secreted by hepatic cellular models. *J Extracell Vesicles* **8**, (2019).

50. Woo, J., Sharma, S. & Gimzewski, J. The Role of Isolation Methods on a Nanoscale Surface Structure and its Effect on the Size of Exosomes. *Journal of Circulating Biomarkers* **5**, 11 (2016).

51. González-Bermúdez, B., Guinea, G. V. & Plaza, G. R. Advances in Micropipette Aspiration: Applications in Cell Biomechanics, Models, and Extended Studies. *Biophysical Journal* **116**, 587–594 (2019).

52. Stoecklein, D. & Di Carlo, D. Nonlinear Microfluidics. *Anal. Chem.* **91**, 296–314 (2019).

53. Morshed, A., Karawdeniya, B. I., Bandara, Y. M. N. D. Y., Kim, M. J. & Dutta, P. Mechanical characterization of vesicles and cells: A review. *ELECTROPHORESIS* **41**, 449–470 (2020).

54. Piontek, M. C., Lira, R. B. & Roos, W. H. Active probing of the mechanical properties of biological and synthetic vesicles. *Biochimica et Biophysica Acta (BBA) - General Subjects* 129486 (2019) doi:10.1016/j.bbagen.2019.129486.

55. Whitehead, B. *et al.* Tumour exosomes display differential mechanical and complement activation properties dependent on malignant state: implications in endothelial leakiness. *J Extracell Vesicles* **4**, (2015).
56. Yuana, Y. *et al.* Atomic force microscopy: a novel approach to the detection of nanosized blood microparticles. *Journal of Thrombosis and Haemostasis* **8**, 315–323 (2010).
57. Paolini, L. *et al.* Residual matrix from different separation techniques impacts exosome biological activity. *Scientific Reports* **6**, 23550 (2016).
58. Binnig, G., Quate, C. F. & Gerber, Ch. Atomic Force Microscope. *Phys. Rev. Lett.* **56**, 930–933 (1986).
59. Krieg, M. *et al.* Atomic force microscopy-based mechanobiology. *Nature Reviews Physics* **1**, 41–57 (2019).
60. Parisse, P. *et al.* Atomic force microscopy analysis of extracellular vesicles. *Eur Biophys J* **46**, 813–820 (2017).
61. Dufrêne, Y. F. *et al.* Imaging modes of atomic force microscopy for application in molecular and cell biology. *Nature Nanotechnology* **12**, 295–307 (2017).
62. Shi, J., Hu, Y., Hu, S., Ma, J. & Su, C. Method and apparatus of using peak force tapping mode to measure physical properties of a sample. (2014).
63. Thomson, N. H. Imaging the substructure of antibodies with tapping-mode AFM in air: the importance of a water layer on mica. *Journal of Microscopy* **217**, 193–199 (2005).
64. Dokukin, M. E., Guz, N. V., Gaikwad, R. M., Woodworth, C. D. & Sokolov, I. Cell Surface as a Fractal: Normal and Cancerous Cervical Cells Demonstrate Different Fractal Behavior of Surface Adhesion Maps at the Nanoscale. *Phys. Rev. Lett.* **107**, 028101 (2011).
65. Vorselen, D., MacKintosh, F. C., Roos, W. H. & Wuite, G. J. L. Competition between Bending and Internal Pressure Governs the Mechanics of Fluid Nanovesicles. *ACS Nano* **11**, 2628–2636 (2017).

66. Schäfer, E., Vache, M., Kliesch, T.-T. & Janshoff, A. Mechanical response of adherent giant liposomes to indentation with a conical AFM-tip. *Soft Matter* **11**, 4487–4495 (2015).
67. Schäfer, E., Kliesch, T.-T. & Janshoff, A. Mechanical Properties of Giant Liposomes Compressed between Two Parallel Plates: Impact of Artificial Actin Shells. *Langmuir* **29**, 10463–10474 (2013).
68. Liang, X., Mao, G. & Simon Ng, K. Y. Probing small unilamellar EggPC vesicles on mica surface by atomic force microscopy. *Colloids and Surfaces B: Biointerfaces* **34**, 41–51 (2004).
69. Sharma, S., Palanisamy, V., Mathisen, C., Schmidt, M. & Gimzewski, J. K. Exosomes-biological liposomes as potential drug delivery agents. *Global Journal of Physical Chemistry* **2**, 4 (2011).
70. Jin, A. J., Prasad, K., Smith, P. D., Lafer, E. M. & Nossal, R. Measuring the Elasticity of Clathrin-Coated Vesicles via Atomic Force Microscopy. *Biophys J* **90**, 3333–3344 (2006).
71. Laney, D. E., Garcia, R. A., Parsons, S. M. & Hansma, H. G. Changes in the Elastic Properties of Cholinergic Synaptic Vesicles as Measured by Atomic Force Microscopy. *Biophys J* **72**, 806–813 (1997).
72. Costa, K. D. & Yin, F. C. P. Analysis of Indentation: Implications for Measuring Mechanical Properties With Atomic Force Microscopy. *J Biomech Eng* **121**, 462–471 (1999).
73. Domke, J. & Radmacher, M. Measuring the Elastic Properties of Thin Polymer Films with the Atomic Force Microscope. *Langmuir* **14**, 3320–3325 (1998).
74. Dimitriadis, E. K., Horkay, F., Maresca, J., Kachar, B. & Chadwick, R. S. Determination of elastic moduli of thin layers of soft material using the atomic force microscope. *Biophys J* **82**, 2798–2810 (2002).
75. Chadwick, R. S. Axisymmetric Indentation of a Thin Incompressible Elastic Layer. *SIAM J. Appl. Math.* **62**, 1520–1530 (2002).

76. Guo, Z. *et al.* A modified Hertz model for finite spherical indentation inspired by numerical simulations. *European Journal of Mechanics - A/Solids* **83**, 104042 (2020).
77. Derjaguin, B. V., Muller, V. M. & Toporov, Yu. P. Effect of contact deformations on the adhesion of particles. *Journal of Colloid and Interface Science* **53**, 314–326 (1975).
78. Roos, W. H., Bruinsma, R. & Wuite, G. J. L. Physical virology. *Nature Physics* **6**, 733–743 (2010).
79. Canham, P. B. The minimum energy of bending as a possible explanation of the biconcave shape of the human red blood cell. *Journal of Theoretical Biology* **26**, 61–81 (1970).
80. Helfrich, W. Elastic Properties of Lipid Bilayers: Theory and Possible Experiments. *Zeitschrift für Naturforschung C* **28**, 693–703 (1973).
81. Cuvelier, D., Derényi, I., Bassereau, P. & Nassoy, P. Coalescence of Membrane Tethers: Experiments, Theory, and Applications. *Biophys J* **88**, 2714–2726 (2005).
82. Vorselen, D. *et al.* The fluid membrane determines mechanics of erythrocyte extracellular vesicles and is softened in hereditary spherocytosis. *Nature Communications* **9**, 4960 (2018).
83. Ridolfi, A. *et al.* AFM-Based High-Throughput Nanomechanical Screening of Single Extracellular Vesicles. *Anal. Chem.* **92**, 10274–10282 (2020).
84. Dearnley, M. *et al.* Reversible host cell remodeling underpins deformability changes in malaria parasite sexual blood stages. *PNAS* **113**, 4800–4805 (2016).
85. Sisquella, X. *et al.* Plasmodium falciparum ligand binding to erythrocytes induce alterations in deformability essential for invasion. *eLife* **6**, e21083 (2017).
86. Perez-Guaita, D. *et al.* Multispectral Atomic Force Microscopy-Infrared Nano-Imaging of Malaria Infected Red Blood Cells. *Anal. Chem.* **90**, 3140–3148 (2018).
87. Ito, K. *et al.* Host Cell Prediction of Exosomes Using Morphological Features on Solid Surfaces Analyzed by Machine Learning. *J. Phys. Chem. B* **122**, 6224–6235 (2018).

88. Kikuchi, Y. *et al.* Diversity of physical properties of bacterial extracellular membrane vesicles revealed through atomic force microscopy phase imaging. *Nanoscale* **12**, 7950–7959 (2020).
89. Yokota, S. *et al.* Extracellular vesicles nanoarray technology: Immobilization of individual extracellular vesicles on nanopatterned polyethylene glycol-lipid conjugate brushes. *PLOS ONE* **14**, e0224091 (2019).
90. Tarca, A. L., Carey, V. J., Chen, X., Romero, R. & Drăghici, S. Machine Learning and Its Applications to Biology. *PLOS Computational Biology* **3**, e116 (2007).
91. Moen, E. *et al.* Deep learning for cellular image analysis. *Nature Methods* **16**, 1233–1246 (2019).
92. Gordon, O. M. & Moriarty, P. J. Machine learning at the (sub)atomic scale: next generation scanning probe microscopy. *Mach. Learn.: Sci. Technol.* **1**, 023001 (2020).
93. Minelli, E. *et al.* A fully-automated neural network analysis of AFM force-distance curves for cancer tissue diagnosis. *Appl. Phys. Lett.* **111**, 143701 (2017).
94. Barnard, A. S. *et al.* Nanoinformatics, and the big challenges for the science of small things. *Nanoscale* **11**, 19190–19201 (2019).
95. Gómez-de-Mariscal, E. *et al.* DeepImageJ: A user-friendly plugin to run deep learning models in ImageJ. *bioRxiv* 799270 (2019) doi:10.1101/799270.
96. Hothorn, T. CRAN Task View: Machine Learning & Statistical Learning. https://CRAN.R-project.org/view=MachineLearning (2020).
97. Machine Learning in MATLAB - MATLAB & Simulink. https://www.mathworks.com/help/stats/machine-learning-in-matlab.html (2020).
98. scikit-learn: machine learning in Python — scikit-learn 0.23.2 documentation. https://scikit-learn.org/stable/ (2020).
99. Van Deun, J. *et al.* EV-TRACK: transparent reporting and centralizing knowledge in extracellular vesicle research. *Nature Methods* **14**, 228–232 (2017).

100. Kalinin, S. V. *et al.* Big, Deep, and Smart Data in Scanning Probe Microscopy. *ACS Nano* **10**, 9068–9086 (2016).

# Chapter 5. Nanoscale Extracellular Vesicles Carry the Mechanobiology Signatures of Breast Cancer Cells

## 5.1 Abstract

Breast cancer cells secrete abundant nanometer-sized vesicles. Small extracellular vesicle (or sEV) cargos are known to have similar biomolecular signatures to their secreting parental breast cancer cells. However, whether malignant transformation modulates the physical and biomechanical profiles of secreted nanosized sEVs (40-120 nm) has not been established. Here, using multiparametric AFM imaging we directly compared the structure-mechanical properties (including topographic height, Young's modulus, and adhesion) of breast cancer cell-derived sEVs and secreting cells. Our findings reveal that sEVs show reduced Young's modulus concomitant with a decrease in cell stiffness as cells progress from non-tumor, to non-invasive, to invasive breast cancer phenotypes across different probing forces, isolation techniques, and particle sizes. Further, single sEV structure-mechanical analysis of actual patient plasma samples showed alterations in biomechanical properties of sEVs in breast cancer patients compared to sEVs from benign healthy controls. Our study demonstrates that precise biomechanical fingerprinting of single nanoscale sEVs provides an attractive label-free, cell-free, and orthogonal approach to detect changes in parental cells, such as during malignant transformation.

## 5.2 Introduction

Breast (and other) cancer cells abundantly secrete highly heterogeneous nanosized exosomes and other extracellular vesicles (EVs), ranging in diameter from ~30-1000 nm.[1] Malignant transformation,[2] micro-environmental stresses,[3,4] and therapeutic stresses[5] profoundly impact both the abundance and biomolecular cargo of EVs secreted by cells. Since EVs reflect the origin and state of the parental cells, they hold tremendous promise as cell-free disease biomarkers.[1,6] So far, efforts to understand the biomolecular cargoes of cancer-derived EVs have provided a wealth of information on the biogenesis, role and biomarker functions of EVs ensembles.[7,8] Because of the heterogeneity of nanometer-scale exosomes,[7,9] single EV methods such as fluorescence imaging,[10,11] flow cytometry of EVs enlarged *via* target-initiated engineering,[12] droplet-based enzyme-linked immunoassay,[13] digital detection integrated with surface-anchored nucleic acid amplification,[14] proximity-dependent barcoding assay[15] or immuno-droplet digital polymerase chain reaction[16] have been employed to understand the biomolecular makeup of individual EVs, as such information may be lost in bulk-level analyses. However, the label-free biophysical characteristics of single EVs abundantly secreted by breast cancer cells have not been established. In contrast to diagnostically significant biomechanical changes associated with cancer progression and metastasis at the single cell[17–19] and tissue levels[20,21] there is scant understanding of the biomechanical characteristics[22] of sub-cellular nanoscale breast cancer-derived EVs and the potential applicability from a diagnostic standpoint.

Atomic force microscopy (AFM)[23] provides an attractive nanoscale imaging and analysis technique[22,24] that has been successfully applied to probe the structure and mechanics of nano-liposomes[25] and cancer cell-derived small EVs (or sEVs; ~40-120 nm in diameter) in bladder,[26] hepatic,[27] and glioblastoma[28] *in vitro* cellular models and in patient saliva samples.[29,30] However, the impact of sEV isolation techniques or varying magnitudes and frequency of applied forces on elastic biomechanical properties of these nanosized vesicles has remained elusive. Furthermore, the feasibility of detecting biomechanical signatures of single sEVs in plasma or other biofluids has not been reported. Here, we directly compared the structure-mechanical properties (including simultaneously obtained AFM topographic height, Young's modulus, and adhesion) of nanosized breast cancer cell-derived sEVs and secreting cells using multiparametric AFM imaging and force spectroscopy.[22,29] Our findings reveal that single sEVs show altered biomechanical properties that correspond to the mechanical phenotypes of their parent-cells. Highly invasive and more mechanically compliant breast cancer cells secrete sEVs with reduced Young's modulus compared to non-tumor and less-invasive breast cancer cells. Furthermore, single sEV-like particle populations derived from breast cancer patient plasma further showed reduced Young's modulus associated with invasive breast cancer or ductal carcinoma *in situ* compared to benign samples.

Our proof-of-concept study provides evidence for differences in quantitative, label-free, single vesicle biomechanical fingerprints of breast cancer cell-derived sEVs and patient plasma sEV-like populations. The application of altered sEV biomechanical properties as orthogonal characteristics may further augment conventional biomolecular cargo analyses for EV-based cancer biomarker discovery.

## 5.3 Results & Discussion

### 5.3.1 sEVs show distinct mechanics and reflect the parent cell mechanical signatures:

To study the effect of malignant transformation on the biomechanical properties of breast cancer, we probed three well-established *in vitro* breast cancer cell line models of MCF10A (benign, non-tumorigenic human mammary epithelial cells); MCF-7 (none-to-moderate metastatic), and MDA-MB-231 (highly metastatic) as described[31] and their secreted sEVs. Cell mechanical properties were assessed based on AFM Young's modulus analysis on single, isolated cells grown in 2D cultures measured using single force-indentation curves obtained at 1Hz in contact mode. In line with previous reports,[32,33] MCF-7 cells were significantly stiffer ($P < 0.05$) compared to their metastatic, more invasive counterparts (MDA-MB-231) (**Figure 1A)** with average Young's modulus ($E$, KPa) values (mean ± SD) measured as 1.23 ± 0.31 kPa and 0.41 ± 0.14 kPa, respectively. MCF10A cells were most stiff with average Young's modulus value 2.11 ± 0.38 kPa. These results confirm the reduced overall elastic modulus of invasive breast cancer cells, compared to non-invasive, and benign epithelial mammary cell counterparts, under identical applied indentation forces.

Next, the biomechanical properties of sEVs derived from MCF10A, MCF-7 and MDA-MB-231 were evaluated using AFM nanoindentation, as shown in **Figure 2**. The sEV isolates were confirmed for the presence of vesicles using cryo-EM. AFM and light scatter nanoparticle size distributions showed particles within the expected size range, and protein markers for sEVs as outlined in **Supplemental Figure S1** and as described previously.[11] sEV isolates incubated on (3-Aminopropyl)- triethoxysilane-functionalized (AP-functionalized) mica substrates were imaged *via* AFM to locate single sEVs, prior to mechanical analysis (**Figure 1B**). Subsequently, force-indentation curves were used to derive Young's modulus of single sEVs.[22] Our results show that under identical forces of indentation, sucrose cushion ultracentrifugation-isolated MDA-MB-231 sEVs were ~40% more mechanically compliant than MCF-7 sEVs and had lower variance in Young's modulus (**Fig. 1B**) (P < 0.001) compared to MCF-7 sEVs across three independent experimental runs. More than 200 total curves were obtained over at least 40 individual similar-sized sEVs individually selected from multiple regions on the imaging substrate, for each of the three cell types. MCF10A sEVs had the highest elastic modulus (0.97 ± 0.07 MPa).

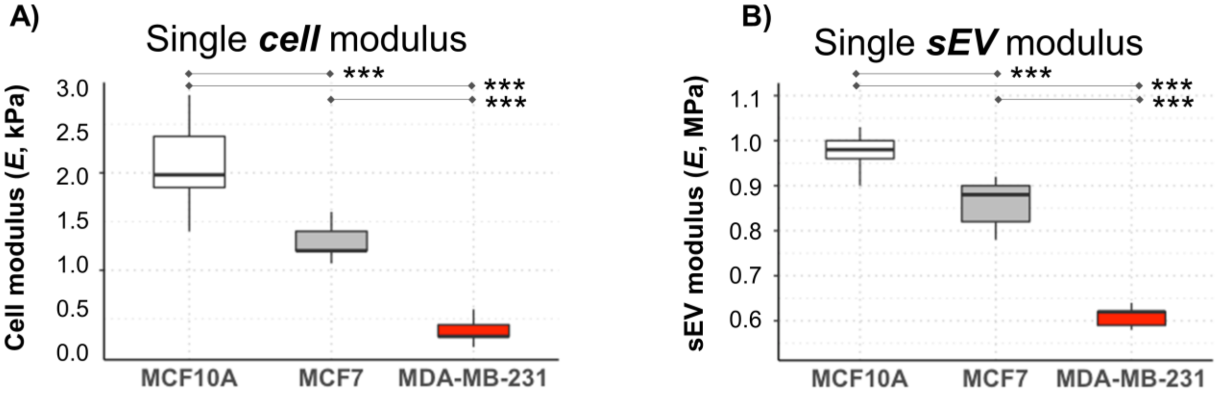

**Figure 1. Comparison of biomechanical properties (Young's modulus, E) of single breast cancer cells and corresponding small extracellular vesicles (sEV) using single AFM force-indentation analysis** A) Highly metastatic MDA-MB-231 cells show significantly lower average

cell modulus (*E*=0.41 ± 0.14 kPa) compared to low metastatic (MCF7 cells, *E*=1.23 ± 0.31 kPa) and non-metastatic (MCF10A, *E*=2.11 ± 0.38 kPa) cells ($p < 0.001$, represented by ***). B) In comparison, the sEVs obtained from highly metastatic MDA-MB-231 cells also show lower average sEV modulus (*E*= 0.61 ± 0.03 MPa) compared to those obtained from low metastatic (MCF7 sEVs, *E*=0.85 ± 0.07 MPa) and non-metastatic (MCF10A sEVs, *E*=0.97 ± 0.07 MPa) cells ($p < 0.001$, represented by ***). The findings demonstrate reduced Young's modulus of sEVs concomitant with a decrease in cell stiffness as cells progress from non-tumor, to non-invasive, to invasive breast cancer phenotypes. *P*-values were calculated by one-way ANOVA followed by Tukey post-hoc test.

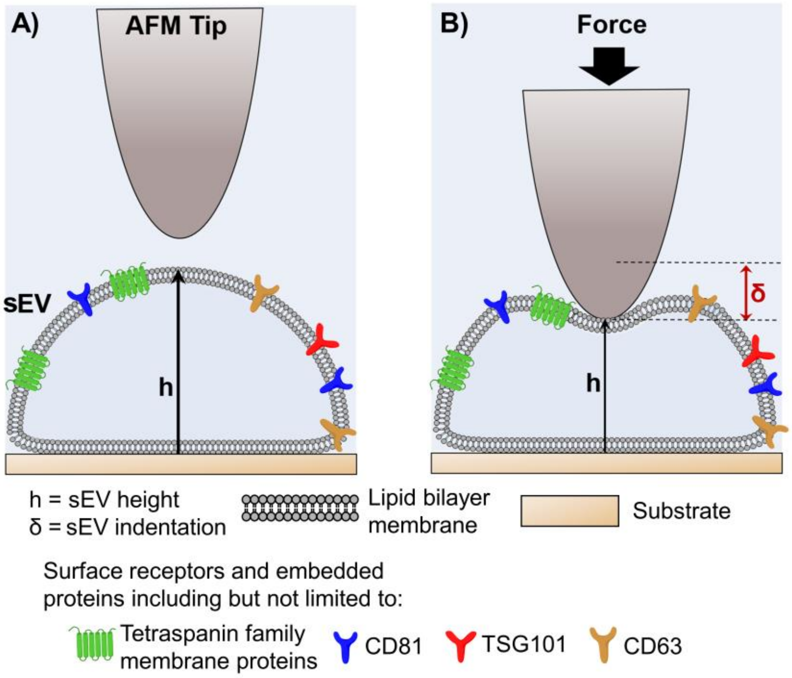

**Figure 2. Schematic of sEV indentation by AFM.** A) sEVs are comprised of a lipid bilayer membrane, with embedded proteins including tetraspanins and surface receptors such as CD81 and CD63. sEVs adhered to a relatively flat substrate adopt a hemispherical shape, with height h, before indentation by the AFM tip. B) The AFM tip indents the sEV and deforms the lipid bilayer membrane. The indentation depth, δ, is calculated as the difference between the vesicle's original height and its new height. A full workflow showing the calculation of Young's Modulus, adhesion, and fitting of indentation model is shown in **Supplemental Figure S4**.

Considering the impact of isolation methods on downstream EV imaging and analysis,[11] for instance, confounding differences in particle sizes, the presence of polymeric residues on isolated EVs, or presence of non-EV co-isolate contaminants, we tested the modulus findings among sEVs obtained from different isolation methods: immunoaffinity bead (IA), ultracentrifugation (UC), and sucrose cushion ultracentrifugation (UCg). As shown in **Figure 3**, across the three isolation methods, MDA-MB-231 sEVs were also more compliant to deformation compared to their MCF-7 sEV counterparts. To minimize the influence of heterogeneity in size of particles on measured mechanical properties, we compared the Young's modulus of sEVs across different sizes. Moreover, we show that the high-resolution structural characterization provides an accurate and localized overlay of nanomechanical features on lipid bilayer membrane-enclosed single sEVs, distinguishing them from other non-membranous or non-EV co-isolated components of similar size or shapes (**Figure 4**). Overall, our data demonstrated that the elastic modulus of sEVs derived from MCF10A, MCF-7, and MDA-MB-231 cells were significantly distinct and showed similar trends in mechanical profiles as the parental cells of origin, independent of isolation techniques measured for similar sized particles.

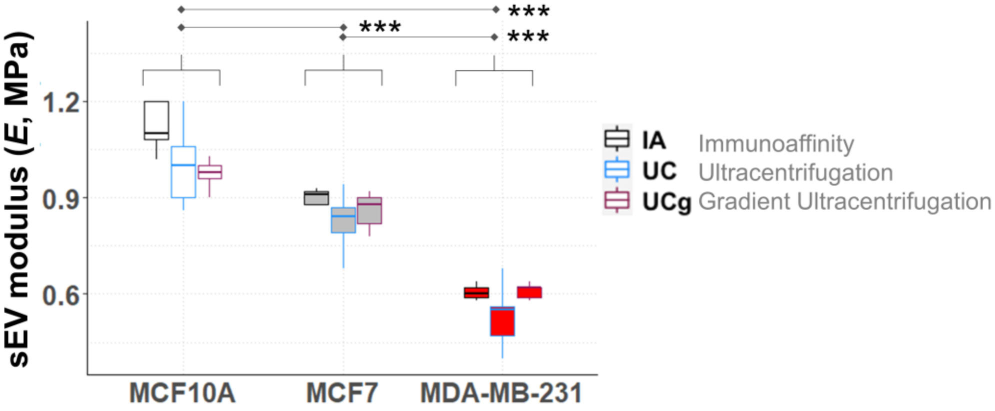

**Figure 3. Across different isolation methods, the biomechanical properties of cell-derived small extracellular vesicles (sEV) also show reduced Young's modulus from non-tumor, non-invasive, and to invasive breast cancer phenotypes.** sEVs were isolated from cell culture supernatants using immunoaffinity (IA), ultracentrifugation (UC) or sucrose cushion ultracentrifugation (UCg). The sEVs isolated from cells with high metastatic potential show lower modulus values ($p < 0.001$, indicated by ***). MCF10A sEVs isolated using IA (1.15 ± 0.13 MPa), UC (0.99 ± 0.09 MPa), or UCg (0.97 ± 0.07 MPa) show the highest Young's modulus values. MCF7 sEVs isolated using IA (0.90 ± 0.02 MPa), UC (0.83 ± 0.05 MPa) or UCg (0.85 ± 0.07 MPa) show a slight reduction in modulus compared to MCF10A. However, similar sized MDA-MB-231 sEVs isolated using IA (0.62 ± 0.09 MPa), UC (0.54 ± 0.09 MPa) or UCg (0.61 ± 0.03 MPa) all show significantly lower Young's Modulus values. To rule out the impact of variations in particle size on Young's modulus, or other co-existent non-EV aggregates, individual particles were

imaged before mechanical analysis. Similar sized particles (ranging in diameters 80-120 nm) were evaluated. Overall, sEVs from both cell lines show variations in modulus, however the MCF7 sEVs show overall higher modulus than MDA-MB-231 sEVs. *P*-values were calculated by one-way ANOVA followed by Tukey post-hoc test.

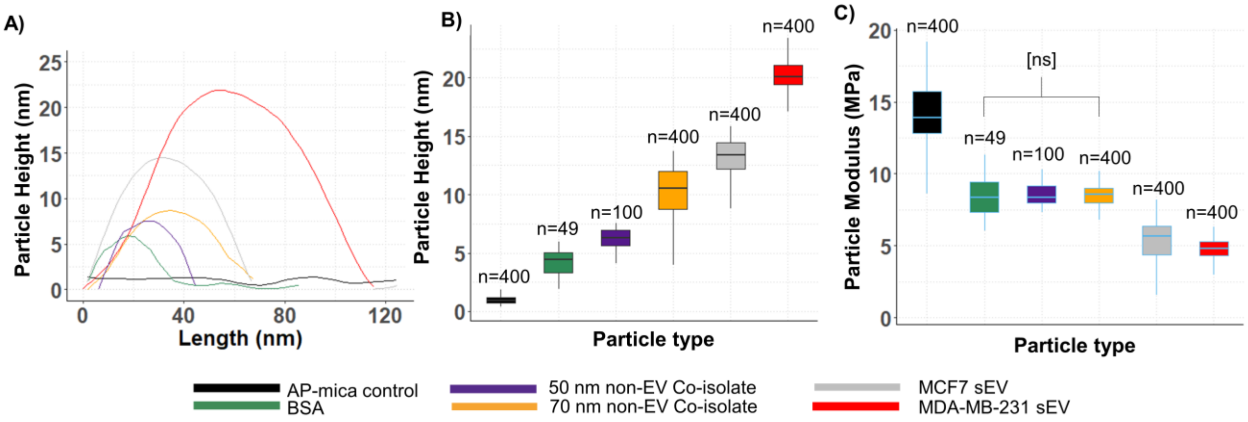

**Figure 4. Nanomechanical mapping combines structure, height, and mechanical properties to distinguish membrane single sEVs from other co-isolated particles.** A) Representative cross-sectional profiles for AP-functionalized mica substrates (black), compared to bovine serum albumin particles and small co-isolate showing relatively low height profiles (~5 nm) compared to lipid bilayer membrane limited MCF7 and MDA-MB-231 sEV isolates. Box plot representations show differences in particle heights (B) and Young's modulus (C) demonstrate that taller yet more mechanical compliant sEVs are distinct from other co-isolated particles and the relatively flat and stiff AP-functionalized mica substrates. All distributions in (B) and (C) are statistically significant from each other ($p > 0.05$) except the modulus obtained from BSA, the 50 nm non-EV co-isolates, and the 70 nm non-EV co-isolates marked with [ns]. (See Figure S2 for AFM images of structural features for co-isolates*.* *P*-values were calculated by one-way ANOVA followed by Tukey post-hoc test.)

### 5.3.2 Multi-parametric nanomechanical mapping confirms distinct mechanical signatures of breast cancer cell-derived sEVs:

Compared to single AFM indentation analysis as shown above (**Figure 1B**) where sEVs were first imaged and subsequently probed for mechanical properties, we further illustrated quantitative changes in the structure-mechanical properties of breast cancer-derived sEVs (isolated by the UCg method) using fast nanomechanical mapping. Here, using the off-resonance mode of the AFM for increased sensitivity, we combined simultaneous structural visualization and biomechanical analysis of single sEVs. Besides topography, we also mapped the derived elastic modulus, and measured the surface adhesion forces[34] to determine multi-parametric biophysical characteristics of sEVs derived from the two breast cancer cell types (**Figure 5)**. Since imaging forces directly impact not only topography but also the elastic behavior of membrane vesicles, the maximum imaging forces employed (two setpoint forces) were optimized to allow for successful tracking of particles immobilized on the surface. Such optimization allowed us to assess the elastic deformability of sEVs but without dislocating the sEV from the surface or rupturing the vesicle.

**Figure 5A-B** show representative maps for simultaneously obtained (i-ii) topography, (iii-iv) Young's modulus, and (v-vi) adhesion profiles obtained over individual similar sized MCF-7 and MDA-MB-231 sEVs respectively. We used two setpoint forces (*i.e.*, 1.25 nN and 2.0 nN marked in solid and broken lines respectively). The cross-section profiles were obtained across the lines (white, broken) marked on the sEVs in the corresponding panels. At both setpoint forces, the MDA-MB-231 sEV showed significantly reduced Young's modulus, *E* (**Figure 5B iii-iv**) and increased adhesion (**Figure 5B v-vi)** compared to the MCF-7 sEV (**Figure 5A, iii-vi**). **Figure 6** summarizes the differences observed in sEVs for the height, Young's modulus, and surface adhesion measurements (n=900 for each) obtained over the vesicle apical regions**.** Notably, despite the higher frequencies (2KHz) used for nanomechanical mapping of the sEVs using this AFM modality, in contrast to low frequency single force-indentation measurements (**Figure 1B**), the modulus results concur with sEVs from higher metastatic potential breast cancer cells showing significantly reduced Young's modulus at both force setpoints. The adhesion forces reflect non-specific binding of EV surface to the AFM probe. Overall, the MDA-MB-231 sEVs show reduced modulus and increased surface adhesion compared to the MCF-7 sEVs.

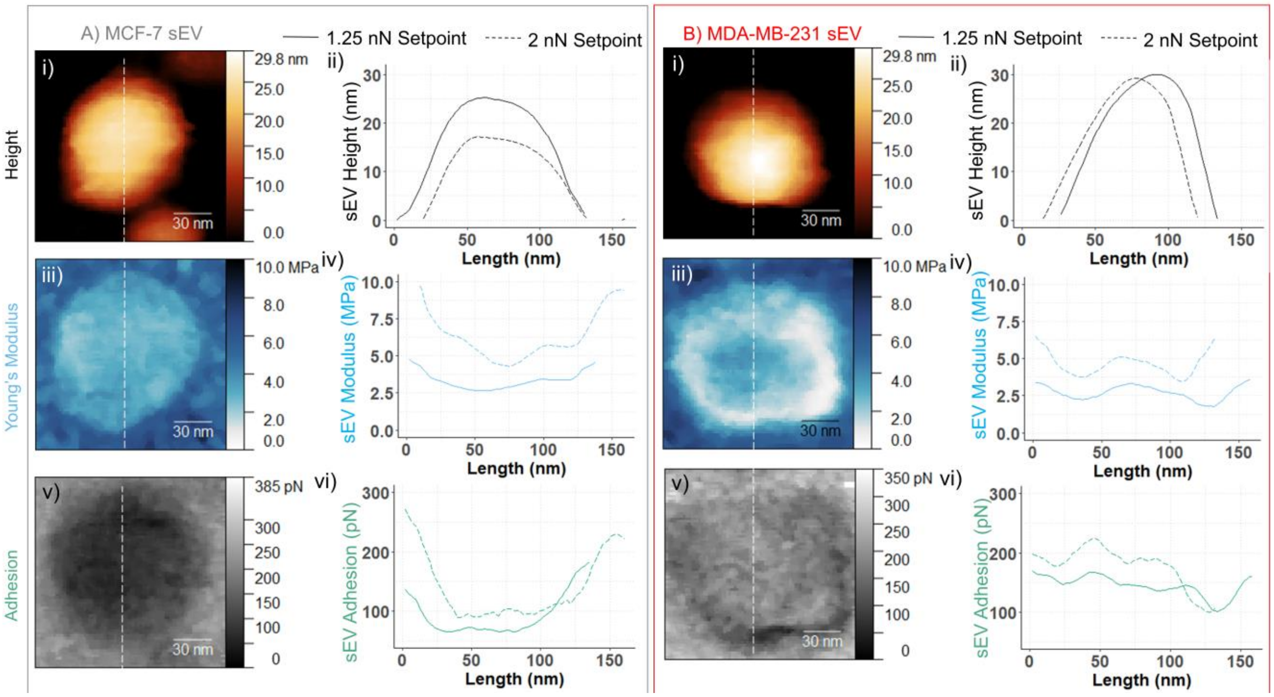

**Figure 5. Multi-parametric AFM nanomechanical mapping of single sEVs.** Representative maps of individual sEVs derived from breast cancer cell lines (A) MCF-7 and (B) MDA-MB-231, and corresponding cross-section profiles, marked with a broken white line, for (i-ii) height, (iii-iv) Young's modulus, and (v-vi) surface adhesion force. The MDA-MB-231 sEVs show lower Young's modulus and increased surface adhesion compared to the MCF-7 sEVs.

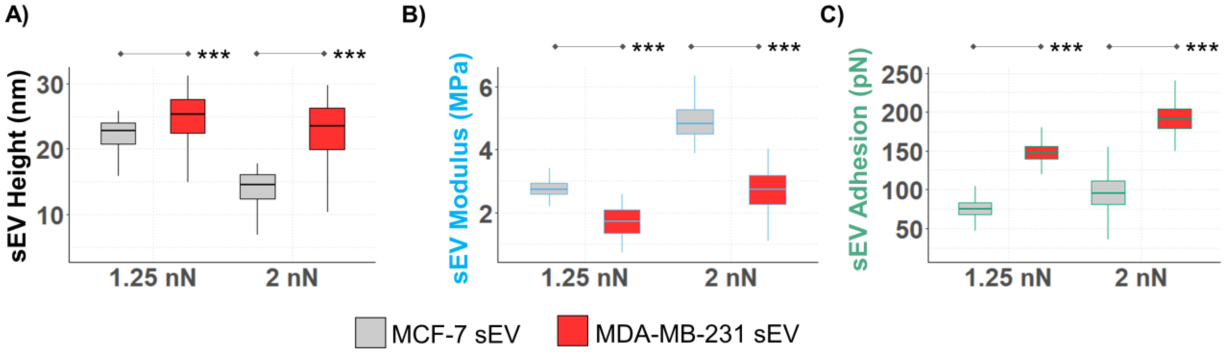

**Figure 6. Comparison of nanomechanical properties for breast cancer cell sEVs.** Box plots show differences in median ± std values for (A) height, (B) Young's modulus, and (C) surface adhesion forces between MCF-7 and MDA-MB-231 cell derived sEVs. Measurements were obtained from ~900 individual force-distance curves for each cell type at 1.25 and 2 nN imaging setpoint forces ($p < 0.001$, represented by ***). The sEVs from MDA-MB-231 cells show lower Young's modulus and increased surface adhesion compared to MCF-7 sEVs, for both the force setpoints used. *P*-values were calculated by one-way ANOVA followed by Tukey post-hoc test.

Previous studies from our group and others have identified the significance of EV biomechanical properties[26,27,35,36] as potential biomarkers for cancer[29] and other diseases.[37] However, sEV isolation methods,[11] size heterogeneity,[1] the presence of co-isolates,[8] as well as the magnitude and frequency of forces applied[29] which impact how sEVs deform[34] confound sEV nanomechanical analysis. Focusing on breast cancer progression, we demonstrate that nanomechanical properties can distinguish sEVs secreted from breast cancer cells varying in metastatic potential. Employing a comprehensive analysis of structural-mechanical profiles of individual sEVs, our results demonstrate that sEVs from invasive breast cancer cells were significantly softer compared to sEVs from non-invasive cells. The invasive cell-derived sEVs showed reduced Young's modulus, consistent across different isolation methods (**Figure 3**), indentation forces, and imaging frequencies. The Young's modulus values in our measurements using single force-indentation AFM measurements at low (1Hz) (**Figure 1B**) and high frequency (2KHz) nanomechanical mapping (**Figure 5**) agree with literature values reported for other biological and synthetic lipid vesicles,[34] validating the suitability of our nanomechanical measurements (**Figure 6**). We show that high-resolution nanomechanical mapping provides an accurate and localized overlay of nanomechanical features on single sEVs, distinguishing them from other non-EV co-isolated components of similar sizes or shape (**Figure 4**). In case of sEVs, while low imaging forces (150-250 pN) may result in small elastic deformations,[38] we chose higher setpoint forces (1.25 and 2 nN) to induce larger elastic deformations that more deeply indent the sEV lipid bilayer membrane without rupturing or irreversibly deforming the sEV. At both force setpoints, differences in the Young's modulus are observed (**Figure 6**), but at the 2 nN force setpoint MCF-7 sEVs and MDA-MB-231 sEVs exhibit greater differences in mechanical properties. No irreversible changes in the structural and mechanical integrity of sEVs were identified subsequent to nanomechanical mapping at both setpoint forces.

### 5.3.3 Preliminary evaluation of breast cancer plasma patient derived sEV-like particles shows altered biomechanical signatures:

Next, we evaluated the feasibility of structure-mechanical analysis of sEV-like particles in clinical breast cancer specimens using plasma samples obtained from histologically confirmed breast cancer patients.

Our preliminary evaluation (**Figure 7**) of plasma-isolated particles elucidates the heterogeneity in counts, size, and structural-biomechanical characteristics of sEV-like particles associated with breast cancer plasma compared to benign healthy controls. Particle counts obtained via AFM as described previously[11] show increased counts (**Figure 7A),** and increased particle diameters (**Figure 7B)** for invasive cancer compared to benign breast conditions and ductal *in situ* carcinoma (DCIS). In comparison, NTA particle counts were also elevated in cancer patient plasma (**Figure S3 iv**). While increased EV counts and more heterogeneous size populations have been previously reported in breast cancer patient plasma,[39] corresponding spatial biomechanical properties on single sEV-like particles from plasma had not been established. Here, we introduced multi-parametric nanomechanical mapping to determine the high-resolution structure and mechanical properties of individual sEV-like particles in plasma. Single sEV-like particles isolated from benign plasma samples showed round morphology (**Figure 7C-i**) compared to the irregularly shaped particles observed from invasive breast cancer patient plasma (**Figure 7C-ii**), as shown in representative topographic height images. The corresponding modulus panels show higher Young's modulus for benign plasma particles (**Figure 7C-iii**) compared to the softer invasive breast cancer plasma isolated sEV-like particles (**Figure 7C-iv**). A quantitative analysis of plasma-isolated sEV-like particles showed no-significant differences in mean heights between benign, DCIS and invasive breast cancer sample derived particles (**Figure 7D-i**). However, the particle modulus values were significantly lower (47% decrease) for invasive and DCIS samples compared to the benign counterparts ($p < 0.001$) (**Figure 7D-ii**). Together, our findings from the pilot patient plasma study reveal distinctly altered biomechanical properties among sEV-like particles from benign (non-cancer) and breast cancer plasma.

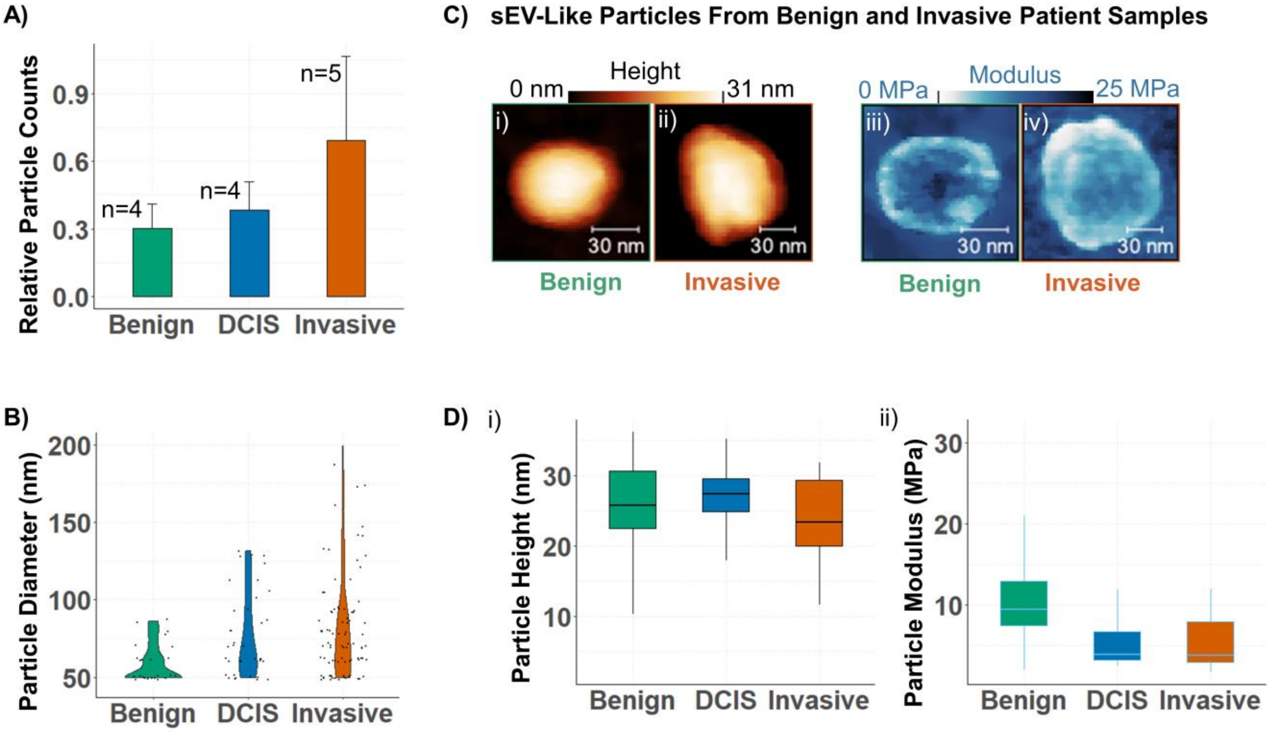

**Figure 7. Preliminary AFM nanomechanical mapping based evaluation of plasma sEV-like particles.** Single sEV-like particles isolated from invasive breast cancer plasma show both (A) higher relative particle counts and (B) wider particle size distribution via AFM compared to benign and DCIS samples. (C) Representative single sEV-like particles from benign (i) and invasive (ii) breast cancer plasma display round and irregularly shaped morphology, respectively. (iii-iv) Corresponding images show higher Young's modulus distributions in benign compared to invasive breast cancer plasma EV-like particles (D) Quantitative analysis of the mean particle (i) heights and (ii) differences in Young's modulus values determined for particles from benign, DCIS, and invasive breast cancer samples ($p < 0.001$). *P*-values were calculated by one-way ANOVA followed by Tukey post-hoc test.

Nevertheless, plasma is a complex bio-fluid containing highly heterogeneous vesicle populations, proteins and other biomolecules.[40] Naturally, plasma samples require more stringent protocols for sEV isolation from platelet-depleted samples.[41,42] In comparison to other ensemble biomolecular characterization techniques, the ability to visualize the phenotype of each individual particle measured in our AFM analysis allows improved sensitivity and reliability of our sEV measurements. Plasma-derived sEV-like particles display distinct biomechanical profiles (**Figure S3**) and thus can still be identified from non-EV co-isolates of similar morphology and diameters as in **Figure 4**.

Ultimately, the biomechanical properties of cells and sEVs stem from their geometry and molecular composition. The changes in biomechanical properties of cancer cells[17] are widely associated with altered cytoskeleton rearrangements,[32,43] nuclear lamina,[44] and integrins.[45] The biomechanical changes in cancer EVs[29,38] which are approximately 1,100,000-140,100,000 times smaller than the volume of cells are also likely to be influenced by the nature and abundance of transmembrane proteins and other proteins[46] as well as restricted vesicle geometry.[47] Several studies have shown reduced cell stiffness with increasing metastatic efficiency in human cancer cells. Cross et al. first reported that metastatic cells derived from the pleural fluids of patients with suspected lung, breast, and pancreatic cancer are 70% softer compared to the benign control cells.[17] Mechanistically, the elastic properties of living cells are mainly determined by the cellular actin cytoskeleton.[32,43] In the case of EVs secreted by cancer cells, one might also expect changes in the protein content embedded within the membrane vesicles to directly affect the mechanical properties of similar sized vesicles. Compared to liposomes, natural vesicles show increased stiffness mainly attributed to the presence of membrane proteins.[48] Also, Vorselen et al. found a 40% decrease in stiffness in red blood cell-derived EVs from patients with hereditary spherocytosis compared to healthy donor samples.[37] They attributed the observed differences in stiffness to differences in the protein content, thus it is plausible that the changes in membrane-embedded proteins in metastatic tumor cell-derived EVs compared to their nonmetastatic counterparts could explain decreased stiffness in cancer-derived EVs. We have reported in this manuscript a proteomic analysis of isolated sEVs that identified more than 280 proteins. This list includes multiple cytoskeletal and signaling proteins known to directly impact biomechanical phenotypes (**Figure S1D**).

Previously, using single molecule force spectroscopy our group reported structural and bio-molecular differences between normal and tumor-derived saliva exosomes[30] and demonstrated the enrichment of specific proteins present in the membranes of tumor-derived vesicles as determined by a functionalized AFM probe with an antibody specific to the CD63 exosome marker protein. We also reported differences between glioblastoma cell-derived exosomes and normal exosomes.[28] Subsequently, Whitehead et al. showed mechanical variations in metastatic and nonmetastatic bladder cell-derived exosomes.[26] However, an inverse relationship between EV stiffness softness and malignancy has also been reported.[36] Overall, the enhancement of EVs with specific protein cargoes by tumor cells into their surrounding microenvironment has been reported in several studies, and can influence tumor growth and metastasis. While further studies are needed for in-depth evaluation of the biomechanical characteristics of EVs derived from other types of cells to identify the possible changes related to tumors and other diseases, including single molecule force spectroscopy using tip functionalized with antibodies specific to EV surface proteins our study clearly shows the mechanical signatures of breast cancer cell and plasma derived EVs.

Further investigation is needed to determine whether or not altered biomechanical properties of sEVs play important functional roles in cancer progression or if they merely manifest themselves as diagnostic signals, and to determine whether or not altered biomechanical properties of secreted sEVs are displayed in other cancers with diagnostic utility. In either case, our work provides a persuasive proof-of-concept for AFM-based nanomechanical mapping as a quantitative metric for label-free, orthogonal profiling of cancer-derived sEVs. Quantifying altered biomechanical signatures of secreted sEVs may be a clinically applicable predictor of cancer progression or invasion. AFM remains the gold standard for assessing the mechanical signature of patient-derived cancer cells,[17] and for single sEVs as demonstrated in the current study. The small sample volume required for AFM analysis of sEV isolates is suitable for assessing limited volume patient biofluid samples. High speed AFM and automation,[49,50] as well as the implementation of machine learning methods[34] now enable identification of patterns and features of sEV biophysical properties in AFM datasets that are clinically relevant.[51] In addition, clinically useful microfluidic platforms capable of sorting cells based on their stiffness[52] have been previously described. The development of similar platforms to sort sEVs by stiffness could be easily multiplexed with existing microfluidic platforms which analyze sEV protein, DNA, and mRNA cargo and have been successfully employed in biofluids.[53] Such methods could be utilized independently to select sEVs of potential cancerous origin from patient plasma in clinical settings for proteomic analysis[54] or used to select specific sEV subpopulations for mechanical profiling.

## 5.4 Conclusions

Using single AFM force-indentation analysis and nanomechanical mapping we compared the structural-mechanical properties of invasive and noninvasive nanosized breast cancer sEVs along with their corresponding parental cells. Our findings reveal that secreted sEVs reflect the biomechanical signatures of parent breast cancer cells that vary in metastatic potential. sEVs derived from soft, invasive breast cancer cells were also significantly softer compared to sEVs derived from stiff, non-invasive breast cancer cells, demonstrating that biomechanical fingerprinting of single EVs is an attractive label-free orthogonal approach to assess the state of the parental cells, such as during malignant transformation. These biomolecular changes in single sEVs that manifest as alterations in key nanoscale structural-mechanical EV fingerprints promise new opportunities for orthogonal, label-free sEV based biomarkers. Here we demonstrated the feasibility of single sEV structure-mechanical measurements in breast cancer patient plasma. Besides an increase in particle counts and size, nanoscale sEVs derived from breast cancer patient plasma also showed altered biomechanical properties that match the trends observed in *in vitro* models. Together, our results demonstrate the promise of structure-mechanical fingerprinting of sEVs as an attractive high-resolution, label-free, orthogonal approach at the nanoscale to detect changes in parental cells, such as during malignant transformation, opening new avenues towards breast cancer biomarkers.

## 5.5 Materials and Methods

*Cell cultures*:

To examine the biophysical characteristics of secreted small extracellular vesicles (sEVs), we first isolated sEVs from three cultured cells that represent different metastatic potentials. We chose MCF10A (human mammary epithelial cells) and MCF-7 and MDA-MB-231 cells, which are well-established breast cancer cell lines from the American Type Culture Collection (Manassas, VA) as described previously.[31] MCF-7 cells are tumorigenic but non-metastatic and represent the low metastatic potential. MDA-MB-231 cells are highly metastatic, with altered adhesion and motility properties.

*Cell Culture EV isolation*:

Breast cancer cell lines were cultured in Dulbecco's modified eagles medium (DMEM; Gibco, Thermo Fischer Scientific, Carlsbad CA) supplemented with 10% fetal bovine serum (Atlanta Biologicals), 100U/ml penicillin, and 100µg/ml streptomycin, in a 5% CO2 humidified atmosphere at 37°C and were cultured in six 60 mm Petri dishes (Corning, CA). FBS-originated-exosome-free media was prepared per protocol by Théry: FBS was ultra-centrifuged at 100,000 g for 2 hours at 4ºC, then filtered with a 0.22 µm sterile filter. After 48 hours of incubation in DMEM supplemented with 10% exosome-free FBS, cell viability of 70-80% was confirmed and the media containing EVs were isolated.[55] The total cell count was 2 x$10^7$ and 24 mL of EV-containing media was obtained. EV isolation was performed using ultracentrifugation (UC), 30% sucrose cushion ultracentrifugation (UCg), or immunoaffinity bead (IA) as described previously.[11,56]

*Quality control for cell cultures and chemicals employed*

Mycoplasma or other microbes can release vesicles interfering with the purity and characterization of sEVs. Therefore, we employed rigorous testing of any contamination of the cells, cell culture media, other reagents, or chemicals. Cell cultures (ATCC) were regularly tested and found negative for mycoplasma contamination using the culture medium (Mycoplasma broth, Millipore Sigma) and microscopic analysis. Additionally, EV-depleted media was also evaluated microscopically to validate the depletion of sEV-sized particles. Further, since a full depletion of EVs may not be possible, as per the recommendations of the ISEV guidelines,[57] we used fresh media not cultured with cells and a blank buffer as controls. Based on MALS and AFM particle sizing, no particulate materials within the size range of sEVs were detectable in these controls. Additionally, consistent cell seeding protocols and cell viability tests were used across multiple EV isolation runs (n>3) to ensure the reproducibility and quality of the isolated sEVs. All chemicals, buffers and other reagents used were molecular grade.

*AFM nanomechanical analysis of single cells*:

Single cell mechanical measurements were obtained on breast cancer cells cultured on 60 mm tissue culture dishes (Corning) as described previously.[43] Cells that stained positive for Annexin V (Sigma-Aldrich) as an indicator of apoptosis, were excluded from the analysis. All measurements were conducted at 37°C using a Catalyst atomic force microscope (Bruker Instruments, Santa Barbara, CA) using a combined inverted optical/confocal microscope (Zeiss, Corp, Thornwood, NY) that permits lateral positioning of the AFM tip over the cell center with submicron precision. AFM measurements were collected in contact mode using silicon nitride cantilevers (MLCT, Bruker Ltd., CA) with experimentally determined spring constants of 0.02 N/m and a tip radius of ~20 nm. Force-displacement curves were recorded at 1Hz for the determination of Young's modulus. Conversion of force-displacement curves to force-indentation curves allows the determination of the local cell surface elastic modulus or “stiffness” (Young's modulus, E). AFM measurements were obtained in at least 60 cells in three different experiments.

*AFM nanomechanical analysis of single sEVs*:

For sEV mechanics, 10 µL of 10% (3-Aminopropyl) triethoxysilane or AP solution was incubated with clean, freshly cleaved mica discs in a vacuum chamber overnight. Nitrogen gas was purged, and the mica discs were stored in a nitrogen gas chamber; 50 µL of the EV samples were incubated over AP-modified mica surfaces for 10 min. To remove unbound sEVs, mica was washed with PBS four times; 50 µL of PBS was added on mica before imaging. AFM images were taken at 256 samples per line, at 0.6 Hz to locate single sEVs prior to indentation measurements. At least sixty force-displacement curves were recorded over EVs (n >30) for each sample in three different experiments using contact mode at setpoint force of 1nN at 1Hz (using MLCT probes, Bruker Ltd. CA). The Young's modulus (E, MPa) was calculated by converting the force curves into force indentation curves and fit with the Hertz-Sneddon thin-film model using the full length of the force-indentation curve from the point of contact to the maximum force setpoint.[58] Both single cell and EV single force indentation data were processed using SPIP$^{TM}$.

*Simultaneous AFM based structure-mechanics mapping of breast cancer cell sEVs*:

20 µL of isolated sEV samples were incubated over AP-modified mica substrates for 3 min. To remove unbound sEVs, substrates were washed twice with 50 µL PBS and imaging in PBS. Measurements were conducted in PBS using a Dimension FastScan Microscope (Bruker Instruments, Santa Barbara, CA) in off-resonance tapping mode, with ScanAsyst Fluid tips (Bruker, CA) with radius ~20 nm and experimentally determined spring constants of 0.7 N/m. AFM images were taken at 256 samples per line, at 0.75 Hz, at optimal force setpoints of 1.25 nN and 2 nN. Images were exported offline and processed using Gwyddion. Images were flattened with a second-order polynomial for the height channel, and a first-order polynomial for the Young's Modulus and Adhesion channels as described previously.[34] The Young's modulus (E, MPa) was calculated using the Hertz-Sneddon thin film model using the full length of the force-indentation curve from the point of contact to the maximum force setpoint. Cross-sections were taken horizontally across the middle of the sEV images using x, y coordinates to align cross-sections

across all channels. The box plots show data obtained from 30 pixels by 30-pixel area (~3500 nm$^2$) at the apical region of the sEVs, using XY coordinates to align the covered area across all channels (**Figure S4**).

*Plasma sEV-like particle isolation, AFM nanomechanical measurements, and data analysis*:

Human plasma samples were collected from six newly diagnosed breast cancer patients and three non-cancer patients, matched for age and gender. Samples were obtained prior to surgery or neoadjuvant therapy. The main clinical characteristics of all samples are reported in **Supplemental Table S1.** Written informed consent was obtained from all subjects [in accordance with IRB protocol; IRB # 20-001197]. All samples were acquired through the collection of whole blood in ethylenediaminetetraacetic acid (EDTA) tubes. After blood collection, the samples were spun at 3,000 RPM (Eppendorf Centrifuge 5810 No. 0012529- rotor A-4-81) for 10 min. Samples were stored in 1ml aliquots at - 80ºC until further processing. Samples were thawed and centrifuged at 10,000g for 30 minutes to remove large (micron sized) extracellular vesicles. sEV-like particles were isolated from the supernatant using the IA method as described previously.[11] Isolated sEV-like samples were prepared on AP-modified mica and nanomechanical mapping was performed by AFM as above. Patient plasma sEV-like particle diameters and relative counts were obtained from AFM images using grain analysis function on 8 μm × 8 μm height images obtained at a resolution of 256 samples per line, at 0.75 Hz.[11]

*Statistical Analysis*:

Data were expressed as mean values ± standard deviations. Their statistical significance was identified by the Student's t-test or one-way analysis of variance (ANOVA) (Origin 8.0, OriginLab Corporation, Northampton, Massachusetts) for the differences among breast cancer cells and EVs. *P*-values of less than 0.05 was considered to be statistically significant. For multi-parametric sEV analysis, each feature was summarized by cell type and imaging force set-points in terms of means, standard deviations, and quartiles. We used one- and two-way ANOVA models followed by Tukey post-hoc test to compare features between cell types at different imaging force set points using the rstatix package in R. *P*-values < 0.05 were considered statistically significant. Principal Component Analysis (PCA) was used to transform the number of potentially correlated variables and interpret the data. We selected the minimum number of components to explain at least 50% of the variation in the features and presented the data in a PCA scatter plot, clustering observations by cell type and imaging force (**See Supplemental Figure S5)**. These analyses were performed using SAS v. 9.4 (SAS Institute Inc., Cary, NC).

## 5.6 Supplementary Information

**5.6.1. Verification of membrane vesicles in the expected size range of 40-120nm diameter and particle-size distributions for breast cancer cell line derived sEVs:** The cell culture derived EV isolates used for this study were confirmed for the presence of lipid bilayer membrane bound vesicles using TF20 High-Resolution CryoEM (FEI) (**Figure S1A**). Particle sizes for different isolates were determined using AFM imaging and nanoparticle tracking analysis (**Figure S1B and C** respectively). These measurements were consistent with orthogonal particle size distributions obtained using Resistive Pulse sensing and optical interference-based analysis and as described previously. The ExoCheck EV antibody array was used to confirm the presence of EVs isolated from MCF7 and MDA-MB-231 cells (**Figure S1D)**, utilizing common sEV external surface markers (CD63, EpCAM, ANXA5, CD81, ICAM) and internal markers (TSG101, ALIX, and FLOT1), as well as GM130 cis-Golgi marker to monitor any cellular contamination. Mass spectrometric proteomic analysis of breast cancer cell derived sEV isolates by cellular component (**Figure S1E)** shows enriched small extracellular vesicles, exosomes, and the presence of plasma membrane, cytoskeleton and extracellular proteins.

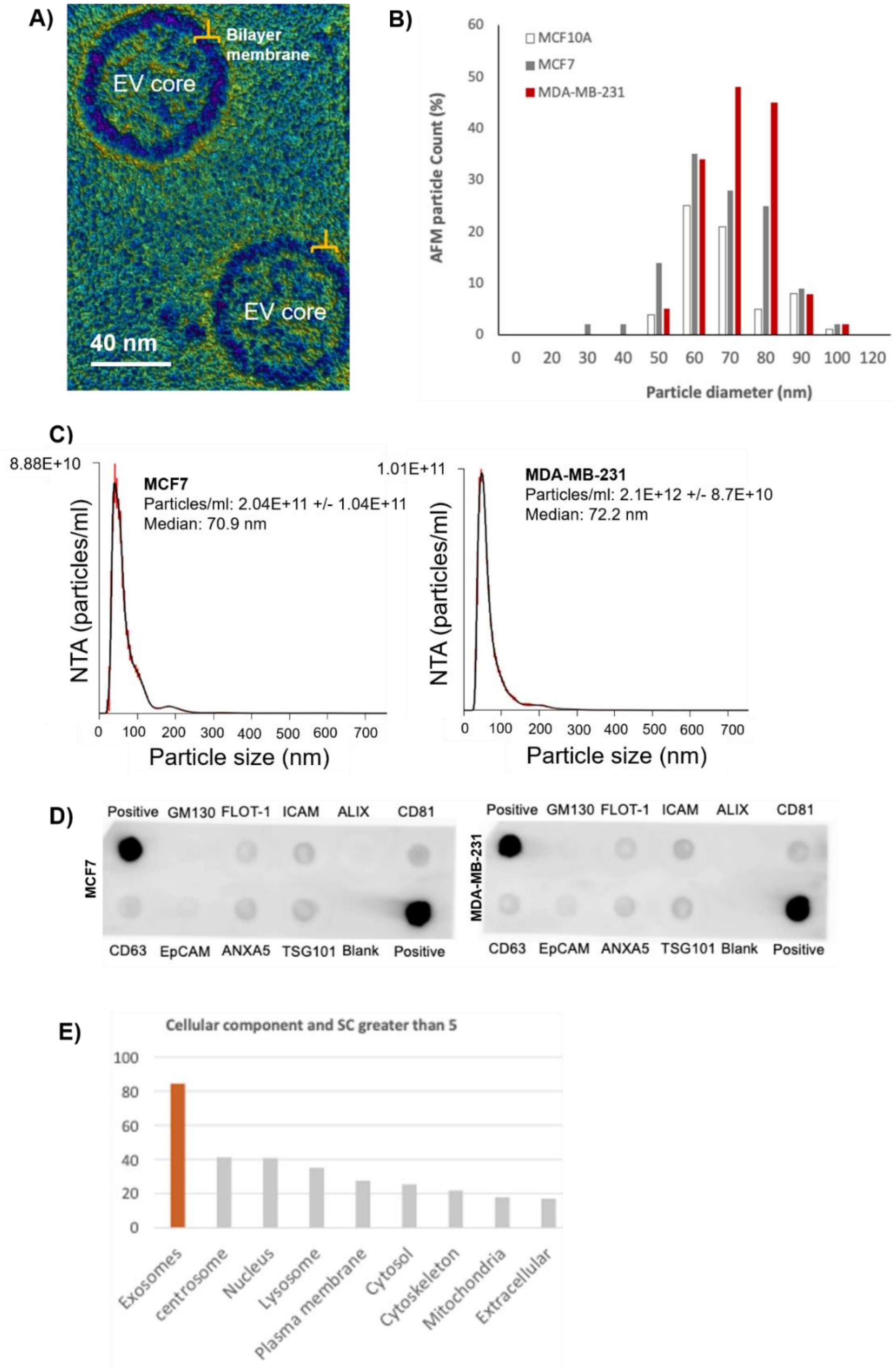

**Figure S1. Breast cancer cell line derived sEV characterization.** A) Verification of lipid bilayer membrane bound vesicles in breast cancer cell derived sEV isolates using cryo-EM. The lipid bilayer membrane shows a distinct contrast compared to the lumen of the vesicle. B) AFM particle counts showing higher counts in MCF7 and MDA-MB-231 compared to MCF-10A cells in the expected 60-100nm sEV size range. C) NTA of sEVs showing particles per ml and median particle diameters. The black line shows the best-fitting curve. Red line represents the error bar. Shown is a representative chart of three independent repeats. D) Exo-Check EV antibody array of five external (CD63, EpCAM, ANXA5, CD81, and ICAM) and three internal (TSG101, ALIX, and FLOT1) protein markers in EVs isolated from MCF7 and MDA-MB-231 cells. Other markers include GM130 cis-Golgi marker to monitor any cellular contamination in sEV isolations, a labeled positive control for HRP detection, and a blank spot as a background control. E) Mass spectrometric proteomic analysis of breast cancer cell derived sEV isolates. Cellular components show enriched small extracellular vesicles, exosomes, and the presence of plasma membrane, cytoskeleton and extracellular proteins.

### 5.6.2. Identification features sEVs from non-sEVs *via* AFM nanomechanical mapping.

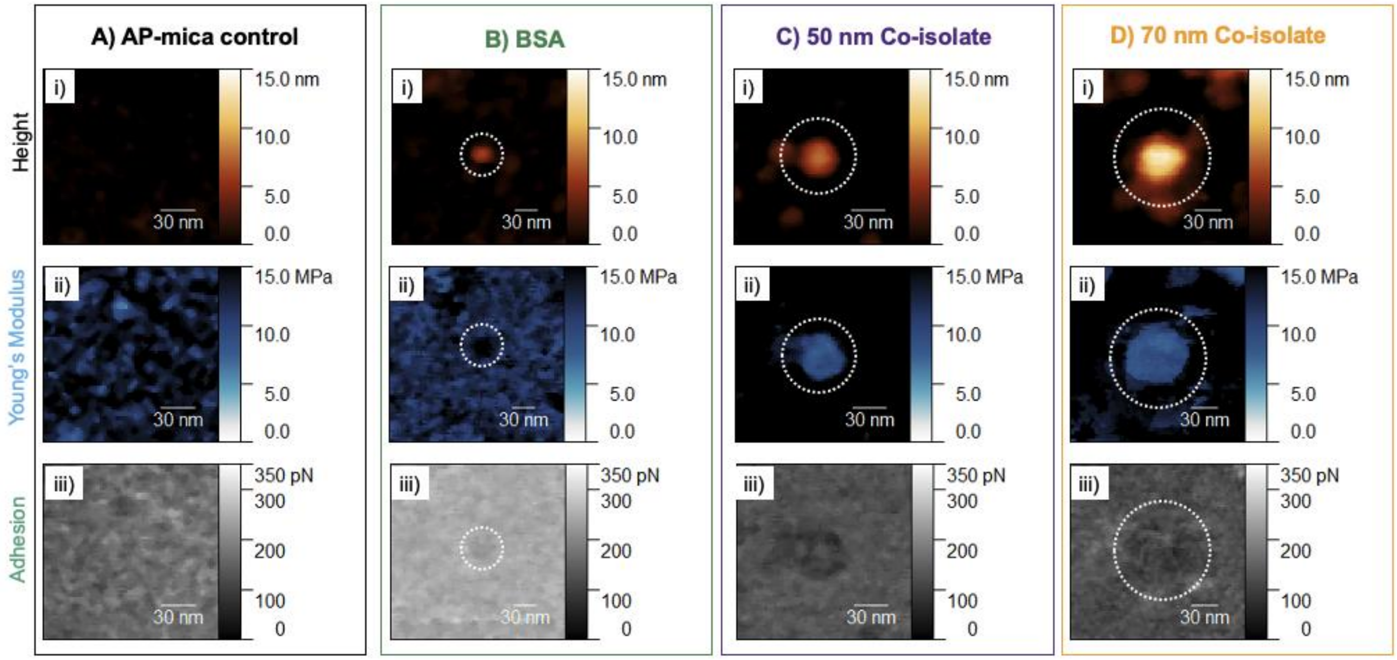

**Figure S2. Localized overlay of AFM structural-nanomechanical features (i.e., height, shape, size, and Young's modulus) together allow differentiation of single EVs from other non-EV co-isolated components of similar size or shape**. Representative AFM images of (A) (3-Aminopropyl) triethoxysilane (APTES)-functionalized mica substrate, (B) isolated BSA control particle, and (C-D) small non-membrane bound particles with diameters similar to single sEVs, For each sample, the (i) height, (ii) Young's Modulus, and (iii) adhesion force are shown.

### 5.6.3. AFM based counts and topographic height variations in sEV-like particles in patient plasma.

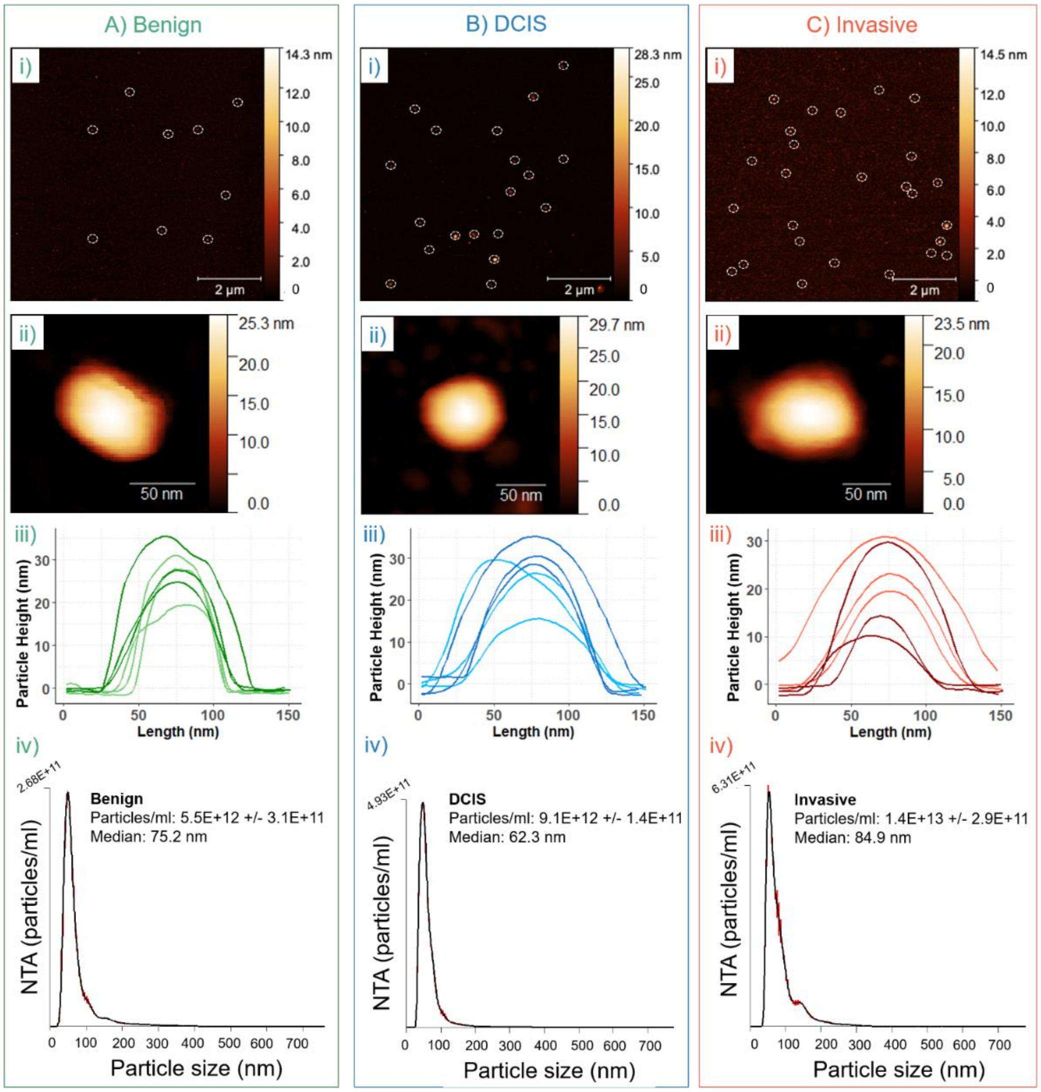

**Figure S3. Representative images and cross-sections for (A) Benign (B) DCIS and (C) Invasive patient plasma sample derived sEVs**. (i) Representative wide field images (8 x 8 µm, 256 samples per line) of patient plasma sEV-like particles. Larger sEV-like particles are marked with a white dashed circle. (ii) Representative images of single sEV-like particles. (iii) Height cross-sections for three single sEVs from two patients of each histological classification show varying height and diameter for all samples. (iv) NTA of plasma sEVs showing particles per ml and median particle diameters. The black line shows the best-fitting curve. Red line represents the error bar. Shown is a representative chart of three independent repeats.

### 5.6.4. AFM indentation analysis of sEVs workflow.

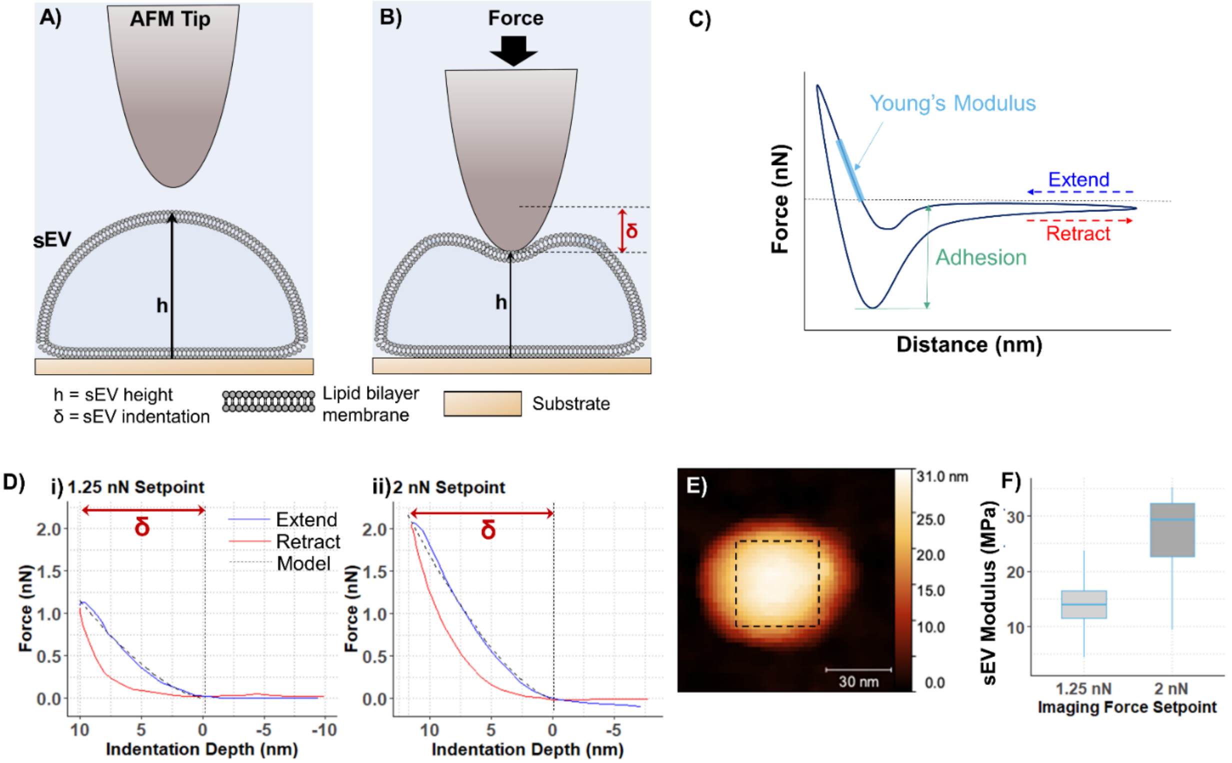

**Figure S4. AFM indentation analysis workflow.** A) sEVs adhered to a relatively flat substrate adopt a hemispherical shape, with height h, before indentation by the AFM tip. B) The AFM tip indents the sEV and deforms the lipid bilayer membrane. The indentation depth, δ, is calculated as the difference between the vesicle's original height and its new height. C) An individual force-distance curve showing EV mechanical response to indentation as described previously (see reference 34). D) Representative force-distance curves show varying sEV indentation depths. i) Lower force setpoint, 1.25 nN. ii) Higher force setpoint, 2 nN E) Apical region of the sEV, identified in the height channel. F) Simultaneously obtained height, modulus, and adhesion values from the apical region of the sEV are represented as box plots. The median is shown as a solid line within the colored box, and the two ends of the box mark the 25th percentile (Q1) and the 75th percentile (Q3). The lines extending from the box show the spread of values below the 25th percentile and above the 75th percentile.

### 5.6.5. Comparison of AFM based nanomechanical properties for breast cancer cell derived sEVs.

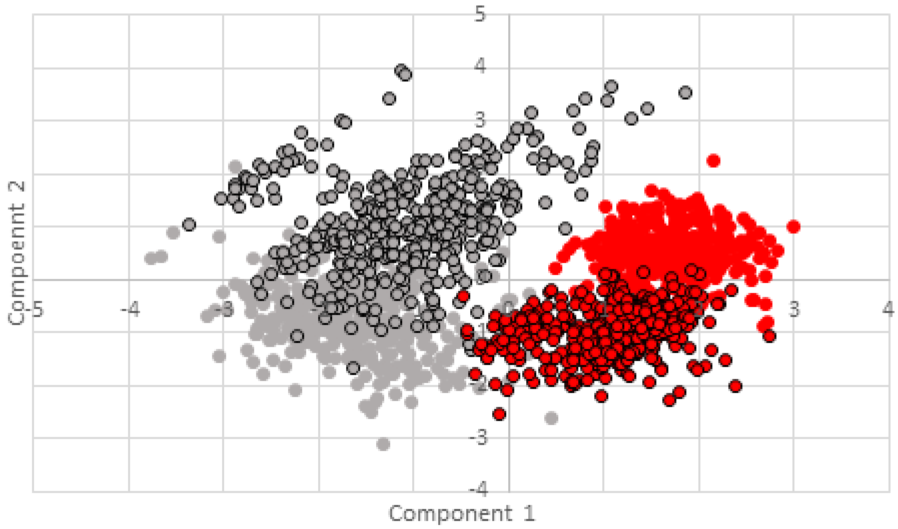

**Figure S5. Principal component analysis shows separation of clusters based on breast cancer metastatic potential**. Component one separates cell types, while component two separates imaging force, though the directions are flipped, representing the cell type and imaging force interaction.

**TABLE S1. Specific Patient Characteristics.**

| No. | Age/sex | Clinical History | Cytological/Histology |
|---|---|---|---|
| 1 | 68/F | Benign breast with sclerosing adenosis | Benign |
| 2 | 45/F | Benign fibrosis tissue with small fibroadenoma | Benign |
| 3 | 26/F | Benign/stromal fibrosis and fibroadenomatoid nodule | Benign |
| 4 | 64/F | DCIS | DCIS |
| 5 | 68/F | DCIS | DCIS |
| 6 | 64/F | DCIS | DCIS |
| 7 | 59/F | T2N1aMx | Invasive |
| 8 | 47/F | IDC, T1bN0 | Invasive |
| 9 | 47/F | T3N1aMx | Invasive |

### 5.7 References:

1. Kalluri, R. & LeBleu, V. S. The biology, function, and biomedical applications of exosomes. *Science* **367**, (2020).
2. Choi, D. *et al.* Extracellular vesicle communication pathways as regulatory targets of oncogenic transformation. *Semin Cell Dev Biol* **67**, 11–22 (2017).
3. Hoshino, A. *et al.* Tumour exosome integrins determine organotropic metastasis. *Nature* **527**, 329–335 (2015).
4. Harmati, M. *et al.* Small extracellular vesicles convey the stress-induced adaptive responses of melanoma cells. *Scientific Reports* **9**, 15329 (2019).
5. O'Neill, C. P., Gilligan, K. E. & Dwyer, R. M. Role of Extracellular Vesicles (EVs) in Cell Stress Response and Resistance to Cancer Therapy. *Cancers (Basel)* **11**, (2019).
6. Wen, S. W. *et al.* Breast Cancer-Derived Exosomes Reflect the Cell-of-Origin Phenotype. *Proteomics* **19**, e1800180 (2019).
7. Jeppesen, D. K. *et al.* Reassessment of Exosome Composition. *Cell* **177**, 428-445.e18 (2019).
8. Zhang, H. *et al.* Identification of distinct nanoparticles and subsets of extracellular vesicles by asymmetric-flow field-flow fractionation. *Nat Cell Biol* **20**, 332–343 (2018).
9. Choi, D. *et al.* Mapping Subpopulations of Cancer Cell-Derived Extracellular Vesicles and Particles by Nano-Flow Cytometry. *ACS Nano* **13**, 10499–10511 (2019).
10. Panagopoulou, M. S., Wark, A. W., Birch, D. J. S. & Gregory, C. D. Phenotypic analysis of extracellular vesicles: a review on the applications of fluorescence. *J Extracell Vesicles* **9**,.
11. Sharma, S., LeClaire, M., Wohlschlegel, J. & Gimzewski, J. Impact of isolation methods on the biophysical heterogeneity of single extracellular vesicles. *Scientific Reports* **10**, 13327 (2020).
12. Shen, W. *et al.* A Single Extracellular Vesicle (EV) Flow Cytometry Approach to Reveal EV Heterogeneity. *Angewandte Chemie International Edition* **57**, 15675–15680 (2018).

13. Liu, C. *et al.* Single-Exosome-Counting Immunoassays for Cancer Diagnostics. *Nano Lett* **18**, 4226–4232 (2018).
14. Tian, Q. *et al.* Nanoparticle Counting by Microscopic Digital Detection: Selective Quantitative Analysis of Exosomes via Surface-Anchored Nucleic Acid Amplification. *Anal Chem* **90**, 6556–6562 (2018).
15. Wu, D. *et al.* Profiling surface proteins on individual exosomes using a proximity barcoding assay. *Nature Communications* **10**, 3854 (2019).
16. Ko, J. *et al.* Single Extracellular Vesicle Protein Analysis Using Immuno-Droplet Digital Polymerase Chain Reaction Amplification. *Advanced Biosystems* **4**, 1900307 (2020).
17. Cross, S. E., Jin, Y.-S., Rao, J. & Gimzewski, J. K. Nanomechanical analysis of cells from cancer patients. *Nat Nanotechnol* **2**, 780–783 (2007).
18. Dokukin, M. E., Guz, N. V., Gaikwad, R. M., Woodworth, C. D. & Sokolov, I. Cell surface as a fractal: normal and cancerous cervical cells demonstrate different fractal behavior of surface adhesion maps at the nanoscale. *Phys Rev Lett* **107**, 028101 (2011).
19. Iyer, S., Gaikwad, R. M., Subba-Rao, V., Woodworth, C. D. & Sokolov, I. AFM Detects Differences in the Surface Brush of Normal and Cancerous Cervical Cells. *Nat Nanotechnol* **4**, 389–393 (2009).
20. Plodinec, M. *et al.* The nanomechanical signature of breast cancer. *Nat Nanotechnol* **7**, 757–765 (2012).
21. Sharma, S., Aguilera, R., Rao, J. & Gimzewski, J. K. Piezoelectric needle sensor reveals mechanical heterogeneity in human thyroid tissue lesions. *Scientific Reports* **9**, 9282 (2019).
22. Krieg, M. *et al.* Atomic force microscopy-based mechanobiology. *Nature Reviews Physics* **1**, 41–57 (2019).
23. Binnig, G., Quate, C. F. & Gerber, Ch. Atomic Force Microscope. *Phys. Rev. Lett.* **56**, 930–933 (1986).

24. Sharma, S., LeClaire, M. & Gimzewski, J. K. Ascent of atomic force microscopy as a nanoanalytical tool for exosomes and other extracellular vesicles. *Nanotechnology* **29**, 132001 (2018).
25. Ramachandran, S., Quist, A. P., Kumar, S. & Lal, R. Cisplatin Nanoliposomes for Cancer Therapy:  AFM and Fluorescence Imaging of Cisplatin Encapsulation, Stability, Cellular Uptake, and Toxicity. *Langmuir* **22**, 8156–8162 (2006).
26. Whitehead, B. *et al.* Tumour exosomes display differential mechanical and complement activation properties dependent on malignant state: implications in endothelial leakiness. *J Extracell Vesicles* **4**, (2015).
27. Royo, F. *et al.* Differences in the metabolite composition and mechanical properties of extracellular vesicles secreted by hepatic cellular models. *J Extracell Vesicles* **8**, (2019).
28. Sharma, S., Das, K., Woo, J. & Gimzewski, J. K. Nanofilaments on glioblastoma exosomes revealed by peak force microscopy. *J R Soc Interface* **11**, 20131150 (2014).
29. Sharma, S. *et al.* Structural-Mechanical Characterization of Nanoparticle Exosomes in Human Saliva, Using Correlative AFM, FESEM, and Force Spectroscopy. *ACS Nano* **4**, 1921–1926 (2010).
30. Sharma, S., Gillespie, B. M., Palanisamy, V. & Gimzewski, J. K. Quantitative Nanostructural and Single Molecule Force Spectroscopy bio-molecular analysis of human saliva derived exosomes. *Langmuir* **27**, 14394–14400 (2011).
31. Neve, R. M. *et al.* A collection of breast cancer cell lines for the study of functionally distinct cancer subtypes. *Cancer Cell* **10**, 515–527 (2006).
32. Cross, S. E. *et al.* AFM-based analysis of human metastatic cancer cells. *Nanotechnology* **19**, 384003 (2008).
33. Lekka, M. *et al.* Cancer cell recognition – Mechanical phenotype. *Micron* **43**, 1259–1266 (2012).

34. LeClaire, M., Gimzewski, J. & Sharma, S. A review of the biomechanical properties of single extracellular vesicles. *Nano Select* **2**, 1–15 (2021).
35. Kikuchi, Y. *et al.* Diversity of physical properties of bacterial extracellular membrane vesicles revealed through atomic force microscopy phase imaging. *Nanoscale* **12**, 7950–7959 (2020).
36. Yurtsever, A. *et al.* Structural and mechanical characteristics of exosomes from osteosarcoma cells explored by 3D-atomic force microscopy. *Nanoscale* **13**, 6661–6677 (2021).
37. Vorselen, D. *et al.* The fluid membrane determines mechanics of erythrocyte extracellular vesicles and is softened in hereditary spherocytosis. *Nature Communications* **9**, 4960 (2018).
38. Ridolfi, A. *et al.* AFM-Based High-Throughput Nanomechanical Screening of Single Extracellular Vesicles. *Anal. Chem.* **92**, 10274–10282 (2020).
39. König, L. *et al.* Elevated levels of extracellular vesicles are associated with therapy failure and disease progression in breast cancer patients undergoing neoadjuvant chemotherapy. *OncoImmunology* **7**, e1376153 (2018).
40. Palviainen, M. *et al.* Extracellular vesicles from human plasma and serum are carriers of extravesicular cargo—Implications for biomarker discovery. *PLOS ONE* **15**, e0236439 (2020).
41. Witwer, K. W. *et al.* Standardization of sample collection, isolation and analysis methods in extracellular vesicle research. *Journal of Extracellular Vesicles* **2**, 20360 (2013).
42. Mateescu, B. *et al.* Obstacles and opportunities in the functional analysis of extracellular vesicle RNA – an ISEV position paper. *Journal of Extracellular Vesicles* **6**, 1286095 (2017).
43. Sharma, S. *et al.* Correlative nanomechanical profiling with super-resolution F-actin imaging reveals novel insights into mechanisms of cisplatin resistance in ovarian cancer cells. *Nanomedicine: Nanotechnology, Biology and Medicine* **8**, 757–766 (2012).

44. Pajerowski, J. D., Dahl, K. N., Zhong, F. L., Sammak, P. J. & Discher, D. E. Physical plasticity of the nucleus in stem cell differentiation. *Proc Natl Acad Sci U S A* **104**, 15619–15624 (2007).
45. Wirtz, D., Konstantopoulos, K. & Searson, P. C. The physics of cancer: the role of physical interactions and mechanical forces in metastasis. *Nat Rev Cancer* **11**, 512–522 (2011).
46. Piffoux, M., Silva, A. K. A., Wilhelm, C., Gazeau, F. & Tareste, D. Modification of Extracellular Vesicles by Fusion with Liposomes for the Design of Personalized Biogenic Drug Delivery Systems. *ACS Nano* **12**, 6830–6842 (2018).
47. Dimitrievski, K. Deformation of Adsorbed Lipid Vesicles as a Function of Vesicle Size. *Langmuir* **26**, 3008–3011 (2010).
48. Calò, A. *et al.* Force measurements on natural membrane nanovesicles reveal a composition-independent, high Young's modulus. *Nanoscale* **6**, 2275–2285 (2014).
49. Ando, T. High-speed atomic force microscopy and its future prospects. *Biophys Rev* **10**, 285–292 (2017).
50. Mikheikin, A. *et al.* DNA nanomapping using CRISPR-Cas9 as a programmable nanoparticle. *Nature Communications* **8**, 1665 (2017).
51. Sokolov, I. *et al.* Noninvasive diagnostic imaging using machine-learning analysis of nanoresolution images of cell surfaces: Detection of bladder cancer. *Proc Natl Acad Sci U S A* **115**, 12920–12925 (2018).
52. Islam, M. *et al.* Microfluidic cell sorting by stiffness to examine heterogenic responses of cancer cells to chemotherapy. *Cell Death Dis* **9**, (2018).
53. Contreras-Naranjo, J. C., Wu, H.-J. & Ugaz, V. M. Microfluidics for exosome isolation and analysis: Enabling liquid biopsy for personalized medicine. *Lab Chip* **17**, 3558–3577 (2017).
54. Hoshino, A. *et al.* Extracellular Vesicle and Particle Biomarkers Define Multiple Human Cancers. *Cell* **182**, 1044-1061.e18 (2020).

55. Théry, C., Amigorena, S., Raposo, G. & Clayton, A. Isolation and characterization of exosomes from cell culture supernatants and biological fluids. *Curr Protoc Cell Biol* **Chapter 3**, Unit 3.22 (2006).
56. Gupta, S. *et al.* An improvised one-step sucrose cushion ultracentrifugation method for exosome isolation from culture supernatants of mesenchymal stem cells. *Stem Cell Research & Therapy* **9**, 180 (2018).
57. Théry, C. *et al.* Minimal information for studies of extracellular vesicles 2018 (MISEV2018): a position statement of the International Society for Extracellular Vesicles and update of the MISEV2014 guidelines. *Journal of Extracellular Vesicles* **7**, 1535750 (2018).
58. Sharma, S., Palanisamy, V., Mathisen, C., Schmidt, M. & Gimzewski, J. K. Exosomes-biological liposomes as potential drug delivery agents. *Global Journal of Physical Chemistry* **2**, 4 (2011).

# Chapter 6. Nanoscale Imaging and Analysis of Cerebrospinal Fluid-Derived Single EVs

## 6.1 Abstract

Extracellular vesicles (EVs) have attracted attention as potential biomarkers for various diseases because they are found ubiquitously in biofluids such as cerebrospinal fluid (CSF), and offer an attractive alternative to tissue biopsies, especially for invasive procedures such as brain tumor biopsies. Here, we report the first high-resolution structural and mechanical analysis of CSF-derived single EVs. Our results demonstrate the ability of AFM to successfully elucidate sEV nano-metrics including count, size distribution, and biomechanical properties in CSF using minimal sample volume, without the need to pool samples.

## 6.2 Introduction

Although neuroimaging is an important modality in the diagnosis of brain tumors, it is not unambiguous, and direct access to brain tissues through biopsy or surgery is burdened with medical risks, ethical considerations, sampling errors due to tumor heterogeneity, and offers but a snapshot of the inherently dynamic process of tumor growth.[1,2] Therefore, there is a critical unmet need for the development of orthogonal circulating biomarkers, such as extracellular vesicles (EVs), that can be used not only to diagnose, but also to monitor disease progression on therapy.

EVs[3] are 30 - <1,000-nanometer particles secreted into the extracellular environment by a wide range of normal mammalian cells.[4,5] EVs are known to play a role in intercellular communication.[6] EVs also harbor oncoproteins and other diagnostically important elements of GBM transcriptome, genome and lipidome.[7–9] The presence and high stability of EVs in blood and cerebrospinal fluid (CSF), combined with their bio-molecular composition that mirrors the intra-tumoral environment, highlights their applicability as circulating biomarkers for glioma diagnosis and therapeutic monitoring.[2,8,10]

While it is increasingly evident that EVs circulating in body fluids such as CSF may provide unique and assessable ‘nanoscale windows’ into brain tumors, the low abundance and nanometer scale dimensions of EVs pose unique challenges. Uncertainties exist with respect to impact of different isolation techniques employed, as well as rigor and reliability of EV characterization.[11,12] Moreover, often there is a need for economizing CSF samples by pooling individual CSF volumes for downstream biomolecular analysis.[13] Together, pre-analytical variabilities arising from variability in EV isolation techniques[13–15] and limited CSF volume availability in patient samples limit the adequacy of commonly used characterization tools to probe nanometer-sized and highly heterogeneous EVs in CSF. Compared to proteomic and genomic cargo analysis of CSF-derived EVs, information on quantitative, high resolution, structural-mechanical properties of CSF EV isolates, and the impact of isolation techniques, is scarce.

Here, using atomic force microscopy (AFM)[16,17] as a sub-nm imaging and force manipulation tool for single EVs,[18] we report the first high-resolution structural and mechanical analysis of CSF-derived single EVs. First, we demonstrate the applicability of AFM-based single EV analysis as an efficient, quantitative tool to study the abundance, structure, and biomechanical properties of CSF-derived single EVs in a label-free manner. These biophysical properties largely remain obscured in the ensemble or other characterization techniques due to detection limits of particle size or concentration inherent in most analytical techniques employed. Second, using minimal (less than 1 milliliter) volumes of CSF, we successfully compared EVs isolated via different isolation methods within the same patient samples, in replicates.

### 6.3 Results & Discussion

CSF samples were obtained from four patients undergoing lumber puncture or shunt at UCLA Medical Centre. Written informed consents were obtained from all subjects as per UCLA IRB approved study protocol (IRB#10-000655). The 1 mL volume samples were centrifuged at 10,000 g for 30 mins at 4°C to remove microvesicles and cell debris. EVs were isolated using size exclusion chromatography (SEC) using Izon qEV Original (35 nm resin pore) column, precipitation by ExoQuick-TC (PT), or a combination of the two (SECPT) as outlined in **Supplemental Figure S1**.

First, we evaluated the feasibility of determining the structure-mechanical properties of CSF-derived single sEVs using AFM nanomechanical mapping.[19] Small EVs (sEVs) isolated by SEC or SECPT were incubated on (3-Aminopropyl) triethoxysilane (AP)-modified mica substrates and imaged under PBS conditions with ScanAsyst Fluid tips (Bruker, CA) with radius ~20 nm and experimentally determined spring constants of 0.7 N/m. Using the off-resonance mode of a Dimension FastScan AFM (Bruker Instruments, Santa Barbara, CA) for increased sensitivity, we combined simultaneous structural visualization and biomechanical analysis of single sEVs. A representative single sEV-like particle isolated from CSF sample shows round, oblate morphology (**Figure 1**) Besides topography, we also mapped the mechanical deformation of sEVs, the localized surface modulus corresponding to small indentation, and the Young's modulus corresponding to deeper indentations, to determine previously undetermined multi-parametric biophysical characteristics of CSF derived sEVs (**Figure 1A)**. The maximum imaging force employed (setpoint force) was optimized to allow for successful tracking of particles immobilized on the surface with minimal mechanical perturbation. **Figure 1B** shows representative maps for simultaneously obtained (i) topography, (ii) localized surface modulus, (iii) Young's modulus, and (iii) deformation profiles obtained over an individual sEV obtained from patient CSF sample. The cross-section profiles, aligned using XY coordinates across all channels, were obtained across the lines (white, broken) marked on the sEVs in the corresponding panels. Typical heights of single EVs ranged between 20 and 30 nm (**Figure 1B-i; and C-i)**. We resolved the localized surface modulus (**Figure 1B-ii and C-ii**), Young's modulus (**Figure 1B-iii and C-iii**), and deformability (**Figure 1B-iv; and C-iv)** of single sEVs, revealing areas of increased localized surface modulus on the apical region of the sEV membrane which potentially arise from residual polymeric matrix. The well-resolved high-resolution images establish the suitability of our AFM nanomechanical approach to evaluate clinical CSF samples.

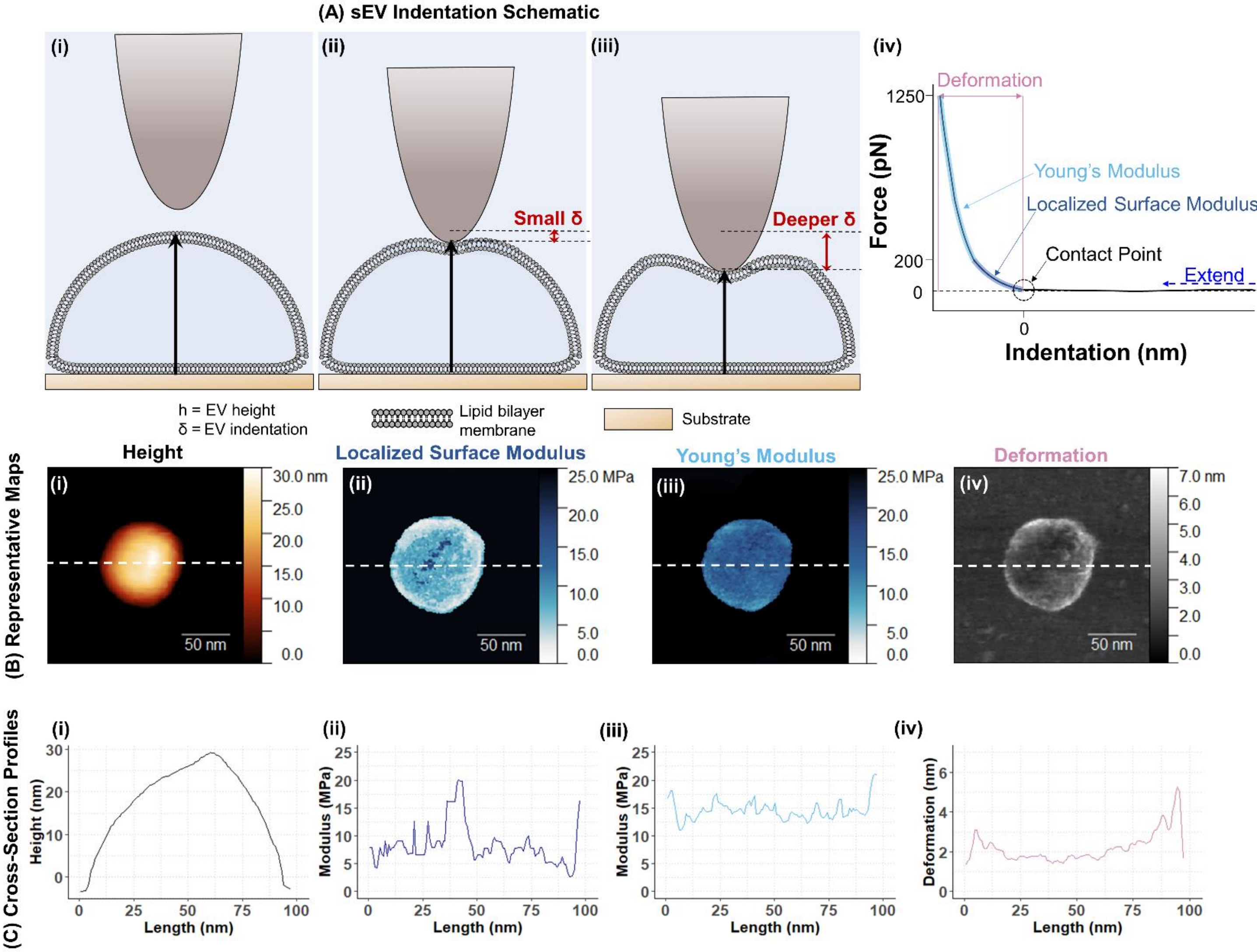

**Figure 1. AFM imaging of CSF-derived sEVs.** (A) Indentation schematic of an sEV's response to the applied force of an AFM tip. (i) Initially, the tip is far from the sEV, and the sEV adopts a hemispherical shape with height h on the relatively flat surface. (ii) The AFM tip begins to indent the sEV and slightly deforms the membrane. The indentation depth, δ, is calculated as the difference between the vesicle's original height and new height. The small indentation is used in the calculation of the localized surface modulus. (iii) The AFM tip indents the sEV further, to a set force setpoint, from which the Young's modulus is calculated. (B) Representative maps of EVs derived from CSF patient samples, and (C) corresponding cross-section profiles, marked with a broken white line, for (i) height, (ii) localized surface modulus, (iii) Young's modulus and

(iv) deformation. The sEV is round, and relatively flat except for a small raised area. The localized surface modulus image shows areas of increased stiffness across the center of the sEV, while the Young's modulus image shows uniform modulus across the sEV. The Young's modulus profile and the localized surface profile show high and low modulus values at the same coordinates on the sEV, with the exception of a spike in localized surface modulus near the center of the sEV.

**Table 1. Biophysical characteristics of CSF sEV isolates.**

| Sample | Isolation Method | Particle Count (Particles/um$^2$) (Mean ± Error) | Size (nm) (Mean ± STDEV) | RMS Surface Roughness (nm) (Mean) | Localized Surface Modulus (MPa) (Mean ± STDEV) | Young's Modulus (MPa) (Mean ± STDEV) |
|---|---|---|---|---|---|---|
| CSF-1<br>GBM leptomeningeal | SEC | 4.2 ± 0.5 | 67.0 ± 25.8 | 2.42 | 2.40 ± 1.12 | 4.84 ± 0.51 |
| | SECPT | 4.8 ± 0.3 | 55.5 ± 11.0 | 1.75 | 7.62 ± 2.51 | 18.98 ± 2.29 |
| | PT | 10.8 ± 4.4 | 57.3 ± 12.5 | 2.17 | - | - |
| CSF-2<br>GBM hydrocephalus | SEC | 1.4 ± 0.3 | 68.1 ± 21.7 | 3.03 | 7.75 ± 3.48 | 7.31 ± 1.58 |
| | SECPT | 1.4 ± 0.4 | 64.1 ± 20.9 | 2.95 | 11.62 ± 5.03 | 14.49 ± 1.73 |
| | PT | 6.6 ± 2.5 | 72.4 ± 30.8 | 3.78 | - | - |
| CSF-3<br>Lung adenocarcinoma | SEC | 1.5 ± 0.1 | 62.8 ± 22.9 | 2.46 | 4.01 ± 1.37 | 8.62 ± 2.13 |
| | SECPT | 3.80 ± 0.1 | 65.7 ± 26.3 | 2.95 | 2.76 ± 0.88 | 7.09 ± 1.39 |
| | PT | 7.0 ± 2.0 | 63.0 ± 18.2 | 2.50 | - | - |
| CSF-4<br>Metastatic cervical cancer | SEC | 3.1 ± 2.4 | 61.4 ± 15.9 | 1.82 | 3.48 ± 3.08 | 7.88 ± 4.46 |
| | SECPT | 5.4 ± 0.8 | 65.9 ± 24.6 | 1.90 | 15.15 ± 7.31 | 17.69 ± 2.83 |
| | PT | 2.7 ± 0.4 | 61.7 ± 18.7 | 2.55 | - | - |

Robust characterization of sEVs serves as the foundation for any downstream applications. Additionally, the choice of isolation method impacts the quantity and quality of sEV isolates,[12] complicating the optimization of sEV isolation from low abundance, limited volume samples such as CSF. We therefore leveraged the minimal sample volume requirements of AFM imaging to evaluate variabilities in CSF sEVs across different isolation techniques. We employed SEC, PT, and SECPT isolation methods in parallel for rigorous characterization and yield maximization. Our preliminary evaluation of CSF-derived particles elucidates the heterogeneity in key sEV nano-metrics (**Table 1)** including counts, size distributions, and structural-biomechanical characteristics of sEV-like particles associated with GBM CSF compared to non-cancer, lung and cervical metastatic cancer CSF (**Figure 2**) sEVs compared across isolation techniques. The RMS Roughness, and the Young's modulus and localized surface modulus distributions were obtained from 20 pixel by 20-pixel area (~1500 $nm^2$) at the apical region of the EVs, using XY coordinates to align the covered area across all channels.

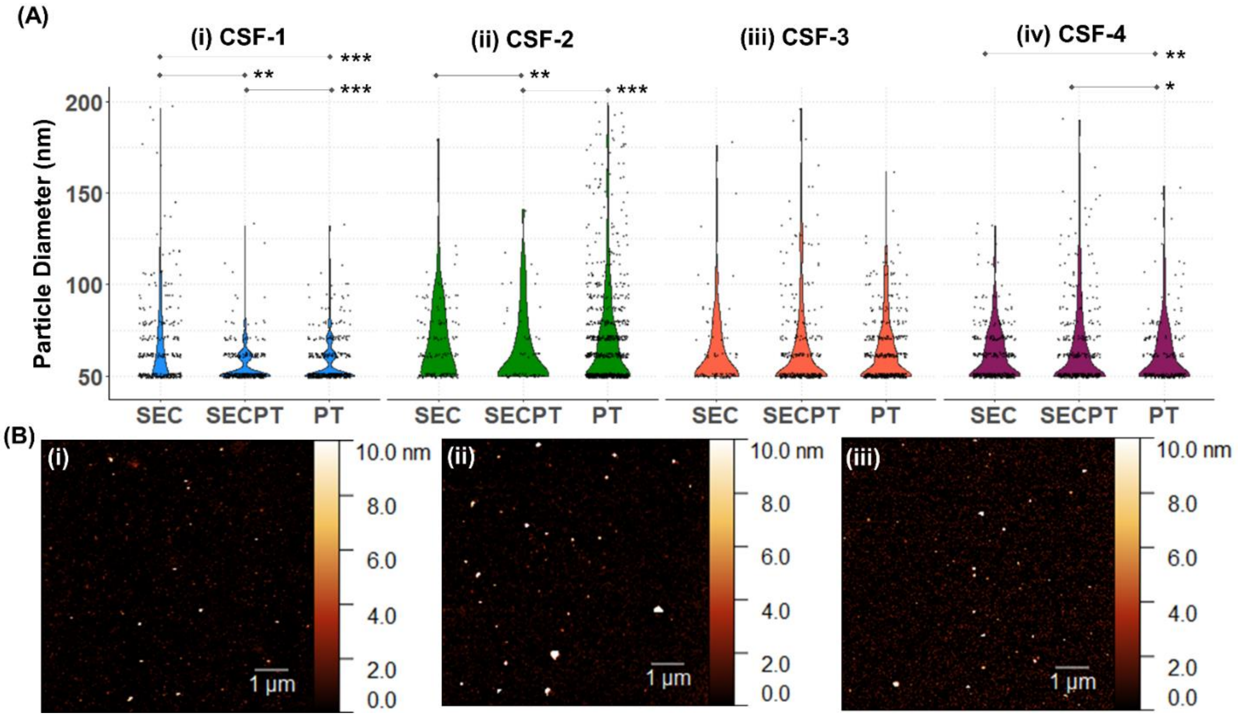

**Figure 2. AFM-based particle counts and sized distributions for CSF-derived sEVs.** Particle size distributions (A) for particles isolated from four patient CSF samples (i-iv) using SEC, the combination SECPT method, and PT alone, and (B) representative wide field images for (i) SEC (ii) SECPT and (iii) PT are shown. Particle counts and size distributions are obtained from AFM images using grain analysis function on 8 µm × 8 µm height images obtained at a resolution of 256 samples per line, at 0.75 Hz. Significant differences in the size distributions are marked with asterisks: * for $p < 0.05$, ** for $p < 0.01$, *** for $p < 0.001$, as determined by one-way ANOVA followed by Tukey's post-hoc test.

Of the three isolation methods used, SECPT produced higher particle counts for CSF-1, CSF-3, and CSF-4 compared to SEC alone, but did not demonstrate the expected 25-fold increase in concentration. Consistent with previous results, PT isolations alone produced the highest particle counts for three CSF samples, but also contained particle aggregates and co-isolated non-sEV particles. CSF-1, collected from a patient with GBM leptomeningeal spread, showed the highest particle counts across the three isolation methods. CSF-4, collected from a patient with metastatic cervical cancer, showed the second highest particle counts across the three isolation methods. For CSF-1 and CSF-2, SECPT produced a statistically significant smaller size distribution than SEC alone, but SECPT did not produce a significantly significant change in size distribution for

CSF-3 and CSF-4. When comparing SECPT isolates to PT isolates, CSF-1 and CSF-2 showed a statistically significant increase in size, while the CSF-4 SECPT isolate was smaller than the SEC isolate. None of the CSF-3 isolates showed statistically significant differences in size distribution between each other.

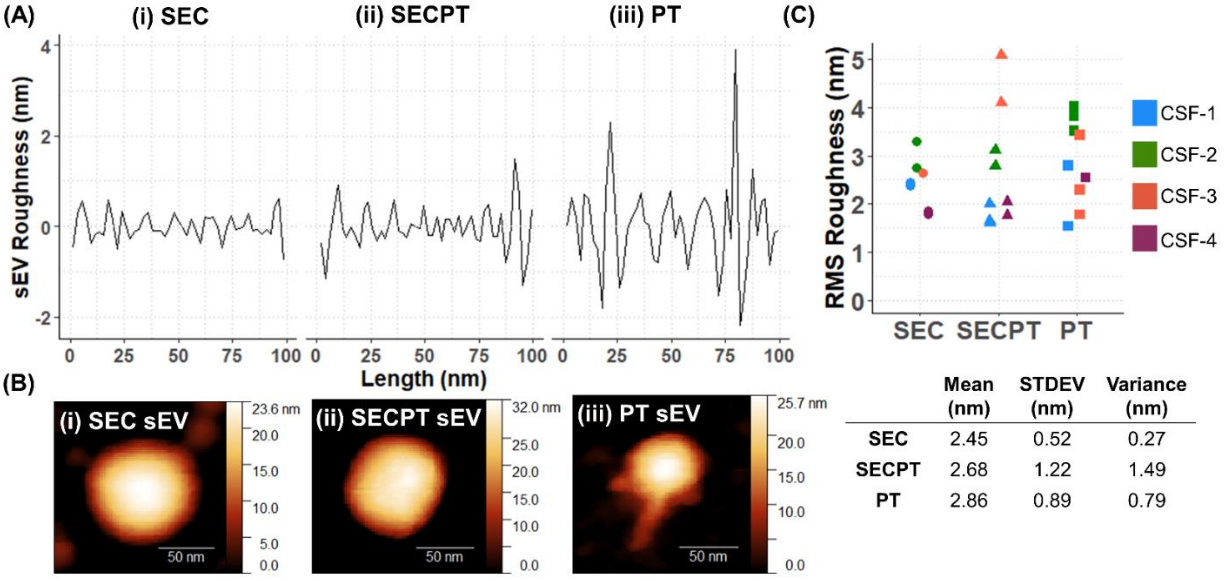

| | Mean (nm) | STDEV (nm) | Variance (nm) |
|---|---|---|---|
| **SEC** | 2.45 | 0.52 | 0.27 |
| **SECPT** | 2.68 | 1.22 | 1.49 |
| **PT** | 2.86 | 0.89 | 0.79 |

**Figure 3. Surface roughness of CSF sEVs.** (A) Linear roughness profiles and (B) representative height images for sEVs isolated using (i) SEC, (ii) SECPT, and (iii) PT. The PT sEV shows the greatest roughness profile, and polymeric matrix can be seen in the height image. The Young's modulus, localized surface modulus, and deformation channels can be found in Supplemental Figure S2. (C) RMS Roughness of sEVs from all four patient samples. SECPT and PT-isolated sEVs show a wider distribution of roughness than SEC isolated sEVs

Next, we examined the impact of isolation method on the surface roughness and elastic modulus of single sEVs (**Figure 3**). Line roughness profiles of single sEVs shows high roughness for PT sEVs compared to SEC and SECPT sEVs, and representative topography images **(Figure 3B)** show a representative PT sEV with attached polymeric matrix compared to round SEC and SECPT sEVs with no structural irregularities. Across the four CSF samples probed, PT isolates showed the highest RMS roughness (**Figure 3C)**, though SECPT sEVs showed the highest variance in RMS Roughness. The obtained surface roughness values for PT isolates are consistent with previous work which has shown that the PT method produces sEVs with higher surface roughness[12] than other methods. With regards to the localized surface modulus and Young's modulus (**Table 1**), all sEV isolates except the CSF-2-SEC isolate showed higher Young's modulus (deeper indentation) than localized surface modulus (small indentation), likely due to increased substrate effects at deeper indentations.[19] SECPT isolates from CSF-1, CSF-2, and CSF-4 demonstrated higher localized surface modulus and Young's modulus than corresponding SEC isolates, indicating that the combination method stiffens sEV nanoscale surface structure.

### 6.4 Conclusions

In conclusion, our study on nanoscale EV structural-mechanical analysis in CSF samples highlights the novel potential implications for AFM technology in improved isolation, quantification and single vesicle characterization of CSF EVs for GBM (and other brain-associated) biomarkers. An important obstacle to overcome prior to the widespread adoption of CSF EVs for disease monitoring or diagnosis is the limited sample volume and low abundance of EVs in CSF. Sample pooling or dilution is inappropriate for many applications, averages the variability between samples, eliminating the range and outliers, and may mask problems related to the performance of an assay. Our results demonstrate the ability of AFM to successfully elucidate sEV nano-metrics in CSF using minimal sample volume without the need to pool samples. Though the primary focus of this work has been single EV characterization of CSF derived sEVs, we also considered isolation methods performance characterization necessary to support novel uses for future EV analysis. We found that while the combination SECPT method increases the particle count of CSF sEV isolates, the elastic modulus of sEVs increased in SECPT isolates compared to SEC alone. Robust characterization of EVs serves as the foundation for any downstream applications: single EV-based analysis to quantify isolation method dependent nanoscale surface structure effects as shown here, combined with biochemical analysis, will be critical to develop “gold standard” protocols for isolation of EVs from single patient CSF samples.

## 6.5 Methods

***Human CSF Samples:*** CSF samples were obtained from four patients undergoing lumber puncture or shunt at UCLA Medical Centre. Written informed consents were obtained from all subjects as per UCLA IRB approved study protocol (IRB#10-000655). The 1 mL volume samples were centrifuged at 10,000 g for 30 mins at 4°C to remove microvesicles and cell debris. The supernatant was collected and frozen at −80˚C until use. CSF samples were tested for the presence of blood and other test parameters including pH, protein content, and pH using Multistix 10 SG Test Strips (Siemens, PA, USA). 10 microliters CSF were placed on each spot, and test parameters were visually quantified according to manufacturer guidelines, and compared to a quality control strip using 10 microliters PBS per spot.

***EV isolations:*** EVs were isolated using multiple techniques as outlined in **Supplemental Figure S1.** Size exclusion chromatography (SEC) based EV isolation was performed using Izon qEV Original (35 nm resin pore) size exclusion chromatography column according to manufacturer guidelines. Briefly, after flushing the column with 0.22 micron filtered PBS, 500 microliters pre-centrifuged CSF was placed on the column. 1.5 mL EV-containing solution was collected and stored at 4°C and analyzed within a week. Additionally, we employed a combination of size exclusion followed by precipitation (celled SECPT) isolation of EVs. SEC-isolated EV-containing solution was collected as above and concentrated using PEG precipitation methods as previously described.[12] Briefly, 1.5 mL EV-containing solution was combined with 300 microliters ExoQuick-TC solution (System Biosciences, CA) in sterile Eppendorf tubes, mixed by inversion, and incubated at 4°C for 18 hrs. The solution was centrifuged at *1,500g* for 30 minutes in an Eppendorf Minispin (Eppendorf, Germany). The resulting pellet was resuspended in 60 microliters PBS and stored at 4°C. To compare the effectiveness of additional precipitation step in concentrating EVs without affecting their structure and other biophysical characteristics, we compared SECPT to SEC and PT only isolates within the same CSF samples.

***Atomic Force Microscopy (AFM) based particle counts, size distribution, and single particle biomechanical analysis:*** 20 µL of isolated EV samples were incubated over (3-Aminopropyl) triethoxysilane (AP)-modified mica substrates (Ted Pella Inc, CA) for 3 min. To remove unbound EVs, substrates were washed twice with 50 µL PBS and imaging in PBS at room temperature. Measurements were conducted in PBS using a Dimension FastScan Microscope (Bruker Instruments, Santa Barbara, CA) in off-resonance tapping mode, with ScanAsyst Fluid tips (Bruker, CA) with radius ~20 nm and experimentally determined spring constants of 0.7 N/m. AFM images were taken at 256 samples per line, at 0.75 Hz, at optimal force setpoints of 1.25 nN and 2 nN. Images were exported offline and processed using Gwyddion or custom R software. Images were flattened with a second-order polynomial for the height channel, and a first-order polynomial for the Young's modulus, and deformation channels as described previously.[19] EV cross-sections were taken horizontally across the middle of the EV images using x, y coordinates to align cross-sections across all channels. The Young's modulus and localized surface modulus distributions were obtained from 20 pixel by 20-pixel area (~1500 nm$^2$) at the apical region of the EVs, using XY coordinates to align the covered area across all channels. RMS roughness was calculated over the same 20 pixels by 20 pixel area of the height channel using the Statistical Quantities Tool in Gwyddion.

***Statistical Analysis:*** Data were expressed as mean values ± standard deviations. Their statistical significance was identified by the Student's t-test or one-way analysis of variance (ANOVA), followed by Tukey's post-hoc test using the rstatix package in R for the differences among different CSF patient samples and between isolation methods. P value of less than 0.05 was considered to be statistically significant.

## 6.6 Supplemental Information

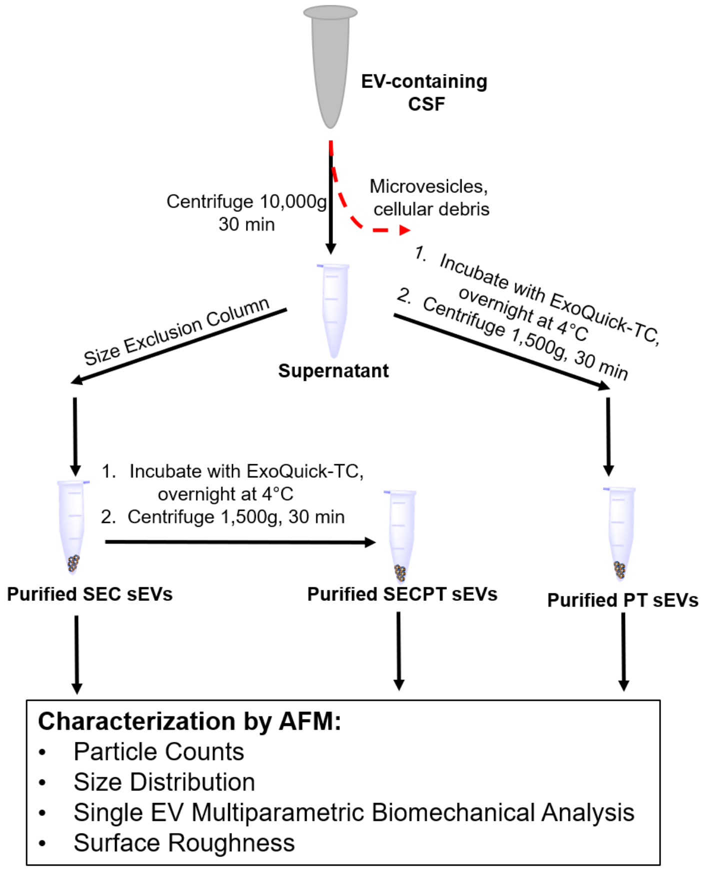

**Supplemental Figure S1. Isolation of sEVs from CSF.** Initially, CSF is cleared of microvesicles and cellular debris by centrifugation. The cleared supernatant is then run through a size exclusion column according to manufacturer guidelines to isolate purified CSF-SEC sEVs. CSF-SEC sEVs are concentrated by incubation with ExoQuick-TC solution to isolate CSF-SECPT sEVs. Cleared supernatant incubated with ExoQuick-TC to produce purified CSF-PT sEVs serves as a control. sEVs from all methods were characterized by AFM to quantify particle counts, size distribution, surface roughness, and biomechanical properties, namely Young's modulus, deformation, and localized surface Young's modulus.

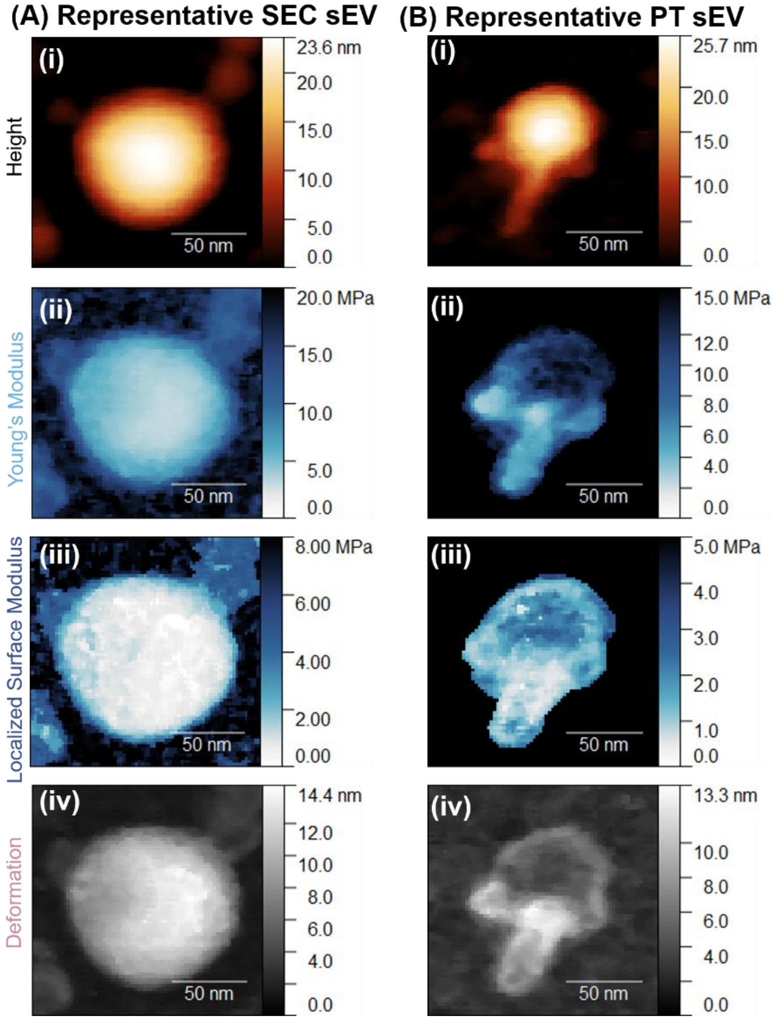

**Supplemental Figure S2. Representative maps of EVs derived from CSF patient samples** isolated using (A) SEC and (B) PT for (i) height, (ii) localized surface modulus, (iii) Young's modulus and (iv) deformation. The SEC-isolated sEV is round, and relatively flat, with uniform Young's modulus and localized surface modulus across the surface. The PT-isolated sEV has a filament, likely residual polymeric matrix, attached to it. The filament shows lower Young's modulus and localized surface modulus and higher deformation than the main body of the sEV.

## 6.7 References

1. Verma N, Cowperthwaite MC, Burnett MG, Markey MK. Differentiating tumor recurrence from treatment necrosis: a review of neuro-oncologic imaging strategies. Neuro Oncol. 2013 May;15(5):515–534. PMCID: PMC3635510

2. Shankar GM, Balaj L, Stott SL, Nahed B, Carter BS. Liquid biopsy for brain tumors. Expert Rev Mol Diagn. 2017 Oct;17(10):943–947. PMCID: PMC5856481
3. Théry C. Exosomes: secreted vesicles and intercellular communications. F1000 Biol Rep. 2011 Jul 1;3. PMCID: PMC3155154
4. Théry C, Zitvogel L, Amigorena S. Exosomes: composition, biogenesis and function. Nat Rev Immunol. 2002 Aug;2(8):569–579. PMID: 12154376
5. Colombo M, Raposo G, Théry C. Biogenesis, Secretion, and Intercellular Interactions of Exosomes and Other Extracellular Vesicles. Annu Rev Cell Dev Biol. Annual Reviews; 2014 Oct 6;30(1):255–289. PMID: 25288114
6. Xu R, Greening DW, Zhu H-J, Takahashi N, Simpson RJ. Extracellular vesicle isolation and characterization: toward clinical application. J Clin Invest. American Society for Clinical Investigation; 2016 Apr 1;126(4):1152–1162. PMID: 0
7. Al-Nedawi K, Meehan B, Micallef J, Lhotak V, May L, Guha A, Rak J. Intercellular transfer of the oncogenic receptor EGFRvIII by microvesicles derived from tumour cells. Nat Cell Biol. 2008 May;10(5):619–624. PMID: 18425114
8. Graner MW, Alzate O, Dechkovskaia AM, Keene JD, Sampson JH, Mitchell DA, Bigner DD. Proteomic and immunologic analyses of brain tumor exosomes. FASEB J. 2009 May;23(5):1541–1557. PMCID: PMC2669426
9. Sharma S, Gimzewski J. The Quest for Characterizing Exosomes: Circulating Nano-Sized Vesicles. Journal of Nanomedicine & Nanotechnology. 2012 Oct 1;03.
10. André-Grégoire G, Gavard J. Spitting out the demons: Extracellular vesicles in glioblastoma. Cell Adh Migr. 2016 Oct 13;11(2):164–172. PMCID: PMC5351723
11. Woo J, Sharma S, Gimzewski J. The Role of Isolation Methods on a Nanoscale Surface Structure and its Effect on the Size of Exosomes. J Circ Biomark. 2016 Jan 1;5:11–11. PMID: 28936259

12. Sharma S, LeClaire M, Wohlschlegel J, Gimzewski J. Impact of isolation methods on the biophysical heterogeneity of single extracellular vesicles. Scientific Reports. Nature Publishing Group; 2020 Aug 7;10(1):13327. PMCID: PMC7414114
13. Kupcova Skalnikova H, Bohuslavova B, Turnovcova K, Juhasova J, Juhas S, Rodinova M, Vodicka P. Isolation and Characterization of Small Extracellular Vesicles from Porcine Blood Plasma, Cerebrospinal Fluid, and Seminal Plasma. Proteomes. 2019 Apr 25;7(2):17. PMCID: PMC6630935
14. Sidhom K, Obi PO, Saleem A. A Review of Exosomal Isolation Methods: Is Size Exclusion Chromatography the Best Option? International Journal of Molecular Sciences. Multidisciplinary Digital Publishing Institute; 2020 Jan;21(18):6466.
15. Li M, Huang L, Chen J, Ni F, Zhang Y, Liu F. Isolation of Exosome Nanoparticles from Human Cerebrospinal Fluid for Proteomic Analysis. ACS Appl Nano Mater. American Chemical Society; 2021 Apr 23;4(4):3351–3359.
16. Binnig G, Quate CF, Gerber Ch. Atomic Force Microscope. Phys Rev Lett. American Physical Society; 1986 Mar 3;56(9):930–933. PMID: 10033323
17. Sharma S, LeClaire M, Gimzewski JK. Ascent of atomic force microscopy as a nanoanalytical tool for exosomes and other extracellular vesicles. Nanotechnology. IOP Publishing; 2018 Feb;29(13):132001. PMID: 29376505
18. Sharma S, Rasool HI, Palanisamy V, Mathisen C, Schmidt M, Wong DT, Gimzewski JK. Structural-Mechanical Characterization of Nanoparticle Exosomes in Human Saliva, Using Correlative AFM, FESEM, and Force Spectroscopy. ACS Nano. 2010 Apr 27;4(4):1921–1926. PMID: 20218655
19. LeClaire M, Gimzewski J, Sharma S. A review of the biomechanical properties of single extracellular vesicles. Nano Select. 2021;2(1):1–15.

# Chapter 7. Single Cell Mechanotype and Associated Molecular Changes in Urothelial Cell Transformation and Progression

## 7.1 Abstract

Cancer cell mechanotype changes are newly recognized cancer phenotypic events, whereas metastatic cancer cells show decreased cell stiffness and increased deformability relative to normal cells. To further examine how cell mechanotype changes in early stages of cancer transformation and progression, an *in vitro* multi-step human urothelial cell carcinogenic model was used to measure cellular Young's modulus, deformability, and transit time using single-cell atomic force microscopy, microfluidic-based deformability cytometry, and quantitative deformability cytometry, respectively. Measurable cell mechanotype changes of stiffness, deformability, and cell transit time occur early in the transformation process. As cells progress from normal, to preinvasive, to invasive cells, Young's modulus of stiffness decreases and deformability increases gradually. These changes were confirmed in three-dimensional cultured microtumor masses and urine exfoliated cells directly from patients. Using gene screening and proteomics approaches, we found that the main molecular pathway implicated in cell mechanotype changes appears to be epithelial to mesenchymal transition.

## 7.2 Introduction

Urothelial carcinoma (UC) of bladder is the fifth most common cancer in the United States.[1] Because of the high rate of disease recurrence and progression, lifelong continued monitoring is an essential part of management, which places a heavy burden on patients and healthcare services.[2] Urine cytology is the most accessible method to examine potential UC cells. Morphologically, malignant cells present increased nuclear-to-cytoplasmic (N/C) ratio and abnormal nuclear architecture, which provides the basis of cytology diagnosis. However, relying on morphology alone has many limitations. Some high-grade carcinoma cells also have abundant cytoplasm.[3] Benign reactive urothelial cells, tissue cluster, viral effect, post-treatment effect, and inflammation could increase the ambiguity and subjectivity. In addition, although in cystoscopy, high-grade invasive carcinoma often appears with large or multiple lesions, there is no specific morphological or molecular features for distinguishing invasive lesions from non-invasive tumors. This has a major clinical implication as invasive tumors, especially muscle invasive tumors, typically require aggressive treatment including radical cystectomy.

Genetically, urothelial bladder cancer has a remarkable propensity for divergent differentiation in association with advanced disease and aggressive behavior and demonstrates heavy mutational burden with an extensive heterogeneity in carcinogenesis.[4] These changes can be traced for developing molecular diagnostic biomarkers. Currently, FDA has approved NMP22, NMP22 BladderChek, and UroVysion urine assay for bladder cancer diagnosis and surveillance, and immunocytology (uCyt+), BTA-TRAK, and BTA-STAT for surveillance.[5] Studies have shown that single or combined molecular tests improve overall sensitivity of cytology to more than 70%.[6,7] Other DNA-based tests, including Telomerase reverse transcriptase (TERT) mutation assay, DNA methylation, microRNA, and transcriptomic biomarkers exhibited varied sensitivity between 50 and 80%.[8,9] However, tumor heterogeneity constitutes a main hurdle to the development of robust molecular biomarkers for bladder cancer.[10] It is still ambitious to capture the whole complex molecular heterogeneity landscape at cell level for the distinguishing of different malignant stages.

Indeed, the hallmark, and probably the deadliest aspect of cancer, is the invasive and metastatic nature of the disease. Cancer cell invasive and metastatic behaviors are likely the result of altered molecular, biochemical, and biophysical properties that are brought by the complex interplay of activation/inactivation of multiple signaling pathways regulating these cellular events. Recent emerging evidence has indicated that cellular mechanical properties, or mechanotype, is directly relevant to cell malignant phenotype, especially invasion, and metastasis. Our previous study showed that metastatic cancer cells from patients with various types of cancers (lung, breast, and pancreas) are less stiff than benign reactive mesothelial cells from human pleural fluid samples based on Young's modulus of elasticity determined by atomic force microscopy (AFM).[11] The reactive mesothelial cells and metastatic cancer cells often share very similar morphological features, creating difficulties in routine clinical diagnosis. Further studies showed that AFM measurements could be used to predict the response of tumor cells to the treatment of therapeutic drugs.[12–15] In addition, the cancer cell mechanotype evaluated by quantitative deformability cytometry (q-DC) can also be used to predict their invasion across breast and ovarian cancer cell lines.[16] Using microfluidic inertial focusing, hydrodynamic stretching, and high-speed image analysis, we have also demonstrated that cell deformability (i.e., the ability to change shape under load) provides a quantitative marker for objective algorithmic-based diagnoses of malignant pleural effusion cells.[17,18] Measurements of circulating tumor cells using this technique also revealed a more deformable phenotype than other large cells present in blood.[19] UC of the bladder has a well-defined multi-step nature of development. Urinary exfoliated cells, derived from primary UC tumors, provide a unique living model for the study of UC. However, the cell mechanotype changes of UC cells and urinary exfoliated cells have not previously been systematically studied.

In the present study, we characterized the changes in cellular mechanotype in a well-established multi-step urothelial cancer progression model and clinical urinary specimens using an array of techniques including single cell AFM indentation method, microfluidic-based deformability cytometry (DC) analysis, and q-DC analysis. Gene expression and proteomics analysis were performed to investigate the underlying molecular events associated with malignant phenotype and cell mechanotype changes.

## 7.3 Materials and Methods

### *Cell Culture*

A human UC *in vitro* model included HUC-BC, HUC-PC, and MCT-11 cell lines were from the Pathology and Laboratory Medicine Department at the University of California, Los Angeles (UCLA).[20,21] Cells were grown in Dulbecco's Modified Eagle's Medium (DMEM) containing 10% (v/v) fetal bovine serum (FBS) and 1% (v/v) streptomycin/penicillin (S/P), and maintained at 37.0°C with 5% $CO_2$. Medium was replaced every 2–3 days depending on cell density. For three-dimensional (3D) cell culture, $2 \times 10^3$ cells in a 200 µL DMEM containing 10% FBS were seeded in 96-well spheroid microplates (corning). The plate was incubated for 48 h at 37°C, 5% $CO_2$ to allow the formation of cell spheroid. Cultured HUC-BC, HUC-PC, and MCT-11 cells in 50% confluency were treated with 200 µM 4-ABP or 60 µg/mL GTE (both from Sigma-Aldrich), which were determined by cell proliferation assay. Cells were exposed for 48 h prior to harvesting for mechanotype analysis.

### *Cell ImageStream Morphology Analysis*

We used the ImageStreamx MarkII imaging flow cytometer to discriminate subtle morphologic or signal distribution changes within cell populations. Treated and untreated HUC cell suspensions with a concentration of $2 \times 10^7$ cells/mL in PBS/2%FBS were labeled with Texas red and DAPI. For each cell, a side-scatter (darkfield) image, a transmitted light (brightfield) image, and two fluorescence images of G-actin and nuclear DNA were acquired to analyze the changes of cell diameter and nuclear area.

### *Urinary Specimen Collection and Processing*

Urinary exfoliated cells were collected from a 20 mL urinary specimen after centrifugation and then attached on slides through cytospinning at 100 rpm for 5 min. We previously used short-term *ex vivo* culture to allow cell attachment,[11] but the culturing step is time consuming and introduces artifacts. The cytospin method is fast and preserves the morphology of urine cells well, which has been verified in our laboratory. Cytospun cells were covered with DMEM/F-12 medium, scanned under 200X microscope field, and measured Young's modulus on uroepithelial cells, which can be distinguished from squamous epithelial cells and cells of hematologic origin.

### *Analysis of Cell Young's Modulus Using AFM*

Treated and untreated HUC-BC, HUC-PC, and MCT-11 cells ($1 \times 10^5$ cell/mL) were seeded in 60 × 15 mm petri dishes. AFM measurement was performed when cells completely attached on the surface using a Catalyst Bioscope (Bruker) with a combined inverted optical/confocal microscope (Zeiss). This combination permits lateral positioning of the AFM tip over the nuclear region of the cell with micrometer to nanometer precision. Mechanical measurements were carried out at 37°C using silicon nitride cantilevers with experimentally determined spring constants. Force–displacement curves were recorded at 1 KHz for determination of Young's modulus. The modulus was calculated by converting the force curves into force–indentation curves and fitting with the Hertz–Sneddon model, which describes the indentation of an elastic sample using a stiff conical indenter on cell nuclear area. To prevent damage to the cell surface and to reduce any possible substrate-induced effects, measurements were performed in force ranges resulting in shallow indentations of the cell (< 400 nm). We measured about 15 cells in each sample. Data were plotted as histograms of Young's modulus (E, KPa) vs. relative frequency for each measured sample.

### *Analysis of Cell Deformability Using DC*

Treated and untreated HUC-BC, HUC-PC, and MCT-11 were detached and suspended at $1 \times 10^5$ cells/mL for DC measurement. Microfluidic devices were fabricated using standard photolithographic methods and polydimethylsiloxane (PDMS) replica molding techniques. Cell suspensions were pumped through PEEK tubing inserted into the DC microfluidic chip by a syringe pump with a volumetric flow rate ranging from 700 to 1,075 µL/min to test various stresses on cell response. High-speed (350,000 frames/s) video was acquired, and an automated image analysis algorithm was used to extract cell size and shape metrics. Automated image analysis software was used to extract a host of independent physical parameters from these images. The software stores and graphs strain metrics (deformability = a/b, where a is the long axis dimension of the cell and b is the short axis) properties of 1,000 of cells in a density scatter plot format.

### *Analysis of Cell Transit Time Using q-DC*

Monolayer cells in culture were detached and suspended at 1 × $10^5$ cells/mL for q-DC experiment. Q-DC microfluidic devices were mounted onto an inverted microscope (Zeiss Observer, Zeiss, Oberkochen, Germany) that was equipped with a 20/0.40 NA objective. Cell suspensions were driven by a constant air pressure (69 kPa) to flow through the channels. As cells deformed through microfluidic constrictions with 7 µm height and 7 µm width, a CMOS camera (MicroRNAcoEx4, Vision Research, Wayne, NJ, United States) was used to capture brightfield images at rates of 600–2,000 frames per second. Using custom software[1] (MATLAB), we analyzed the displacements of single cells through the microfluidic channel and extracted transit time based on the time a cell entered and exited a constriction.[22]

### *Gene Expression Analysis*

Total RNA was extracted from treated and untreated cells using a TRIzol reagent (Thermo Fisher Scientific, United States). The RNA samples were then applied to a RNeasy Mini spin column for purification (RNeasy Miniprep Kit, Qiagen). Global gene expression profiles of the cells were generated using the Affymetrix GeneChip Human Transcriptome Array (HTA) 2.0 system. An Affymetrix WT PLUS Reagent Kit was used to prepare the RNA for hybridization to the HTA. Data analysis was performed using the Affymetrix Expression Console software and Transcriptome

Analysis Console software. Ingenuity Pathway Analysis (IPA) was followed to compare the changes in gene expression in different signaling pathways.

### *Quantitative Analysis of Protein Level of Urothelial Cells by Mass Spectrometry*

Peptide sample preparation, LC-MS acquisition, and analysis were carried out at the UCLA Proteome Research Center. Briefly, protein aliquots (50 μg) were reduced and alkylated via sequential incubations of 5 mM tris(2-carboxyethyl)phosphine hydrochloride and 10 mM iodoacetamide at room temperature, allowed to bound to beads after the addition of 10 μL of carboxylate-modified magnetic beads,[23] and then digested by sequential addition of lys-C and trypsin proteases. Peptide samples were separated on a 75 μm i.d., 25 cm C18 column packed with 1.9 μm C18 particles (Dr. Maisch GmbH HPLC) using a gradient of increasing acetonitrile concentration and injected into an Orbitrap-Fusion Lumos Tribrid mass spectrometer (Thermo Fisher Scientific, United States), on which MS/MS spectra were acquired by Data Dependent Acquisition (DDA) mode. Database searching was performed using the MaxQuant (1.6.10.43) against the human reference proteome from EMBL (UP000005640_9606 HUMAN Homo sapiens, 20,874 entries). The search included carbamidomethylation on cysteine as a fixed modification and methionine oxidation and N-terminal acetylation as variable modifications. The digestion mode was set to trypsin and allowed a maximum of two missed cleavages. The precursor mass tolerances were to 20 and 4.5 ppm for the first and second searches, respectively, while a 20 ppm mass tolerance was used for fragment ions. Datasets were filtered at 1% FDR at both the PSM and protein-level. Peptide quantitation was performed using the MaxQuant's LFQ mode.

### *Immunohistochemical Staining Analysis*

Cells were harvested, washed, and then fixed to prepare for Immunohistochemical staining (IHC) analysis. Cells were placed on slides through the cytospin procedure. We used Citrate buffer PH

6.0 to perform antigen retrieval. The antibodies used were M0725 anti-vimentin IgG (Dako), and pan-cytokeratin (AE1/AE3) (Cell Marque) mouse monoclonal antibody with a concentration of 1/100. We incubated cell slides with the first antibody at 4°C overnight. Then second antibody incubation and DAB process were performed to develop stain color.

*Statistical Analysis*

Statistical analysis was performed using the SAS version 9.2 software (SAS Institute Inc., Cary, NC, United States). Continuous data were presented as means plus/minus the standard deviation (± SD) and compared with the Student's *t*-test and one-way analysis of variance. For cell transit time, we used the Mann-Whitney U test to determine statistical significance. Categorical variables were compared by the chi-square ($\chi^2$) test. Statistical significance was defined by a two-tailed *p*-value of $\leq 0.05$.

## 7.4 Results

### 7.4.1 Characterization of Urothelial Cell Mechanotype During Malignant Transformation and Progression Using AFM, DC, and q-DC

UC, like many other epithelial malignancies, typically follows a multi-step development and progression from normal to non-invasive *in situ* to invasive carcinoma.[24,25] To recapitulate the multi-step nature, we used a unique carcinogenic human urothelial carcinoma (HUC) model. The HUC model includes three cell lines. These cell lines, derived originally from the same progenitor cells, undergo different malignant transformation, and show distinct progression potentials in response to the treatment of carcinogen 4-aminobiphenyl (4-ABP).[20,21] The HUC-BC is untransformed cells and not tumorigenic (hence simulating "normal urothelial cells"), the HUC-PC exhibits non-invasive transformation phenotype (simulating "preinvasive" urothelial cells), and the MCT-11 is transformed carcinoma cells and exhibits typical invasive and aggressive phenotype.

To investigate the cellular mechanotype changes, three previously established platforms were used.[11,17,26] As shown in **Figure 1A** and **Figure 1B**, AFM characterizes elasticity, or stiffness, of living cells through measuring force–displacement as the tip is pushed toward the cell, indented into the sample, and subsequently retracted.[11] The stiffness of cells is quantified by the value of Young's modulus. From untransformed HUC-BC cells, HUC-PC cells to transformed MCT-11 cells, the stiffness gradually decreases (HUC-BC vs. HUC-PC, cell modulus: 19.5 ± 2.6 KPa vs. 11.2 ± 4.5 KPa, $P < 0.05$, *t*-test; HUC-BC vs. MCT-11, cell modulus: 19.5 ± 2.6 KPa vs. 6.7 ± 2.2 KPa, $P < 0.05$, *t*-test) (**Figure 1A**). The inversely related trend was observed in cell deformability measurement by DC in which a continuous stream of single cells is created, where each cell's deformation under a high-speed microfluidic flow is measured with high-speed imaging.[17] DC enables high-throughput single-cell mechanotyping. Cellullar deformation is induced by the shear and inertial stresses of fluid flow (**Figure 1D**). DC measurements show that in the order of HUC-BC, HUC-PC, and MCT-11 cells, deformability progressively increases (HUC-BC vs. HUC-PC, deformability: 1.35 ± 0.02 vs. 1.55 ± 0.04, $P < 0.05$, *t*-test; HUC-BC vs. MCY-11, deformability: 1.35 ± 0.02 vs. 1.65 ± 0.05, $P < 0.05$, *t*-test) (**Figure 1C**). To confirm this finding, we analyzed cellular deformability using another technique, q-DC.[26] By applying a pressure gradient across the microfluidic device, cells were driven to deform through micron-scale constrictions (**Figure 1F**). We tracked the time scale for single cells to transit through micron-scale gaps in the microfluidic channel; the resultant "transit time" reflects cell mechanotype, whereby stiffer cells and particles have a longer transit time.[22] In the pooled dataset that includes three replicates, HUC-PC and MCT-11 cells showed a statistically significant decrease in transit time compared to HUC-BC cells (HUC-BC vs. HUC-PC, median transit time: 25.6 vs. 20.0 ms, $P < 0.05$, U-test; HUC-BC vs. MCT-11, median transit time: 25.6 vs. 20.6 ms, $P < 0.05$, U-test), substantiating an increase in the compliance of highly malignant UC cells compared to the untransformed urothelial cells (**Figure 1E**). These results indicate that highly malignant carcinoma cells are less stiff and more deformable than untransformed cells.

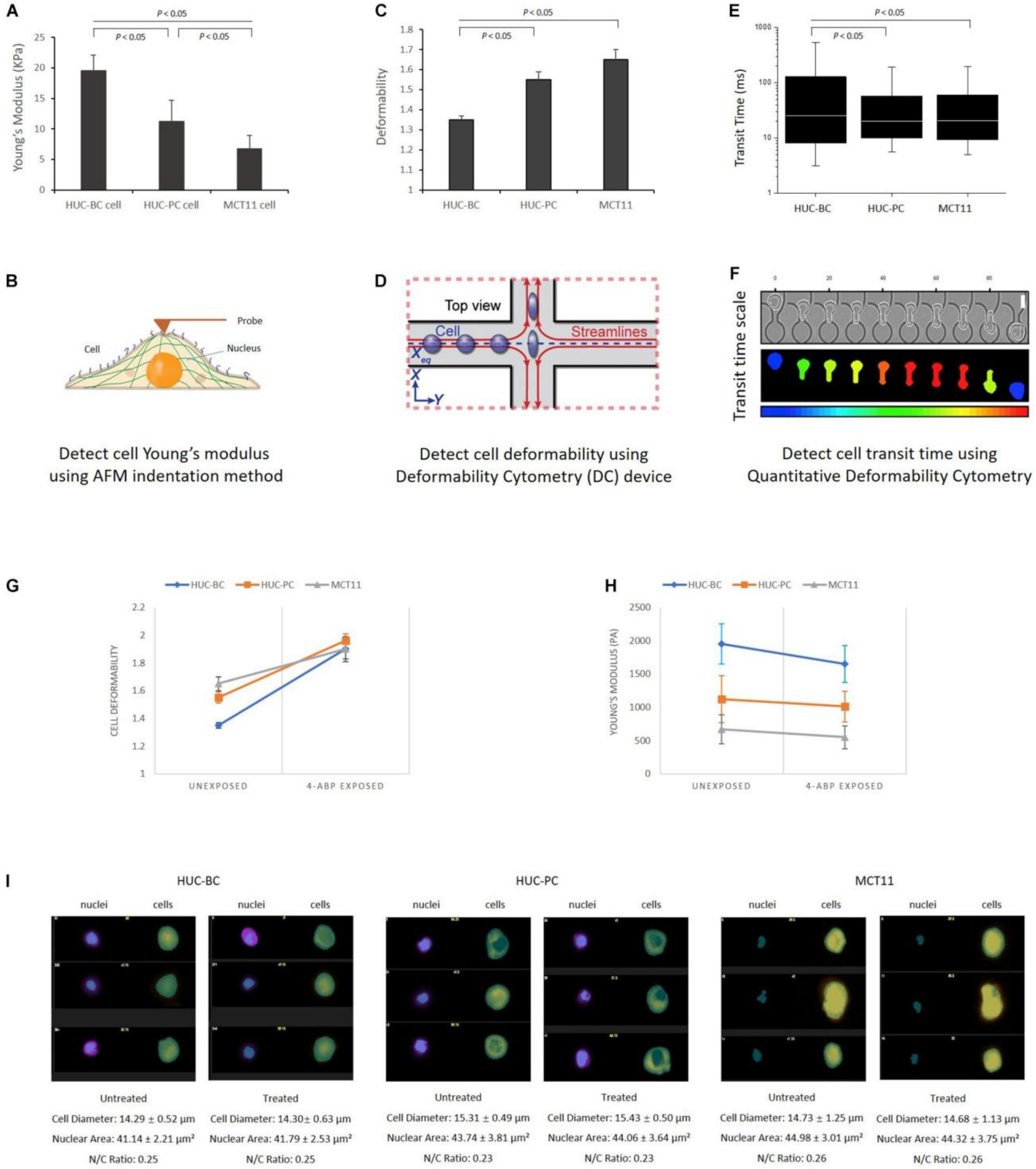

| Untreated | Treated | Untreated | Treated | Untreated | Treated |
|---|---|---|---|---|---|
| Cell Diameter: 14.29 ± 0.52 µm | Cell Diameter: 14.30± 0.63 µm | Cell Diameter: 15.31 ± 0.49 µm | Cell Diameter: 15.43 ± 0.50 µm | Cell Diameter: 14.73 ± 1.25 µm | Cell Diameter: 14.68 ± 1.13 µm |
| Nuclear Area: 41.14 ± 2.21 µm² | Nuclear Area: 41.79 ± 2.53 µm² | Nuclear Area: 43.74 ± 3.81 µm² | Nuclear Area: 44.06 ± 3.64 µm² | Nuclear Area: 44.98 ± 3.01 µm² | Nuclear Area: 44.32 ± 3.75 µm² |
| N/C Ratio: 0.25 | N/C Ratio: 0.25 | N/C Ratio: 0.23 | N/C Ratio: 0.23 | N/C Ratio: 0.26 | N/C Ratio: 0.26 |

**Figure 1. Characterization of urothelial cell mechanotypes using AFM, DC, and q-DC techniques.** (A,B) Young's Moduli of HUC-BC, HUC-PC, and MCT-11 cells were characterized by AFM. Force–displacement curves generated by probe over the nuclear region were recorded for determination of Young's moduli of HUC cells. (C,D) Deformability of HUC-BC, HUC-PC, and MCT-11 cells was analyzed using DC device. Cell deformation is induced by the shear stresses of fluid flow and captured by a high-speed imaging system. An automated image analysis algorithm was used to extract cell size and shape metrics. Cell maximum aspect ratio under compressive and shear forces was defined as deformability. (E,F) Transit time of HUC-BC, HUC-PC, and MCT-11 cells was analyzed using q-DC device. The displacements of single cells through the microfluidic channel were recorded. Transit time based on the time a cell entered and exited a constriction was extracted. (G,H) Decreased cellular Young's modulus and increased deformability were observed in HUC-BC, HUC-PC, and MCT-11 cells after 48 h carcinogen 4-ABP exposure through AFM and DC analysis. (I) Transmitted light (brightfield) image and nuclear images of HUC-BC, HUC-PC, and MCT-11 cells are shown by the ImageStream flow cytometry. Cell sizes, nuclear areas, and cell/nucleus ratio between exposed and unexposed cells were quantified. AFM, atomic force microscope; DC, deformability cytometry; q-DC, quantitative deformability cytometry; HUC, human urothelial carcinoma.

### 7.4.2 Decreased Stiffness in HUC Cells From 3D Cultured Microtumor Mass and From Patient Urinary Cytology Specimens

To better mimic *in vivo* tumor growth, we used a scaffold-free spheroid cell culture condition to grow bladder cancer cells as micro tumor masses (**Figure 2A**). Prior to AFM measurement, cells were dissociated from tumor masses and placed on the slides after cytospin (**Figure 2B**). Again, we observed that untransformed HUC-BC cells display significantly higher stiffness than HUC-PC and MCT-11 cells (**Figure 2C**).

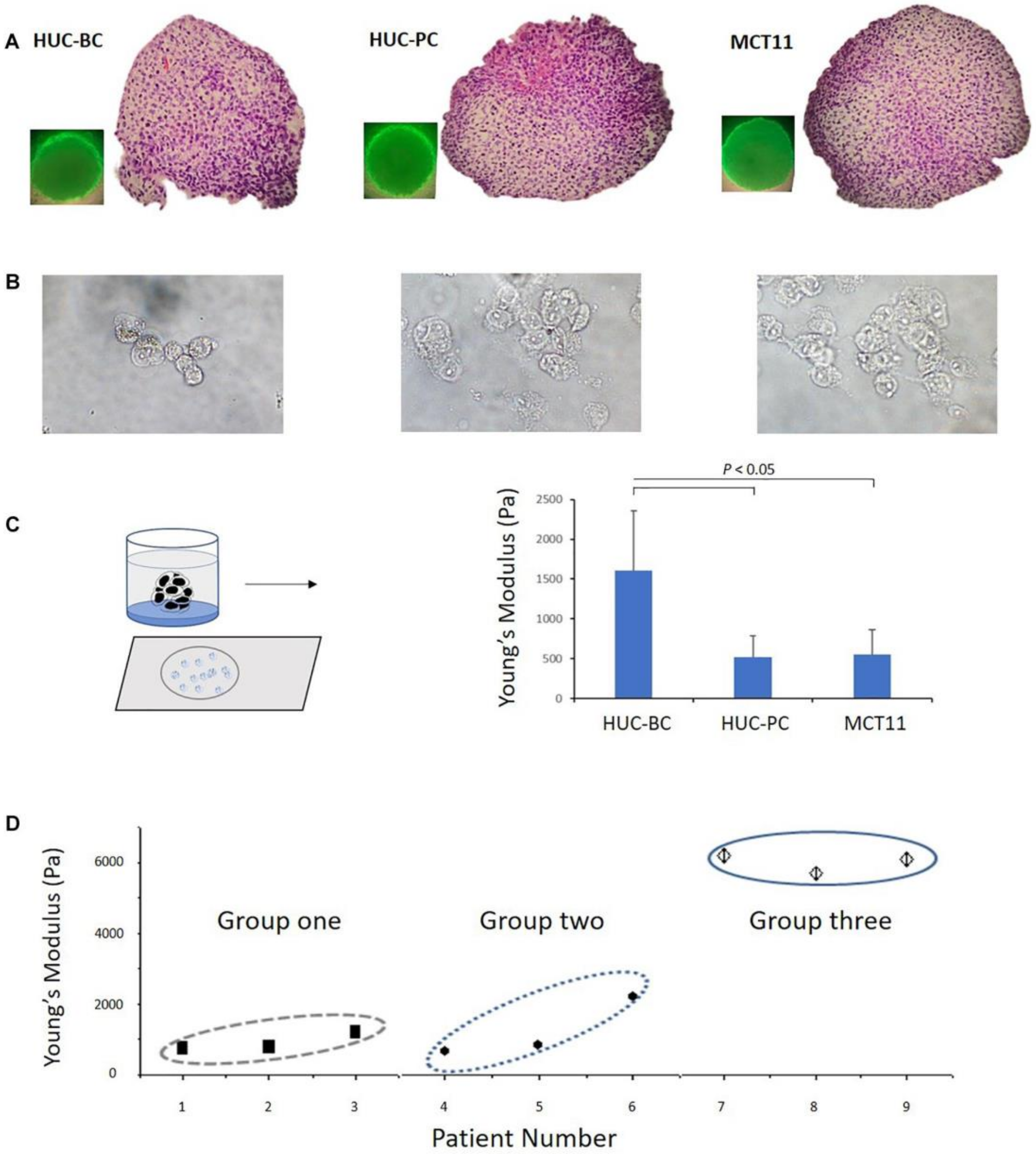

**Figure 2. Change in Young's modulus of cells from 3D cultured microtumor masses and from patient urinary cytology specimens.** (A) A 3D cell culture condition was used to grow HUC-BC, HUC-PC, MCT-11 cells as micro tumor masses. Spheroid formations of HUC cells were shown over 72 h after seeding. HE stains demonstrate dense, rapid-growing cell masses. (B) Dissociated HUC-BC, HUC-PC, and MCT-11 cells were under AFM measuring. (C) Untransformed HUC-BC cells display significant higher cellular Young's modulus than HUC-PC and MCT-11 cells. (D) Pooled data analysis of Young's moduli of urinary exfoliated cells from nine urine cytology specimens. Group one included three cytology-positive specimens from patients with HGUC confirmed by cystoscopy biopsy diagnosis. Group two included thee cytology-atypical specimens from patients with HGUC confirmed by cystoscopy biopsy diagnosis. Group three included three cytology-negative specimens from patients with no UC. The number of measured uroepithelial cells in each case ranged from 3 to 10. The average number of force-displacement curve obtained from each cell was three. AFM, atomic force microscope; HUC, human urothelial carcinoma.

Based on our previously published methods,[11,17] we developed a practical protocol to prepare cells directly from urinary cytology specimens for mechanotype analyses described in the section “Materials and Methods”. Using this method, we tested nine clinical urinary specimens, which were divided into three groups. Group one and two included six specimens from patients with high-grade urothelial carcinoma (HGUC) confirmed by cystoscopy biopsy diagnosis. The three specimens of group one had positive cytology findings and the three specimens of group two had atypical cytology findings. Group three included another three from patients with no UC as confirmed by both cystoscopy and cytology examination. As shown in **Figure 2D**, a pooled data analysis demonstrated the same mechanotype change pattern as we observed in 3D cultured microtumor masses, where urinary exfoliated cells from group three had the highest Young’s modulus. While certainly more samples will be needed to be conclusive, the preliminary finding shows the feasibility of measuring single-cell mechanotype changes in clinical urinary samples.

### 7.4.3 Decreasing Stiffness and Increasing Deformability During Malignant Transformation and Progression Induced by 4-ABP

As shown in **Figure 2C**, the magnitude of difference between HUC-BC vs. HUC-PC and MCT-11 cells cultured from 3D condition appeared to be larger than the differences in cellular stiffness measured by AFM on 2D cultured cells. We suspected that in microtumor masses, HUC cells were grown without losing cell-cell interaction in all directions, central hypoxia, and cell response and resistance to the tumor microenvironment. The malignant potential can be fully expressed and captured by mechanotype analysis. Previously, it has been shown that upon exposure to carcinogen 4-ABP, the malignant phenotypes, namely the ability of cells to form tumor nodules upon injected to the nude mice, can be enhanced.[20,21] Thus, to further characterize the link between mechanotype change and urothelial transformation and progression, we exposed three cell lines to 4-ABP. After 48-h exposure, we quantified morphological changes of cells using the ImageStream flow cytometry analysis. No significant differences were observed in cell sizes, nuclear areas, and cell/nucleus ratio between treated and untreated cells (**Figure 1I**). However, decreased cell Young's modulus was observed in HUC-BC, HUC-PC, and MCT-11 cells through AFM measurement (**Figure 1H**). A similar trend in the changes of cell deformability was seen by DC, whereby all three cell lines displayed increased deformability compared to untreated controls (**Figure 1G**). Altogether, mechanotype characterization of the urothelial cells demonstrated specifically decreased cellular modulus and increased cell deformability as malignancy increases, indicating that changes in cellular mechanotype is associated with urothelial cell malignant transformation and progression.

### 7.4.4 Correlation of Activated Epithelial-Mesenchymal Transition Pathway With the Change of Cellular Mechanotype

To explore the underlying molecular events associated with these specific mechanotype changes, we screened the transcriptome of HUC-BC, HUC-PC, and MCT-11 cells. The 3D portrayal diagram (**Figure 3A**) demonstrates the differences in gene expression among the three cell lines and their carcinogen-induced counterparts. Using IPA, we identified the association of many differentially expressed genes with epithelial to mesenchymal transition (EMT). Compared to HUC-BC cells, HUC-PC, and MCT-11 cells have more than two-fold activation in the EMT pathway (activation *z* score: 2.319, $P < 0.001$) (**Figures 3B–D**). Upstream regulator analysis indicated several molecular signaling pathways, including ERK/MAPK, TGFβ, Integrin, Notch, and Wnt signaling, all of which are important contributors of the EMT pathway, were activated (**Figure 3E**). The EMT process was originally found in tissue repair and fibrosis, in which epithelial cells lose their junctions and apical-basal polarity and motile behavior as they differentiate into mesenchymal cells. Importantly, the EMT process involves gene expression reprogramming, signaling changes and cytoskeleton reorganization, and plays a pivotal role in malignancy progression.[27,28] Recent genome-wide characterization study on 112 bladder cancer cases revealed that highly malignant sarcomatoid urothelial bladder cancer is largely driven by dysregulation of the EMT network.[29] However, the evidence of a full EMT phenotype in clinical carcinomas and metastases is frequently questioned because EMT can be reversible and transient.[30] Also, the role of the EMT process as a driving force on cell mechanotype regulation is not clear. To confirm the change between activated EMT and decreased cell's modulus and increased deformability, we induced malignant progression on HUC-BC, HUC-PC, and MCT-11 cells with 4-ABP. As shown in **Figures 1G and 1H**, 4-ABP exposure reduced Young's modulus and increased deformability in all three cell lines, especially in HUC-BC and HUC-PC cells. We then performed an IPA canonical pathway analysis on differentially expressed genes. Again, activated EMT pathway was found in 4-ABP treated HUC-BC and HUC-PC cells in comparison to their untreated counterparts (HUC-BC vs. treated HUC-BC: Activation $z$ score: 0.1, $P < 0.001$; HUC-PC vs. treated HUC-PC: Activation $z$ score 0.08, $P < 0.001$). These results suggest that the EMT pathway may be correlated with mechanotype dynamics in urothelial cells.

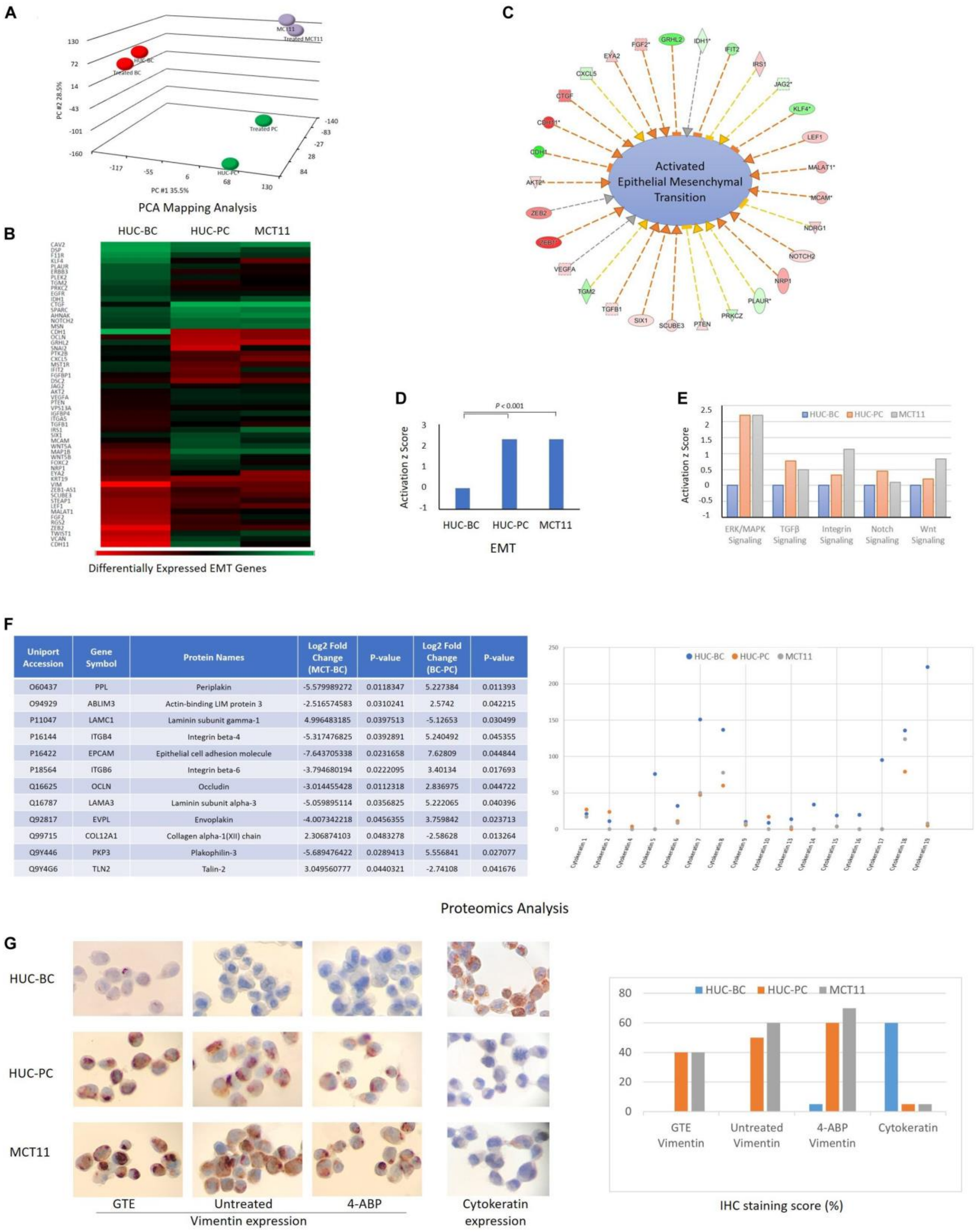

| Uniport Accession | Gene Symbol | Protein Names | Log2 Fold Change (MCT-BC) | P-value | Log2 Fold Change (BC-PC) | P-value |
|---|---|---|---|---|---|---|
| O60437 | PPL | Periplakin | -5.579989272 | 0.0118347 | 5.227384 | 0.011393 |
| O94929 | ABLIM3 | Actin-binding LIM protein 3 | -2.516574583 | 0.0310241 | 2.5742 | 0.042215 |
| P11047 | LAMC1 | Laminin subunit gamma-1 | 4.996483185 | 0.0397513 | -5.12653 | 0.030499 |
| P16144 | ITGB4 | Integrin beta-4 | -5.317476825 | 0.0392891 | 5.240492 | 0.045355 |
| P16422 | EPCAM | Epithelial cell adhesion molecule | -7.643705338 | 0.0231658 | 7.62809 | 0.044844 |
| P18564 | ITGB6 | Integrin beta-6 | -3.794680194 | 0.0222095 | 3.40134 | 0.017693 |
| Q16625 | OCLN | Occludin | -3.014455428 | 0.0112318 | 2.836975 | 0.044722 |
| Q16787 | LAMA3 | Laminin subunit alpha-3 | -5.059895114 | 0.0356825 | 5.222065 | 0.040396 |
| Q92817 | EVPL | Envoplakin | -4.007342218 | 0.0456355 | 3.759842 | 0.023713 |
| Q99715 | COL12A1 | Collagen alpha-1(XII) chain | 2.306874103 | 0.0483278 | -2.58628 | 0.013264 |
| Q9Y446 | PKP3 | Plakophilin-3 | -5.689476422 | 0.0289413 | 5.556841 | 0.027077 |
| Q9Y4G6 | TLN2 | Talin-2 | 3.049560777 | 0.0440321 | -2.74108 | 0.041676 |

**Figure 3. Molecular events associated with mechanotype changes of urothelial cells.** (A) PCA mapping analysis shows the differences in gene expression among HUC-BC,

HUC-PC, MCT-11 cells, and their 4-ABP exposed counterparts. (B–D) demonstrate the activated EMT process from HUC-BC, HUC-PC, to MCT-11 cells (IPA analysis). (E) Shows activated ERK/MAPK, TGFβ, Integrin, Notch, and Wnt signaling from HUC-BC, HUC-PC, to MCT-11 cells. (F) Proteomics analysis identifies differentially expressed proteins associated with cell mesenchymal and epithelial features. Protein markers that had more than twofold expression changes between MCT-11 and HUC-BC, and between HUC-BC and HUC-PC are listed in the right table. Individual cytokeratin expression is shown on the right. (G) Vimentin expression on untreated, GTE-treated, and 4-ABP-treated cells and pan-cytokeratin expression on HUC model cells are shown on IHC staining pictures. Staining score was reported as the ratio number of positively stained cells/total number of cells × 100. PCA, Principal component analysis; IPA, Ingenuity pathway analysis; GTE, green tea extract.

### 7.4.5 Identifying Protein Targets in Epithelial-Mesenchymal Transition Pathway Associated With Mechanotype Changes

We then interrogated the differences in protein content using the proteomics approach.[31] A number of differentially expressed proteins associated with EMT, including peiplakin, a component of desmosomes and of the epidermal cornified envelope in keratinocytes, E cadherin, an epithelial marker localized at cell–cell contacts, mesenchymal marker vimentin, fibronectin, and many other regulator proteins[32] were identified. The table of **Figure 3F** lists a few protein markers that had more than twofold expression changes between MCT-11 and HUC-BC, and between HUC-BC and HUC-PC. The change trends of both epithelial marks and mesenchymal markers demonstrated urothelial cells obtained mesenchymal features while losing epithelial makers with malignant progression, which is consistent with the results from gene expression analysis.

Cytokeratins are a class of intermediate filaments demonstrating epithelial differentiation. Individual cytokeratins are commonly used markers for determining the grade of bladder cancer cells.[33,34] As illustrated in **Figure 3F**, protein abundance of individual cytokeratins showed the expression of most cytokeratin family molecules decrease from HUC-BC, to HUC-PC, and MCT-11 cells. Among them, cytokeratin 5, 7, 17, and 19 have remarkable decreasing trend. This trend was confirmed by pan-cytokeratin IHC staining, where HUC-BC cells demonstrated significantly higher pan-cytokeratin expression than HUC-PC and MCT-11 cells (**Figure 3G**). On the other hand, vimentin, an EMT marker, is one of the intermediate filaments that mainly functions to maintain cell integrity and involved in the cell migration and invasion of metastasizing cancer cells.[35,36] Our previous study showed that ovarian cancer cells induced to have mesenchymal phenotype either by overexpression of EMT transcription factors (ZEB1, SNAI1, and SNAI2), oncogenes (H-Ras v12), or by drug resistance were all consistently more deformable than cells with epithelial phenotype.[37] In these processes, increased vimentin and reduced E-Cadherin were indicated. Over-expression of vimentin correlates with increased tumor growth and invasiveness, and as well as with poor clinical outcomes in several cancers.[38] Another study reported that intracellular mechanical homeostasis was interrupted in vimentin-knockdown breast cancer cells. Overexpressing vimentin in MCF7 breast cancer cells reoriented microtubule polarity, increased cell directional migration, and EMT phenotypes.[39] To confirm the upregulation of vimentin in UC cells, we performed an IHC analysis. HUC-BC cells have the lowest expression of vimentin whereas MCT-11 cells have the highest, in line with the activation status of EMT and urothelial cell mechanotype changes (**Figure 3G**). Previously, we also reported that chemopreventive agent green tea extract (GTE) modulated cytoskeletal actin remodeling via Rho activity in the same UC cells and significantly increased the stiffness of GTE-treated metastatic tumor cells compared to normal cells.[13,40] In the present study, we found that GTE counteracts the effect of carcinogen 4-ABP by reversing the increase in vimentin expression (**Figure 3G**), further corroborating epithelial-mesenchymal transition plays an important role in urothelial cell mechanotype changes.

## 7.5 Discussion

While metastatic tumor cells show a distinctive cell mechanotype relative to normal cells, the specific pattern of changes in cell mechanotype during the early stages of cancer transformation and progression is not well studied. Identifying metastatic cancer cells may be clinically too late to save patients' lives. Therefore, there is a great need for developing biomarkers that can be used to determine the invasive and metastatic potential of malignant cells before the invasion or metastasis actually occur. Moreover, the molecular mechanism underlying the changes in cellular mechanotype is poorly studied and understood. Recent evidence suggests that the regulation of cellular mechanotype may be the result of alterations of multiple genes and signal transcription pathways.[41–45] Thus, knowledge of cell mechanotype changes in the early stages of cancer transformation and progression, and the mechanism or molecular pathways associated with these biomechanical changes may have a significant impact on not only developing biomarkers that can be utilized to distinguish invasive cancer, but also finding drug targets for disrupting, or inhibiting cancer cell invasion or metastasis.

We, here, report the cell mechanotype profiles in relation to UC utilizing an *in vitro* human urothelial carcinogenesis model that recapitulates the multistep process of cancer progression. Cellular Young's modulus and deformability were analyzed using AFM indentation, microfluidic-based DC, and q-DC analyses. From normal, to preinvasive, to invasive cells, Young's modulus, or cell stiffness, progressively decreases. Cellular deformability significantly increases. Previous studies indicated that changes in cell mechanotype could be detected in precancerous cervical intraepithelial lesions as early as CIN II,[46] and also in precancerous esophageal cells.[47] Our malignant transformation/progression experiments implied that cellular mechanotype changes may start at the early stage of malignant progression. To verify this finding in a disease-specific setting, we integrated cell mechanotyping technology into clinical samples. Currently, a variety of platforms have been developed to measure cellular mechanical properties, and different techniques are known to probe mechanical properties at different timescales and depths of the cell.[48] The most commonly explored method is to use biomechanical probes, represented by AFM and magnetic tweezer,[49] whereas cell deformability can be optically probed under the force induced on the whole cells. These methods also include micropipette aspiration,[50] microfluidic assays,[51] DC,[17] and microplate stretcher.[52] More recently, high-throughput techniques have also been explored.[53] Most of these techniques were developed in a laboratory setting and are still in a pre-clinical stage. Urinary exfoliated cells, which are directly from the primary tumor, provide a unique living model for the study of UC. However, for clinical specimens, variability is common in terms of cell number and type. Under AFM, uroepithelial cells, squamous epithelial cells, and cell of hematologic origin can be easily distinguished. Although only nine specimens were preliminarily analyzed in the current study, the findings were consistent with those from *in vitro* condition. Additionally, it presented a proof of concept for the development of mechanotype signature for urothelial cancer early detection.

It has become increasingly clear that EMT is driven by at least four fundamental regulatory network layers. The first layer is EMT-inducing transcription factor control, such as SNAI1, ZEB, and TWIST1. Another three layers are the expression of small non-coding RNAs, differential splicing, and translational and post-translational control, which determine the stabilization and localization of network proteins.[54] The dynamic and transient nature of EMT comprising a broad spectrum of intermediate phenotypes adds further complexity to capture EMT molecular status to determine the diagnosis and progression of cancer.[55] Our findings indicate a close correlation between EMT and cell mechanotype in the process of malignant progression, which provides new insight for developing novel biomarkers for cell-based UC early detection. The underlying molecular events and the specific mechanotype changes during UC development and progression can be summarized in **Figure 4**. One may expect that progression of EMT drives cell mechanotype changes during malignant transformation and progression. Conversely, it is also possible that change in cell mechanotype, such as decreasing in cell stiffness and increasing in deformability that occurs during malignant progression, enables tumor cells to detach from a primary tumor, squeeze through confined spaces, and facilitate cells to invade the surrounding tissue that affects EMT.

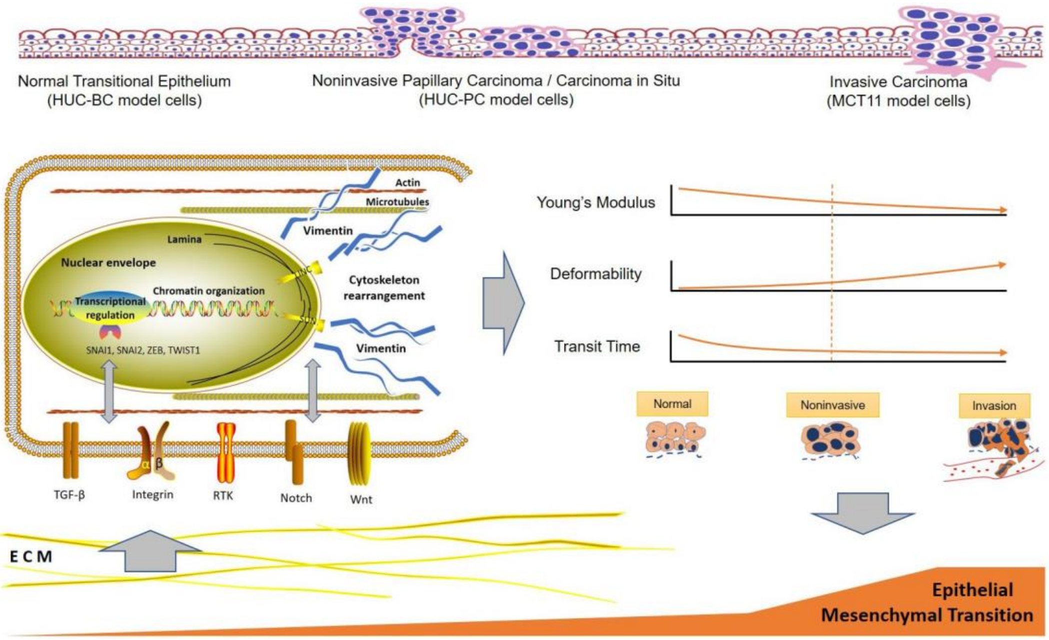

**Figure 4. Hypothetical scheme of the interactions between urothelial cell mechanotype change and epithelial to mesenchymal transition process during malignant transformation and progression. ECM, extracellular matrix**.

In summary, we described the specific mechanotype changes of urothelial cells in malignant transformation and progression. Measurable cell mechanotype changes of stiffness, deformability, and cell transit time occur early in the transformation process. As cells progress from normal, to preinvasive, to invasive cancer cells, Young's modulus of stiffness decreases and deformability increases gradually. The key molecular pathway implicated in urothelial cell mechanotype changes appears to be associated with EMT.

### 7.6 References

1. Siegel, R. L., Miller, K. D. & Jemal, A. Cancer statistics, 2018. *CA: A Cancer Journal for Clinicians* **68**, 7–30 (2018).
2. Leal, J., Luengo-Fernandez, R., Sullivan, R. & Witjes, J. A. Economic Burden of Bladder Cancer Across the European Union. *European Urology* **69**, 438–447 (2016).
3. Renshaw, A. A. & Gould, E. W. High-Grade Urothelial Carcinoma on Urine Cytology Resembling Umbrella Cells. *ACY* **62**, 62–67 (2018).
4. Nordentoft, I. *et al.* Mutational Context and Diverse Clonal Development in Early and Late Bladder Cancer. *Cell Reports* **7**, 1649–1663 (2014).
5. Santoni, G., Morelli, M. B., Amantini, C. & Battelli, N. Urinary Markers in Bladder Cancer: An Update. *Front. Oncol.* **8**, (2018).
6. Todenhöfer, T. *et al.* Combined application of cytology and molecular urine markers to improve the detection of urothelial carcinoma. *Cancer Cytopathology* **121**, 252–260 (2013).
7. He, H., Han, C., Hao, L. & Zang, G. ImmunoCyt test compared to cytology in the diagnosis of bladder cancer: A meta-analysis. *Oncology Letters* **12**, 83–88 (2016).
8. Beukers Willemien *et al.* FGFR3, TERT and OTX1 as a Urinary Biomarker Combination for Surveillance of Patients with Bladder Cancer in a Large Prospective Multicenter Study. *Journal of Urology* **197**, 1410–1418 (2017).
9. Tan, W. S. *et al.* Novel urinary biomarkers for the detection of bladder cancer: A systematic review. *Cancer Treatment Reviews* **69**, 39–52 (2018).
10. Lamy, P. *et al.* Paired Exome Analysis Reveals Clonal Evolution and Potential Therapeutic Targets in Urothelial Carcinoma. *Cancer Res* **76**, 5894–5906 (2016).
11. Cross, S. E., Jin, Y.-S., Rao, J. & Gimzewski, J. K. Nanomechanical analysis of cells from cancer patients. *Nat Nanotechnol* **2**, 780–783 (2007).

12. Cross, S. *et al.* AFM-based analysis of human metastatic cancer cells. *Nanotechnology* **19**, 384003–384003 (2008).
13. Cross, S. E., Jin, Y.-S., Lu, Q.-Y., Rao, J. & Gimzewski, J. K. Green tea extract selectively targets nanomechanics of live metastatic cancer cells. *Nanotechnology* **22**, 215101 (2011).
14. Sharma, S. *et al.* Correlative nanomechanical profiling with super-resolution F-actin imaging reveals novel insights into mechanisms of cisplatin resistance in ovarian cancer cells. *Nanomedicine: Nanotechnology, Biology and Medicine* **8**, 757–766 (2012).
15. Sharma, S., Santiskulvong, C., Rao, J., Gimzewski, J. K. & Dorigo, O. The role of Rho GTPase in cell stiffness and cisplatin resistance in ovarian cancer cells. *Integrative Biology* **6**, 611–617 (2014).
16. Nyberg, K. D. *et al.* Predicting cancer cell invasion by single-cell physical phenotyping. *Integrative Biology* **10**, 218–231 (2018).
17. Gossett, D. R. *et al.* Hydrodynamic stretching of single cells for large population mechanical phenotyping. *PNAS* **109**, 7630–7635 (2012).
18. Tse, H. T. K. *et al.* Quantitative Diagnosis of Malignant Pleural Effusions by Single-Cell Mechanophenotyping. *Science Translational Medicine* **5**, 212ra163-212ra163 (2013).
19. Che, J., Yu, V., B. Garon, E., W. Goldman, J. & Carlo, D. D. Biophysical isolation and identification of circulating tumor cells. *Lab on a Chip* **17**, 1452–1461 (2017).
20. Bookland, E. A. *et al.* Tumorigenic Transformation and Neoplastic Progression of Human Uroepithelial Cells after Exposure in Vitro to 4-Aminobiphenyl or Its Metabolites. *Cancer Res* **52**, 1606–1614 (1992).
21. Bookland, E. A., Reznikoff, C. A., Lindstrom, M. & Swaminathan, S. Induction of Thioguanine-resistant Mutations in Human Uroepithelial Cells by 4-Aminobiphenyl and Its N-Hydroxy Derivatives. *Cancer Res* **52**, 1615–1621 (1992).

22. D. Nyberg, K. *et al.* The physical origins of transit time measurements for rapid, single cell mechanotyping. *Lab on a Chip* **16**, 3330–3339 (2016).
23. Hughes, C. S. *et al.* Ultrasensitive proteome analysis using paramagnetic bead technology. *Molecular Systems Biology* **10**, 757 (2014).
24. Humphrey, P. A., Moch, H., Cubilla, A. L., Ulbright, T. M. & Reuter, V. E. The 2016 WHO Classification of Tumours of the Urinary System and Male Genital Organs—Part B: Prostate and Bladder Tumours. *European Urology* **70**, 106–119 (2016).
25. Wang, G. & McKenney, J. K. Urinary Bladder Pathology: World Health Organization Classification and American Joint Committee on Cancer Staging Update. *Archives of Pathology & Laboratory Medicine* **143**, 571–577 (2018).
26. Nyberg, K. D. *et al.* Quantitative Deformability Cytometry: Rapid, Calibrated Measurements of Cell Mechanical Properties. *Biophysical Journal* **113**, 1574–1584 (2017).
27. Sarrió, D. *et al.* Epithelial-Mesenchymal Transition in Breast Cancer Relates to the Basal-like Phenotype. *Cancer Res* **68**, 989–997 (2008).
28. Thiery, J. P., Acloque, H., Huang, R. Y. J. & Nieto, M. A. Epithelial-Mesenchymal Transitions in Development and Disease. *Cell* **139**, 871–890 (2009).
29. Guo, C. C. *et al.* Dysregulation of EMT Drives the Progression to Clinically Aggressive Sarcomatoid Bladder Cancer. *Cell Reports* **27**, 1781-1793.e4 (2019).
30. Brabletz, T. To differentiate or not — routes towards metastasis. *Nat Rev Cancer* **12**, 425–436 (2012).
31. Michalski, A. *et al.* Mass Spectrometry-based Proteomics Using Q Exactive, a High-performance Benchtop Quadrupole Orbitrap Mass Spectrometer*. *Molecular & Cellular Proteomics* **10**, M111.011015 (2011).
32. Kokkinos, M. I. *et al.* Vimentin and Epithelial-Mesenchymal Transition in Human Breast Cancer – Observations in vitro and in vivo. *CTO* **185**, 191–203 (2007).

33. Kim, J. *et al.* Invasive Bladder Cancer: Genomic Insights and Therapeutic Promise. *Clin Cancer Res* **21**, 4514–4524 (2015).
34. Hashmi, A. A. *et al.* Cytokeratin 5/6 expression in bladder cancer: association with clinicopathologic parameters and prognosis. *BMC Res Notes* **11**, 207 (2018).
35. Coulombe, P. A. & Wong, P. Cytoplasmic intermediate filaments revealed as dynamic and multipurpose scaffolds. *Nat Cell Biol* **6**, 699–706 (2004).
36. Mendez, M. G., Kojima, S.-I. & Goldman, R. D. Vimentin induces changes in cell shape, motility, and adhesion during the epithelial to mesenchymal transition. *The FASEB Journal* **24**, 1838–1851 (2010).
37. Qi, D. *et al.* Screening cell mechanotype by parallel microfiltration. *Sci Rep* **5**, 17595 (2015).
38. Maier, J., Traenkle, B. & Rothbauer, U. Visualizing Epithelial–Mesenchymal Transition Using the Chromobody Technology. *Cancer Res* **76**, 5592–5596 (2016).
39. Liu, C.-Y., Lin, H.-H., Tang, M.-J. & Wang, Y.-K. Vimentin contributes to epithelial-mesenchymal transition cancer cell mechanics by mediating cytoskeletal organization and focal adhesion maturation. *Oncotarget* **6**, 15966–15983 (2015).
40. Lu, Q.-Y. *et al.* Green Tea Extract Modulates Actin Remodeling via Rho Activity in an In vitro Multistep Carcinogenic Model. *Clin Cancer Res* **11**, 1675–1683 (2005).
41. Way, M. & Weeds, A. Cytoskeletal ups and downs. *Nature* **344**, 292–293 (1990).
42. Provenzano, P. P., Inman, D. R., Eliceiri, K. W. & Keely, P. J. Matrix density-induced mechanoregulation of breast cell phenotype, signaling and gene expression through a FAK–ERK linkage. *Oncogene* **28**, 4326–4343 (2009).
43. Lammerding, J. Mechanics of the Nucleus. in *Comprehensive Physiology* 783–807 (American Cancer Society, 2011). doi:10.1002/cphy.c100038.
44. de las Heras, J. I., Batrakou, D. G. & Schirmer, E. C. Cancer biology and the nuclear envelope: A convoluted relationship. *Seminars in Cancer Biology* **23**, 125–137 (2013).

45. Fedorchak, G. R., Kaminski, A. & Lammerding, J. Cellular mechanosensing: Getting to the nucleus of it all. *Progress in Biophysics and Molecular Biology* **115**, 76–92 (2014).
46. Ding, Y. *et al.* Mechanical characterization of cervical squamous carcinoma cells by atomic force microscopy at nanoscale. *Med Oncol* **32**, 71 (2015).
47. Fuhrmann, A. *et al.* AFM stiffness nanotomography of normal, metaplastic and dysplastic human esophageal cells. *Phys. Biol.* **8**, 015007 (2011).
48. Urbanska, M. *et al.* A comparison of microfluidic methods for high-throughput cell deformability measurements. *Nat Methods* **17**, 587–593 (2020).
49. Yang, R. *et al.* The Emergence of AFM Applications to Cell Biology: How new technologies are facilitating investigation of human cells in health and disease at the nanoscale. *J Nanosci Lett* **1`**, 87–101 (2011).
50. Oh, M.-J., Kuhr, F., Byfield, F. & Levitan, I. Micropipette Aspiration of Substrate-attached Cells to Estimate Cell Stiffness. *J Vis Exp* (2012) doi:10.3791/3886.
51. Guo, Q. *et al.* Microfluidic analysis of red blood cell deformability. *Journal of Biomechanics* **47**, 1767–1776 (2014).
52. Thoumine, O., Ott, A., Cardoso, O. & Meister, J.-J. Microplates: a new tool for manipulation and mechanical perturbation of individual cells. *Journal of Biochemical and Biophysical Methods* **39**, 47–62 (1999).
53. Darling, E. M. & Di Carlo, D. High-Throughput Assessment of Cellular Mechanical Properties. *Annual Review of Biomedical Engineering* **17**, 35–62 (2015).
54. Craene, B. D. & Berx, G. Regulatory networks defining EMT during cancer initiation and progression. *Nat Rev Cancer* **13**, 97–110 (2013).
55. Santamaria, P. G., Moreno-Bueno, G., Portillo, F. & Cano, A. EMT: Present and future in clinical oncology. *Molecular Oncology* **11**, 718–738 (2017).